Deformation Mechanisms and Microstructure Evolution in HfNbTaTiZr High Entropy Alloy during Thermo-mechanical Processing at Elevated Temperatures

2019

Rajeshwar Reddy Eleti

Contents

Chapter 1

Introduction

1.1. Background

The classical alloy design concept for developing structural materials is essentially to use one principal element with relatively small amounts of other alloying elements for introducing or improving desired properties. This conventional strategy of alloy design makes it possible to distinguish the base element in major proportion and the alloying element(s) in minor proportions. Well known examples of such alloys are different grades of steels (iron-base alloy), aluminum alloys and copper alloys. On the other hand, another way of exploring and strategizing alloy design is to extend the conventional method by adding more alloying elements in larger quantities. For example, chemical composition of Ni-based superalloys often contains Ni ~52%, Cr ~19%, Fe ~18%, and other minor alloying elements like Nb, Ta, Mo, Ti, etc. Such concentrated chemical compositions have been reported to have a wide range of tunable microstructures and excellent mechanical properties [1]. However, superalloys are still defined based on one major element and the rest are considered as alloying elements.

In contrast to the conventional alloys, a new concept in alloy design that has started recently is to consider all elements in equiatomic proportions. For instance, if an alloy contains 5 elements in equiatomic proportion, each element constitutes 20 at.% of the total material. Considering this new strategy, Brian Cantor [2], and Jien-Wei Yeh [3] independently studied multi-component alloys having equiatomic proportions. In both of their studies, they used more than 5 principle elements. Despite including a large number of different elements, they found that these alloys often showed single-phase solid solution of simple face-centered cubic (FCC) or body-centered cubic (BCC) crystal. Well-known

examples are CoCrFeMnNi and HfNbTaTiZr in equiatomic proportions having single phase FCC and BCC respectively [4].

Describing these alloys, Yeh et al. [3] first coined the term high entropy alloys (HEAs). The description of the term HEA has been considered based on an equiatomic random solid solution having significantly higher configurational entropy (S_{conf}) compared to the conventional alloys. For instance, configurational entropy of a system can be calculated by using Boltzmann's equation,

$$\Delta S_{conf} = k \ln w \tag{1.1}$$

where, k is Boltzmann's constant and w number of ways in which an element can be mixed or arranged in the system. In the presence of multiple numbers of elements, the contribution of each element per mole for the formation of solid solution by increasing the mixing entropy is given as,

$$\Delta S_{conf} = -R\sum_{i=1}^{n} X_i \ln X_i \tag{1.2}$$

where, R is the gas constant, n is number of elements and X_i is mole fraction of the constituent element. In the case of equiatomic proportions, **Equation 1.2** could be reduced to,

$$\Delta S_{conf} = R \ln n \tag{1.3}$$

where, R is the gas constant and n is the number of elements in the equi-atomic solid solution. For any solid solution composed of 5 components in the equiatomic proportion, the calculated configurational entropy of the system from the above equation yields 1.61R. On the other hand, Ni-based superalloys and several bulk metallic glasses satisfy configurational entropy of 1.3R. In order to realize the formation of a random solid solution, in the case of equiatomic concentrated alloys, Yeh et al. [3] arbitrarily categorized that 1.5R might be sufficiently large to form a random solid solution or to suppress the

formation of multiple phases and intermetallic compounds. Thus, Yeh et al. [3] suggested that any solid solution satisfying $\Delta S_{conf} \geq 1.5R$ could be considered as HEA.

Based on the compositional consideration, HEAs are defined as alloys containing at least five or more elements in equiatomic or near equiatomic proportions ranging from 5at.% to ~ 35at.%.

This new strategy of alloy design has expanded high possibility to explore new alloys. Various kinds of HEA systems have been studied and some of them have shown exceptional properties, such as better fatigue limit [5], high fracture toughness [6], high wear and corrosion resistance [7], and high-temperature strength [8] better than conventional alloys. The properties of HEAs are often attributed to the four "*core effects*", i.e., high-entropy effect, severe lattice distortion effect, sluggish diffusion effect, and cocktail effect [4], which are explained in details in the next section.

1.2. Core effects of High Entropy Alloys

1.2.1. High Entropy Effect

During solidification of a multi-component melt, solid state of an alloy can have either random solid solution or multiple phases including intermetallic compounds. A random solid solution phase containing multi-component in the equiatomic proportions has the maximum configurational entropy, because different constituent elements can randomly occupy different lattice sites. On the other hand, intermetallic compounds are composed of stoichiometric chemical compositions having fully or partially ordered structures where each kind of elements occupies specific lattice sites such that the configuration entropy is low.

Interestingly, HEAs mostly solidify as simple FCC or BCC solid solution phases. According to alloy thermodynamics, Gibbs free energy of mixing, ΔG_{mix}, is,

$$\Delta G_{mix} = \Delta H_{mix} - T\Delta S_{mix} \tag{1.4}$$

where, ΔH_{mix} is enthalpy of mixing, ΔS_{mix} is entropy of mixing, and T is absolute temperature. Gibbs free energy of mixing states that the increased entropy of mixing lowers the free energy of multi-elementary systems and may facilitate the formation of simple solid solutions instead of intermetallic compounds. However, some of the reports indicated high entropy effect does not necessarily suppress the formation of compounds. For example, addition of Boron, in the AlCoCrCuFeNi alloy led to the formation of (Cr, Fe)-rich borides [4], and high-temperature annealing experiments showed that the formed borides were stable [4]. It was suggested that the large negative enthalpy for the formation of borides can override the high entropy effect in such systems. In a different study, on the equiatomic CoCrFeMnNi having single phase FCC crystal, Otto et al. [9] evaluated its phase stability under prolonged annealing time intervals for 500 days at intermediate temperature 500°C and at high temperature 900°C. They found that the single phase solid solution decomposes into different phases ($L1_0$-NiMn, B2-FeCo and Cr-rich BCC phase) at 500°C, whereas the solid solution remained stable FCC phase at 900°C. These observations might be understood in a manner conforming to **Equation 1.4**. For any system, enthalpy of mixing dominates at low temperatures, whereas the high configuration entropy is effective at high temperatures. Therefore, it has been suggested that the competition between entropy and enthalpy determines the phase formation in the HEAs.

1.2.2. Severe Lattice Distortion Effect

In HEA solid solution, every atom is likely surrounded by another kind of element atom each having different atomic radius. Owing to the difference in atomic size, atoms are displaced from the ideal lattice sites in pure metals. As a result, the lattice of HEA solid solution is severely distorted [4]. A schematic illustration indicating the lattice distortion in HEA is shown in **Figure 1.1**.

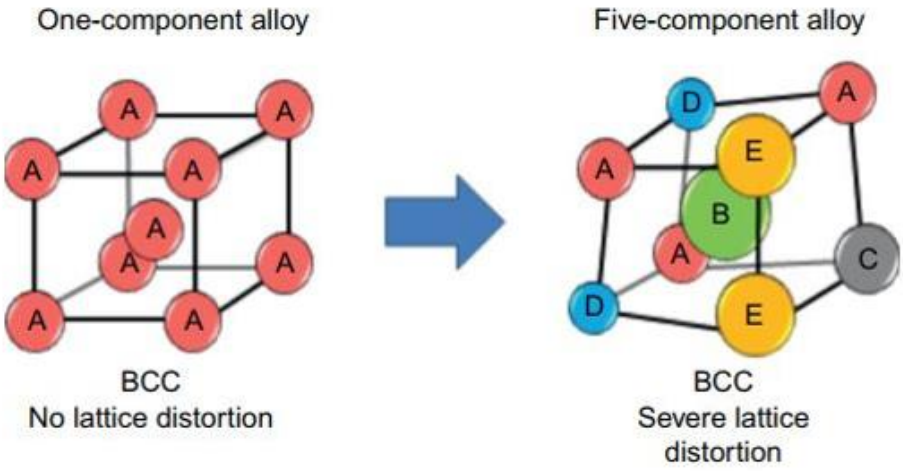

Figure 1.1 A schematic illustration showing the possibility of lattice distortion in a 5 component BCC HEA [4].

For plastic deformation of metallic materials, the fundamental mechanism that governs mechanical properties is dislocation slips. Due to the lattice distortion in HEAs, dislocations are expected to possess unusual dislocation core structure and the Peierls potential is fluctuated, which was recently found to have a significant effect on the mechanical properties of HEAs [4,10,11]. For example, Wu et al. [12] reported a systematic study on the mechanical properties of equiatomic CoCrFeMnNi and its compositionally derived subsystems such as CoCrFeNi, and CoFeNi all having single phase FCC structures. They found that a strong temperature dependence of the yield strength was essentially due to lattice friction resulting from the lattice distortion.

1.2.3. Sluggish Diffusion Effect

Sluggish diffusion effect states that the diffusion related processes in HEAs is slow compared to the conventional alloys. This could be understood in terms of the nature of the HEA solid solution. In HEAs, every nearest neighboring lattice site is expected to pair with a different kind of element. Due to this, the differences in local atomic bonding results in

different local energies for each lattice site. Tsai et al. [13] proposed that when an atom jumps into lower energy site, the atom is trapped in the site and a chance to escape from the site is low. On the other hand, if the site has a high potential energy, an atom may jump back to an initial lower energy site. Based on the analysis, they showed that the activation energy (Q) for the diffusion of individual elements in CoCrFeMnNi was higher than that in pure metals and conventional alloys. **Figure 1.2** shows a comparison of the activation energies for diffusion of Co, Cr, Fe, Mn, and Ni atoms in different matrices. In the CoCeFeMnNi HEA, Ni was found to have the highest activation energy, Q ~317.5 kJ mol^{-1}. In a different work, Liu et al. [14] reported a grain coarsening behavior of CoCrFeMnNi and found an activation energy for the grain growth, Q ~321 kJ mol^{-1}, similar to the above mentioned value, which supports a possibility of sluggish diffusion.

Vaidya et al. [15] studied tracer diffusion of Ni in the CoCrFeMnNi HEA and showed that the diffusivity of Ni in CoCrFeMnNi is very close to that in pure Ni, which indicated the lack of sluggish diffusion effect. However, the number of accumulated study is little, and further experimental analysis is required. Thus, the possibility of sluggish diffusion effect is still an open question in the HEA community.

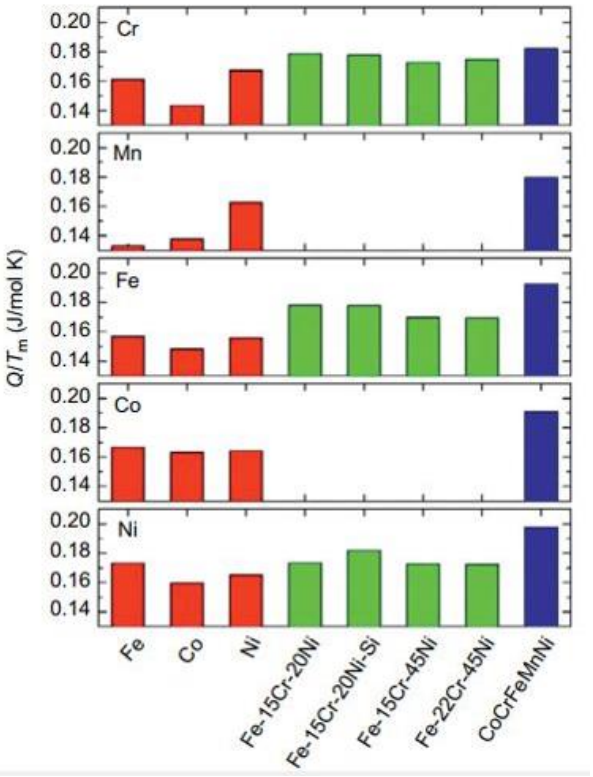

Figure 1.2 Activation energy for diffusion of Co, Cr, Fe, Mn, and Ni in different matrices. Activation energy is normalized by the melting temperature [4].

1.2.4. Cocktail Effect

The cocktail effect is a phenomenon that has been used to describe some properties of HEAs [4]. In several articles previously reported, some particular properties of HEAs are related to the properties of constituent elements. A well-known example is an addition of lightweight elements decreases the density of the HEA [16]. However, the cocktail effect also insists a mutual interaction of constituent elements. For instance, an addition of Al into CoCrCuFeNi increases the hardness of the $Al_xCoCrCuFeNi$ alloy [4]. **Figure 1.3** shows the effect of Al content on the hardness of $Al_xCoCrCuFeNi$. This is because the addition of Al induces the formation of hard BCC phase. Senkov et al.[17] reported that the hardness of MoNbTaVW equiatomic BCC alloy was 5250 MPa, which was three times higher than the

value predicted by the rule of mixture. The cocktail effect indicates that properties of HEAs are not necessarily an average of constituent elements but affected by mutual interaction between the elements.

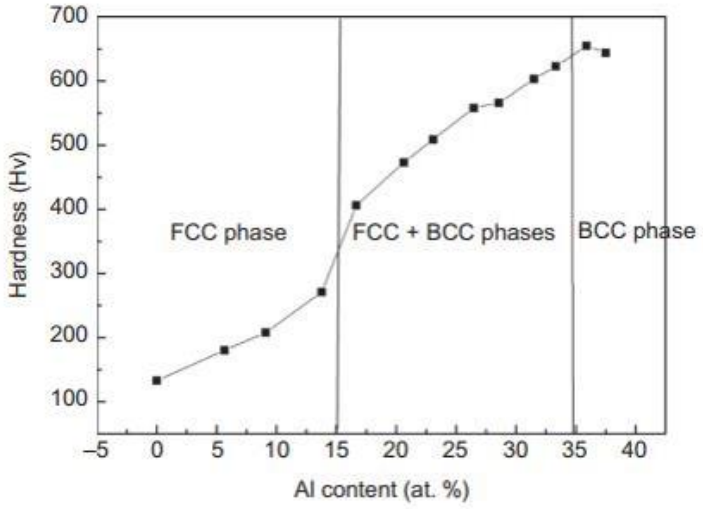

Figure 1.3 Effect of Al content on the hardness of $Al_xCoCrFeCuNi$ HEA [4].

1.3. Refractory High Entropy Alloys

Manufacturers of gas turbine engines have been continuously seeking to improve the operating temperature of engines. By increasing the operating temperature of engines, the performance and efficiency of engines are considerably improved. However, the currently using Nickle-based superalloys are working at temperatures close to their physical limits and cannot withstand any further increase in the operating temperatures. Thus, design and development of new materials are critically important to realize the next generation turbine engines with better efficiency [18,19].

Given the flexibility for alloy design based on HEA philosophy, Senkov et al. [17] introduced refractory HEAs (RHEAs) that can withstand high temperatures. RHEAs often consist of refractory metals, such as Ti, Zr, Hf, V, Nb, Ta, Cr, Mo, and W. Most of the reported RHEAs have single phase solid solution of BCC structure in the as-cast state.

Several RHEAs with promising properties at elevated temperatures have been reported [17,20–22]. As shown in **Figure 1.4**, RHEAs like NbMoTaW, VNbMoTaW and $Al_{0.4}Hf_{0.6}NbTaTiZr$ have shown exceptional strength at temperatures above 1000°C, even compared to conventional superalloys and its compositional derivatives [23]. Due to their retained strengths and several other attractive properties, RHEAs are being considered as replacements for conventional alloys at high temperatures.

When RHEAs (and other HEAs) are produced in large volume, they are expected to experience thermo-mechanical processing (TMP) at elevated temperatures as their fabrication process after casting. Although RHEAs were reported to have exceptionally high yield strengths at high temperatures, their flow behavior and microstructure evolution have not been fully explored. Moreover, fundamental deformation mechanisms of RHEAs at elevated temperatures are scarcely understood by now.

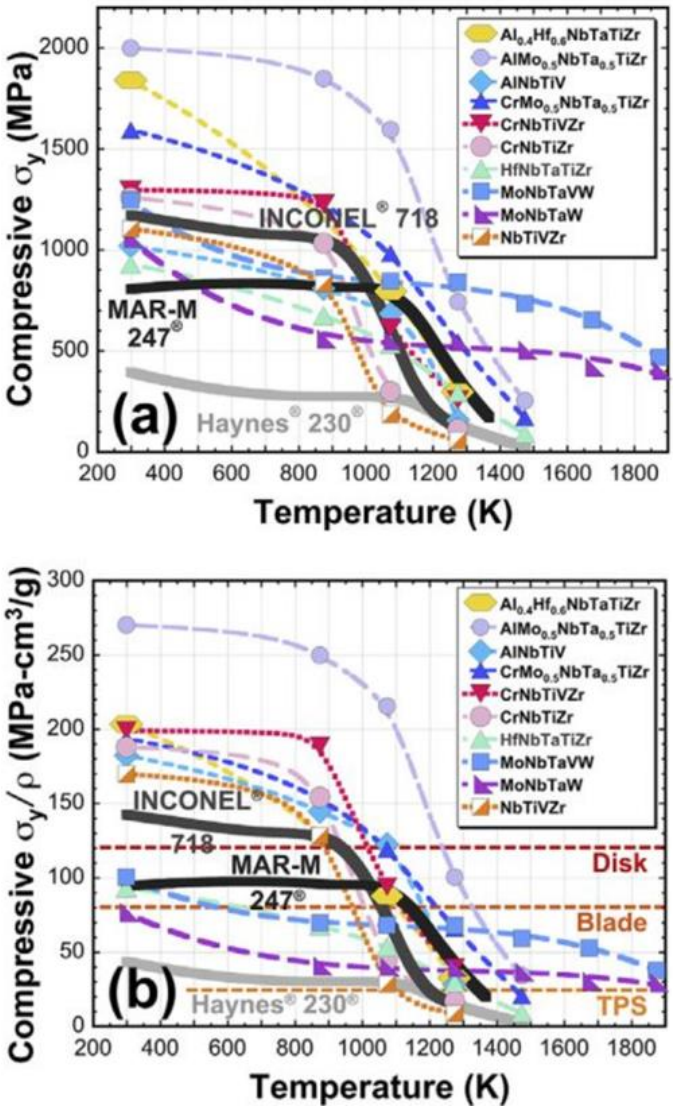

Figure 1.4 Temperature dependence of (a) Compressive yield strength, σ_y (b) σ_y normalized by alloy density of the refractory HEA. Compressive tests were reported to have performed at strain rate 2×10^{-4} s^{-1} to 10^{-3} s^{-1}. [23]

1.4. Thermo-mechanical Processing at Elevated Temperatures

Thermo-mechanical processing (TMP) describes combinations of plastic deformation of metallic materials with heat treatments. TMP is often carried out above $0.4T_m$, where T_m is the melting temperature (°C). Deformation at such high temperatures often undergoes simultaneous changes of microstructures. The central theme of TMP studies has focused on controlling microstructures and investigating flow behaviors. TMP has been successfully employed to a wide variety of materials like high strength low alloy (HSLA) steels [24–26], Ti-alloys [27], and Ni-based superalloys [28]. Controlling microstructures during TMP were reported to govern high temperature deformation mechanisms and final mechanical properties.

Therefore, it is fundamentally important to understand and clarify microstructural evolution during deformation at high temperatures of HEAs. Here, it is important to note that microstructural changes occurring during deformation are considered as *dynamic* processes, which include, for example, '*dynamic recovery*' (DRV) and '*dynamic recrystallization*' (DRX). Both of these processes occurring during deformation counteract strain-hardening, thus are referred as softening processes.

Dynamic recovery (DRV) is one of the processes caused by annihilation and/or rearrangement of dislocations during deformation, which leads to suppressed strain-hardening. It is known that DRV is enhanced to occur in body-centered cubic (BCC) metals and alloys, and in face-centered cubic (FCC) metals and alloys having high stacking fault energies (like aluminum and its alloys). In BCC metals and alloys, the diffusivity of atoms is originally higher owing to their looser packing of atoms than FCC crystals, and cross-slip of screw dislocations is easy to occur in BCC and high stacking-fault energy FCC materials [29]. Additionally, the possibility of dislocation climb assisted by the diffusion of vacancies during high-temperature deformation also aids dislocation annihilation or at least rearrangement. In terms of microstructure, DRV is often recognized to show no significant changes of grain shape but well-developed sub-grain structures in grains interiors. In a stress-strain curve, DRV is often recognized by steady-state flow stress which indicates the

rate of generation and accumulation of dislocations reached a dynamic equilibrium with the rate of annihilation of dislocations.

On the other hand, *Dynamic recrystallization* (DRX) offers significant microstructural changes during deformation at elevated temperatures. DRX refers to the formation of new strain-free grains during deformation. It is known that DRX is most commonly observed in FCC metals and alloys having low stacking fault energies. As is well known, when the stacking fault energy is low, {111}<110> dislocations tend to dissolve into two Shockley partial dislocations. As Shockley partial dislocations generally have mixed nature of screw and edge dislocations, cross-slip of pure screw dislocations becomes difficult to happen, so that recovery by the aid of cross-slip is suppressed. As a result, dislocation density (i.e., the driving force for recrystallization) in the material greatly increases during deformation, leading to DRX. DRX preferentially occurs along initial grain boundaries (GBs), often appear like decorating initial GBs. Thus, resulting microstructures are referred to the necklace-like structure. **Figure 1.5** shows schematic illustrations on the formation of necklace-like DRX structure along initial grain boundaries. DRX consumes deformed regions extensively and replaces them into strain-free grains. As a result, the occurrence of DRX decreases the flow stress and increases deformability of materials. In a stress-strain curve, the occurrence of DRX is manifested by a hump of the flow stress, due to the softening effect of DRX. **Figure 1.6** shows typical stress-strain curves for materials where DRV or DRX is dominant as a dynamic restoration process.

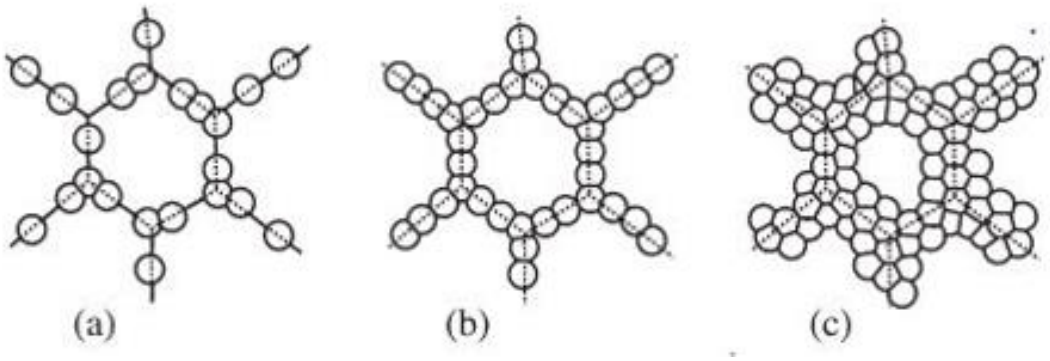

Figure 1.5 Schematic illustration showing formation of the characteristic DRX necklace-like structure. (a) initiation of DRX grains along the initial grain boundary, (b-c) propagation of DRX grains into the parent grain during the progress of deformation [30].

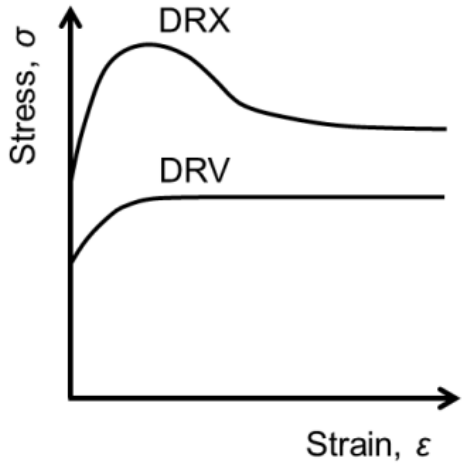

Figure 1.6 Typical stress-strain curves for metallic materials that exhibit dynamic recovery (DRV) and dynamic recrystallization (DRX).

As discussed in the previous sections, HEAs possess interesting core effects, such as sluggish diffusion, severe lattice distortion. Adopting TMP for HEAs might yield attractive microstructures and properties, as well as essential understanding of unexplored behaviors of HEAs at high temperatures and basic understanding on the core effects.

1.5. Thermo-mechanical Processing of High Entropy Alloys

When HEAs are fabricated in established mass-production routes, they must experience any hot working processes after solidification. Thus, it is quite important to understand hot-deformation behavior and microstructure evolution of HEAs during thermo-mechanical processing at high-temperatures.

Recently, Eleti et al. [31] have reported the hot-deformation behavior of equiatomic CoCrFeMnNi HEA having single phase FCC structure. The study showed that the CoCrFeMnNi HEA undergoes extensive grain refinement at relatively low strain level (e = 60% in compression) due to DRX, which was considered owing to the alloy's low stacking fault energy. Furthermore, as shown in **Figure 1.7**, when the alloy was deformed at 1000°C (0.75 T_m) and a strain rate of 10^{-3} s^{-1}, it showed a fully recrystallized microstructure having high resistance to grain growth. Most of the DRX grains had have grain sizes smaller than under 5 μm (not including annealing twin boundaries). The stability of fine grain size at high-temperature might be attributed to sluggish diffusion in HEAs. Thereby, Eleti et al. [31] showed a possibility to fabricate fine-grained microstructures in HEAs without using severe plastic deformation processes, depending on appropriate deformation temperature and strain rate.

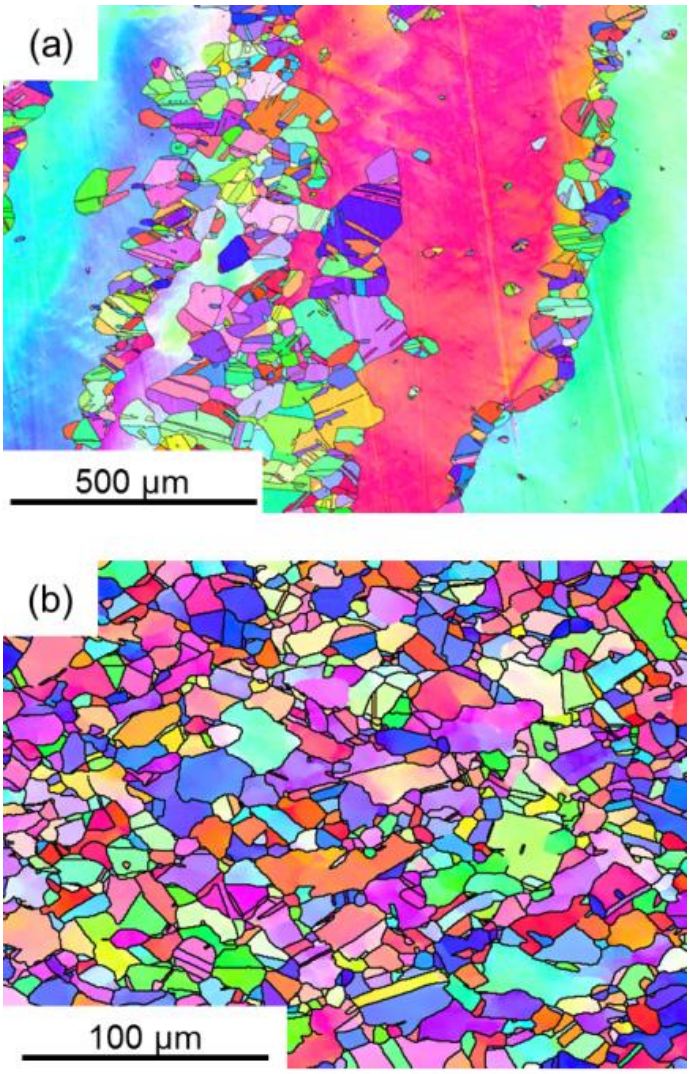

Figure 1.7 (a) Starting microstructure of CoCrFeMnNi before deformation, (b) Microstructure obtained after deformation at 1000°C for the strain rate 10^{-3} s^{-1} until 60% of initial height reduction. High angle grain boundaries (including twin boundaries) having misorientation, (θ) ($\theta \geq 15°$) are painted with black lines. Compression axis is parallel to the vertical axis of the microstructure (b). The complete details on starting microstructure are available elsewhere [31].

Plastic flow behaviors at high-temperatures are often controlled by thermally activated processes like diffusion. Therefore, understanding the flow behavior through flow stress analysis provides an insight into deformation mechanisms. For example, Eleti et al. [31] estimated the activation energy (Q) for hot-compression of CoCrFeMnNi HEA from near-steady state flow stresses, using Arrhenius-type constitutive equation,

$$\dot{\varepsilon} = A\sigma^n \exp\left(\frac{-Q}{RT}\right) \tag{1.3}$$

where, $\dot{\varepsilon}$ is the strain rate (s^{-1}), A a material constant, σ the flow stress (MPa) at a constant strain (or steady-state stress), n the stress exponent, Q the activation energy for hot-deformation ($kJmol^{-1}$), R the gas constant (8.314 $JK^{-1}mol^{-1}$), and T the deformation temperature (K). The estimated Q in CoCrFeMnNi was ~350 $kJmol^{-1}$. Surprisingly, the activation energy for high-temperature deformation was very close to the activation energy for the slowest diffusing element, i.e., Ni in the CoCrFeMnNi solid solution, Q ~317 kJ mol^{-1} [13]. The Q value estimated by Eleti et al. [31] suggested that the diffusion of Ni most likely controls high-temperature deformation of CoCrFeMnNi. In a different study, He et al. [32] estimated an activation energy for high-temperature deformation of CoCrFeMnNi under steady-state flow stress conditions in tensile tests. The reported Q was ~330 $kJmol^{-1}$, which was also very close to the Q for the diffusion of Ni in CoCrFeMnNi alloy.

The similarities in the activation energies for hot-deformation and for diffusion of the slowest diffusing element in HEAs supports the possibility that flow stress analysis might give insights for thermally activated/rate-controlling mechanisms. Mapping such high-temperature parameters for new alloys is useful considering future prospects of HEAs. Unfortunately, however, studies on high-temperature deformation of HEAs is still limited.

1.6. Alloy Selection for the Present Study

In the research of suitable refractory high entropy alloys for high temperature applications, Senkov et al. [20] introduced the equiatomic HfNbTaTiZr alloy. In the as-cast state, HfNbTaTiZr solidifies as single phase body-centered cubic (BCC) solid solution. Schuh et al. [33] reported a systematic investigation of the phase stability in HfNbTaTiZr and suggested that the single phase BCC structure is stable above 1000°C. Unlike several RHEAs exhibiting poor ductility at low temperatures, HfNbTaTiZr was reported to show homogeneous plastic flow without cracking to at least 50% reduction in compression at ambient temperature [20]. Besides that, it was reported that HfNbTaTiZr could be heavily cold rolled by 86.4% reduction in thickness at room temperature without any evidence for crack formation [20]. On the other hand, Juan et al. [34] reported that HfNbTaTiZr possessed excellent mechanical properties such as high yield strength (σ_y > 1000 MPa) and tensile elongation (e > 10%) at ambient temperature.

Senkov et al. [22] reported a preliminary study on high-temperature deformation of this alloy, but information available about this alloy concerning flow behavior and microstructural evolution is still limited. Although mechanical properties of HfNbTaTiZr are attractive, deformation mechanisms of this alloy are still not fully understood. In order to realize the full potential of this alloy, further systematic investigations are required.

It can be concluded, therefore, HfNbTaTiZr is an interesting alloy to explore its flow behaviors, microstructure evolution, and deformation mechanisms both at ambient and high temperatures. The present study aims to clarify flow behaviors and microstructural evolution during thermo-mechanical processing at high temperatures, as well as mechanical properties and deformation mechanisms at high and ambient temperatures. Systematic research was outlined with specific objectives listed in the next section.

1.7. Research Objectives

The purpose of the present study is as follows:

1. To investigate thermo-mechanical behaviors of HfNbTaTiZr HEA over a wide range of deformation temperatures and strain-rates, for understanding microstructure/texture evolution and their relationship with plastic deformation at elevated temperatures.

2. To investigate dynamic and static recrystallization behaviors of HfNbTaTiZr HEA during and after hot-deformation respectively, for understanding the effects of microstructure evolution on the deformation mechanisms and on later recrystallization behavior.

3. To investigate the effect of grain refinement on mechanical properties of HfNbTaTiZr HEA during tensile deformation at ambient temperature.

1.8. Thesis Outline

Chapter 1 is the "*Introduction*," where the concepts of high entropy alloys, thermo-mechanical processing, research objective, and the thesis outline are introduced.

Chapter 2 studies "*Deformation Behavior and Microstructure Evolution in High Temperature Processing of HfNbTaTiZr Refractory High Entropy Alloy*," where the microstructural evolution and its relationship to plastic deformation of HfNbTaTiZr at different temperatures and strain rates are investigated and discussed.

Chapter 3 studies "*Dynamic Recrystallization and Related Deformation Mechanisms of the Equiatomic HfNbTaTiZr Refractory High Entropy Alloy*," where the occurrence of dynamic recrystallization and its effect on deformation mechanisms and high temperature flow behavior of HfNbTaTiZr are investigated and discussed.

Chapter 4 studies "*Recrystallization Behavior of Hot-deformed HfNbTaTiZr Refractory High Entropy Alloy*," where the static recrystallization behaviors of hot-deformed HfNbTaTiZr are investigated and discussed.

Chapter 5 studies "*Lack of Normal Hardening in HfNbTaTiZr Refractory High Entropy Alloy*," where the mechanical behaviors of HfNbTaTiZr having different grain sizes and the operative deformation mechanisms are investigated and discussed.

Chapter 6 is the "*Summary and Conclusions*," which shows summary and conclusions of the thesis.

References

[1] M.F. Ashby, Materials selection in mechanical design, fourth ed., Butterworth-Heinemann, London, 2011.

[2] B. Cantor, I.T.H. Chang, P. Knight, A.J.B. Vincent, Microstructural development in equiatomic multicomponent alloys, Mater. Sci. Eng. A. 375–377 (2004) 213–218. doi:https://doi.org/10.1016/j.msea.2003.10.257.

[3] J.-W. Yeh, S.-K. Chen, S.-J. Lin, J.-Y. Gan, T.-S. Chin, T.-T. Shun, C.-H. Tsau, S.-Y. Chang, Nanostructured High-Entropy Alloys with Multiple Principal Elements: Novel Alloy Design Concepts and Outcomes, Adv. Eng. Mater. 6 (2004) 299–303. doi:10.1002/adem.200300567.

[4] B.S. Murty, J.W. Yeh, S. Ranganathan, High-Entropy Alloys, first ed., Elsevier, 2014.

[5] M.A. Hemphill, T. Yuan, G.Y. Wang, J.W. Yeh, C.W. Tsai, A. Chuang, P.K. Liaw, Fatigue behavior of Al0.5CoCrCuFeNi high entropy alloys, Acta Mater. 60 (2012) 5723–5734. doi:https://doi.org/10.1016/j.actamat.2012.06.046.

[6] B. Gludovatz, A. Hohenwarter, D. Catoor, E.H. Chang, E.P. George, R.O. Ritchie, A fracture-resistant high-entropy alloy for cryogenic applications, Science (80-.). 345 (2014) 1153 LP-1158. doi:10.1126/science.1254581.

[7] Y. Zhang, T.T. Zuo, Z. Tang, M.C. Gao, K.A. Dahmen, P.K. Liaw, Z.P. Lu, Microstructures and properties of high-entropy alloys, Prog. Mater. Sci. 61 (2014) 1–93. doi:https://doi.org/10.1016/j.pmatsci.2013.10.001.

[8] O.N. Senkov, D.B. Miracle, K.J. Chaput, J.-P. Couzinie, Development and exploration of refractory high entropy alloys—A review, J. Mater. Res. 33 (2018) 3092–3128. doi:DOI: 10.1557/jmr.2018.153.

[9] F. Otto, A. Dlouhý, K.G. Pradeep, M. Kuběnová, D. Raabe, G. Eggeler, E.P. George, Decomposition of the single-phase high-entropy alloy CrMnFeCoNi after prolonged

anneals at intermediate temperatures, Acta Mater. 112 (2016) 40–52. doi:https://doi.org/10.1016/j.actamat.2016.04.005.

[10] R.S. Mishra, N. Kumar, M. Komarasamy, Lattice strain framework for plastic deformation in complex concentrated alloys including high entropy alloys, Mater. Sci. Technol. 31 (2015) 1259–1263. doi:10.1179/1743284715Y.0000000050.

[11] S. Yoshida, T. Bhattacharjee, Y. Bai, N. Tsuji, Friction stress and Hall-Petch relationship in CoCrNi equi-atomic medium entropy alloy processed by severe plastic deformation and subsequent annealing, Scr. Mater. 134 (2017) 33–36. doi:https://doi.org/10.1016/j.scriptamat.2017.02.042.

[12] Z. Wu, H. Bei, F. Otto, G.M. Pharr, E.P. George, Recovery, recrystallization, grain growth and phase stability of a family of FCC-structured multi-component equiatomic solid solution alloys, Intermetallics. 46 (2014) 131–140. doi:https://doi.org/10.1016/j.intermet.2013.10.024.

[13] K.-Y. Tsai, M.-H. Tsai, J.-W. Yeh, Sluggish diffusion in Co–Cr–Fe–Mn–Ni high-entropy alloys, Acta Mater. 61 (2013) 4887–4897. doi:https://doi.org/10.1016/j.actamat.2013.04.058.

[14] W.H. Liu, Y. Wu, J.Y. He, T.G. Nieh, Z.P. Lu, Grain growth and the Hall–Petch relationship in a high-entropy FeCrNiCoMn alloy, Scr. Mater. 68 (2013) 526–529. doi:https://doi.org/10.1016/j.scriptamat.2012.12.002.

[15] M. Vaidya, K.G. Pradeep, B.S. Murty, G. Wilde, S. V Divinski, Bulk tracer diffusion in CoCrFeNi and CoCrFeMnNi high entropy alloys, Acta Mater. 146 (2018) 211–224. doi:https://doi.org/10.1016/j.actamat.2017.12.052.

[16] K.M. Youssef, A.J. Zaddach, C. Niu, D.L. Irving, C.C. Koch, A Novel Low-Density, High-Hardness, High-entropy Alloy with Close-packed Single-phase Nanocrystalline Structures, Mater. Res. Lett. 3 (2015) 95–99. doi:10.1080/21663831.2014.985855.

[17] O.N. Senkov, G.B. Wilks, D.B. Miracle, C.P. Chuang, P.K. Liaw, Refractory high-entropy alloys, Intermetallics. 18 (2010) 1758–1765. doi:https://doi.org/10.1016/j.intermet.2010.05.014.

[18] I.A. Choudhury, M.A. El-Baradie, Machinability of nickel-base super alloys: a general review, J. Mater. Process. Technol. 77 (1998) 278–284. doi:https://doi.org/10.1016/S0924-0136(97)00429-9.

[19] A. Pineau, S.D. Antolovich, High temperature fatigue of nickel-base superalloys – A review with special emphasis on deformation modes and oxidation, Eng. Fail. Anal. 16 (2009) 2668–2697. doi:https://doi.org/10.1016/j.engfailanal.2009.01.010.

[20] O.N. Senkov, S.L. Semiatin, Microstructure and properties of a refractory high-entropy alloy after cold working, J. Alloys Compd. 649 (2015) 1110–1123. doi:https://doi.org/10.1016/j.jallcom.2015.07.209.

[21] O.N. Senkov, G.B. Wilks, J.M. Scott, D.B. Miracle, Mechanical properties of Nb25Mo25Ta25W25 and V20Nb20Mo20Ta20W20 refractory high entropy alloys, Intermetallics. 19 (2011) 698–706. doi:https://doi.org/10.1016/j.intermet.2011.01.004.

[22] O.N. Senkov, J.M. Scott, S. V Senkova, F. Meisenkothen, D.B. Miracle, C.F. Woodward, Microstructure and elevated temperature properties of a refractory TaNbHfZrTi alloy, J. Mater. Sci. 47 (2012) 4062–4074. doi:10.1007/s10853-012-6260-2.

[23] D.B. Miracle, O.N. Senkov, A critical review of high entropy alloys and related concepts, Acta Mater. 122 (2017) 448–511. doi:https://doi.org/10.1016/j.actamat.2016.08.081.

[24] I. Tamura, H. Sekine, T. Tanaka, C. Ouchi, Chapter 3 - Deformation of austenite in the recrystallization region, in: I. Tamura, H. Sekine, T. Tanaka, C.B.T.-T.P. of H.-S.L.-A.S. Ouchi (Eds.), Butterworth-Heinemann, 1988: pp. 49–79.

doi:https://doi.org/10.1016/B978-0-408-11034-1.50006-4.

[25] I. Tamura, H. Sekine, T. Tanaka, C. Ouchi, Chapter 10 - Properties of controlled-rolled steels, in: I. Tamura, H. Sekine, T. Tanaka, C.B.T.-T.P. of H.-S.L.-A.S. Ouchi (Eds.), Butterworth-Heinemann, 1988: pp. 167–201. doi:https://doi.org/10.1016/B978-0-408-11034-1.50013-1.

[26] I. Tamura, H. Sekine, T. Tanaka, C. Ouchi, Chapter 11 - Prediction and control of microstructural change and mechanical properties in hot-rolling, in: I. Tamura, H. Sekine, T. Tanaka, C.B.T.-T.P. of H.-S.L.-A.S. Ouchi (Eds.), Butterworth-Heinemann, 1988: pp. 202–225. doi:https://doi.org/10.1016/B978-0-408-11034-1.50014-3.

[27] I. Weiss, S.L. Semiatin, Thermomechanical processing of beta titanium alloys—an overview, Mater. Sci. Eng. A. 243 (1998) 46–65. doi:https://doi.org/10.1016/S0921-5093(97)00783-1.

[28] J.H. Weber, Y. Khalfalla, K.Y.B.T.-R.M. in M.S. and M.E. Benyounis, Nickel Alloys: Thermal Treatment and Thermomechanical Processing, in: Elsevier, 2016. doi:https://doi.org/10.1016/B978-0-12-803581-8.03382-8.

[29] R.D. Doherty, D.A. Hughes, F.J. Humphreys, J.J. Jonas, D.J. Jensen, M.E. Kassner, W.E. King, T.R. McNelley, H.J. McQueen, A.D. Rollett, Current issues in recrystallization: a review, Mater. Sci. Eng. A. 238 (1997) 219–274. doi:https://doi.org/10.1016/S0921-5093(97)00424-3.

[30] F.J. Humphreys, M. Hatherly, Chapter 13 - Hot Deformation and Dynamic Restoration, in: F.J. Humphreys, M.B.T.-R. and R.A.P. (Second E. Hatherly (Eds.), Elsevier, Oxford, 2004: p. 415–V. doi:https://doi.org/10.1016/B978-008044164-1/50017-7.

[31] R.R. Eleti, T. Bhattacharjee, L. Zhao, P.P. Bhattacharjee, N. Tsuji, Hot deformation behavior of CoCrFeMnNi FCC high entropy alloy, Mater. Chem. Phys. 210 (2018)

176–186. doi:https://doi.org/10.1016/j.matchemphys.2017.06.062.

[32] J.Y. He, C. Zhu, D.Q. Zhou, W.H. Liu, T.G. Nieh, Z.P. Lu, Steady state flow of the FeCoNiCrMn high entropy alloy at elevated temperatures, Intermetallics. 55 (2014) 9–14. doi:https://doi.org/10.1016/j.intermet.2014.06.015.

[33] B. Schuh, B. Völker, J. Todt, N. Schell, L. Perrière, J. Li, J.P. Couzinié, A. Hohenwarter, Thermodynamic instability of a nanocrystalline, single-phase TiZrNbHfTa alloy and its impact on the mechanical properties, Acta Mater. 142 (2018) 201–212. doi:https://doi.org/10.1016/j.actamat.2017.09.035.

[34] C.-C. Juan, M.-H. Tsai, C.-W. Tsai, W.-L. Hsu, C.-M. Lin, S.-K. Chen, S.-J. Lin, J.-W. Yeh, Simultaneously increasing the strength and ductility of a refractory high-entropy alloy via grain refining, Mater. Lett. 184 (2016) 200–203. doi:https://doi.org/10.1016/j.matlet.2016.08.060.

Chapter 2

Deformation Behavior and Microstructure Evolution in High Temperature Processing of HfNbTaTiZr Refractory High Entropy Alloy

2.1. Introduction

Refractory HEAs (RHEAs) were firstly introduced by Senkov et al. [1]. RHEAs like NbMoTaW and VNbMoTaW have shown exceptional strength at temperatures above 1000°C, even superior to conventional superalloys and its compositional derivatives [2]. Thereby, RHEAs are expected as potential alloys for high temperature applications beyond the limits of conventional superalloys. On the other hand, mechanical properties of RHEAs at elevated temperatures, such as flow behaviors, deformation mechanisms, and microstructural changes, have not yet systematically studied by now, even though they are expected to be used as high temperature materials [3]. When HEAs are provided to commercial applications in future, the alloys would be fabricated through thermo-mechanically controlled processing (TMCP) at high temperatures in the same way as conventional metals and alloys commercially produced. TMCP can control not only shapes of the metal products but also their microstructures and textures by adjusting processing parameters, so that properties of the materials can be properly controlled. From these points of view, it is important to understand mechanical and microstructural responses of HEAs (especially RHEAs) in TMCP at high temperatures. Obtained TMCP responses would be also beneficial for understanding mechanical properties of the alloys at elevated temperatures.

The objective of the present chapter is to systematically understand deformation behaviors and microstructure evolution of an equiatomic HfNbTaTiZr RHEA during high-temperature processing. In the present study, the HfNbTaTiZr alloy is systematically deformed at different strain rates and temperatures where BCC single phase is stable (≥1000°C). Obtained stress-strain behaviors are analyzed, and evolution of microstructures and textures are carefully observed. Furthermore, mechanical responses at elevated temperatures are discussed in correlation with its microstructures and textures.

2.2. Experimental Procedures

2.2.1. Starting Material

An equiatomic HfNbTaTiZr alloy ingot 14 mm thick, 70 mm wide and 70 mm long was fabricated by vacuum arc melting from pure metals of constituent elements having 99.9 wt% or higher purities. Cu-K_α radiation using PANalytical, X'Pert PRO Alpha-1 was used to characterize phases in the as-cast material. Obtained XRD pattern of the as-cast alloy is shown in **Figure 2.1 a**. The XRD profile confirmed a single phase BCC structure. A microstructure of the as-cast alloy analyzed by electron back-scattering diffraction (EBSD) analysis in a scanning electron microscope (SEM) is shown in **Figure 2.1 b**. The figure exhibits an inverse pole figure (IPF) map where colors indicate crystallographic orientation parallel to the compression direction, according to the key stereographic triangle inserted. The EBSD analysis also confirmed the BCC single phase solid solution in the as-cast state, and the microstructure was a simple polycrystalline structure composed of equiaxed grains having grain sizes ranging from 150 μm to 300 μm. Voids were not observed in the as-cast material. Low angle grain boundaries with (LAGBs) misorientations (θ), $2° \leq \theta < 15°$ and high angle grain boundaries (HAGBs) with $\theta \geq 15°$ are shown in white and black lines, respectively.

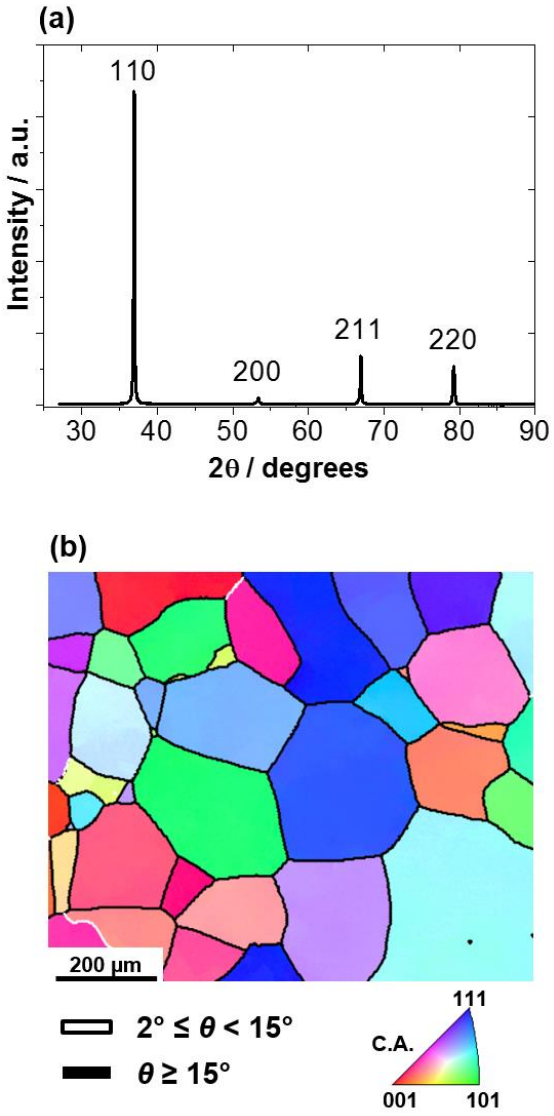

Figure 2.1 (a) XRD pattern of the as-cast equiatomic HfNbTaTiZr alloy, and (b) EBSD orientation map of the as-cast microstructure. Low angle grain boundaries with misorientations (θ), $2° \leq \theta < 15°$ and high angle grain boundaries with $\theta \geq 15°$ are shown in white and black lines, respectively.

2.2.2. Compression Tests

Cylindrical specimens for hot-compression tests, having dimensions 8 mm in diameter and 12 mm in height, were cut from the as-cast material by the use of an electric discharge wire-cutting machine. Uniaxial compression tests were carried out in a thermo-mechanical processing simulator (model: Thermecmastor-Z, Fuji Electronic Industrial Company Ltd.). Before commencement of the test, the deformation chamber was evacuated until 2.0×10^{0} Pa using rotary pump connected to the chamber. Later, the chamber was filled with the inert Ar gas. Therefore, the high temperature experiments were performed virtually in the vacuum atmosphere with no concern for oxidation. **Figure 2.2** schematically illustrates the thermo-mechanical processing patterns tested in the present study. The specimens were heated from room temperature to a set deformation temperature at a heating rate of 10°C s^{-1} by an induction heating system equipped in the physical simulator and held isothermally for 900 seconds before compression to homogenize temperature of the specimens. For precise temperature control and measurement, a thermocouple was welded at mid-height positions on side surfaces of the cylindrical specimens. Uniaxial compression was carried out by 50% reduction in height (corresponding true strain (ε) of 0.69) at different temperatures (1000°C, 1100°C, and 1200°C) and different strain rates (10^{-4} s^{-1}, 10^{-3} s^{-1}, and 10^{-2} s^{-1}). Mica plates and glass powder were used as insulator and lubricant in the compression, respectively. The high temperature process was carried out in a vacuum atmosphere. The specimens were quenched by water immediately after the compression to freeze microstructures and provided for microstructural observations.

2.2.3. Microstructural and Crystallographic Analyses

For microstructural observations, hot-compressed specimens were cut vertically through the center. The cut surfaces parallel to the compression direction were mechanically polished until achieving scratch-free surfaces and then electropolished to get mirror-like surfaces. Electropolishing was carried out in a chemical solution with 10 vol.%

perchloric acid and 90 vol.% methanol at -20°C at a constant voltage of 20V for 30sec. Microstructural observations were carried out at the center of the polished sections of the hot-compressed specimens. Electron back-scattering diffraction (EBSD) system operated in a field emission-scanning electron microscope (FE-SEM, JSM 7100F) at an accelerated voltage of 20 kV was used to obtain microstructural and crystallographic information. The EBSD scans were carried out at a step size of 0.3 μm or 0.1 μm, depending on sizes of observed areas and purpose. Sound Kikuchi patterns sufficient for analyzing orientations were acquired even in unrecrystallized regions. For investigating textures of the hot-compressed specimens, obtained EBSD data were analyzed by orientation imaging microscopy (OIM) technique using a software, TSL OIM Analysis 7.

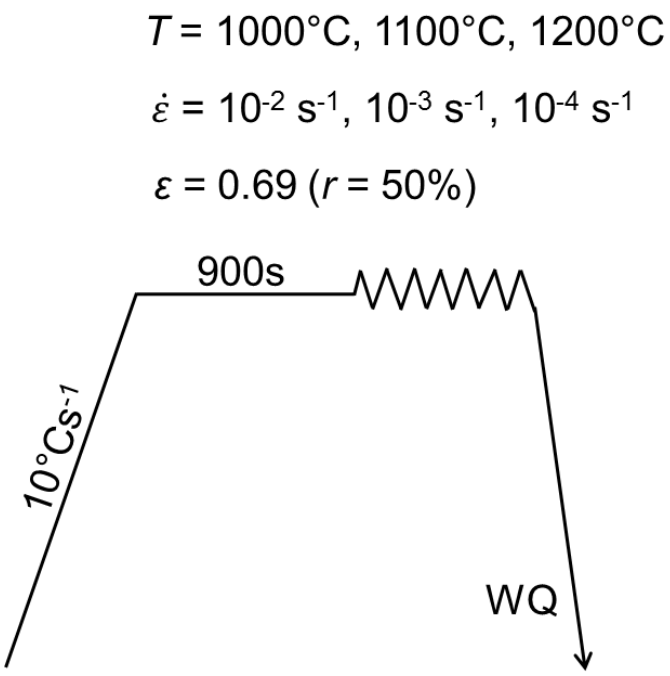

Figure 2.2 Schematic diagram showing the experimental procedure and processing conditions in the hot-compression tests.

2.3. Results

2.3.1. Stress-Strain Behaviors

Figure 2.3 shows stress-strain curves of the equiatomic HfNbTaTiZr alloy hot-compressed at different deformation temperatures and different strain rates. Stress-strain curves under most deformation conditions showed a characteristic behavior, i.e., a sharp drop of the flow stress at a very early stage of deformation, followed by a continuous decrease of the flow stress. The flow stress decreased with increasing the deformation temperature or decreasing the strain rate. Increase in the deformation temperature and decrease in the strain rate reduced the peak stress as well as the magnitude of the stress drop, as summarized in **Figure 2.4**. One of the important aspects observed from the stress-strain curves is the absence of work-hardening after the peak stress. Such plastic flow behaviors are discussed in the later part, associated with microstructural features.

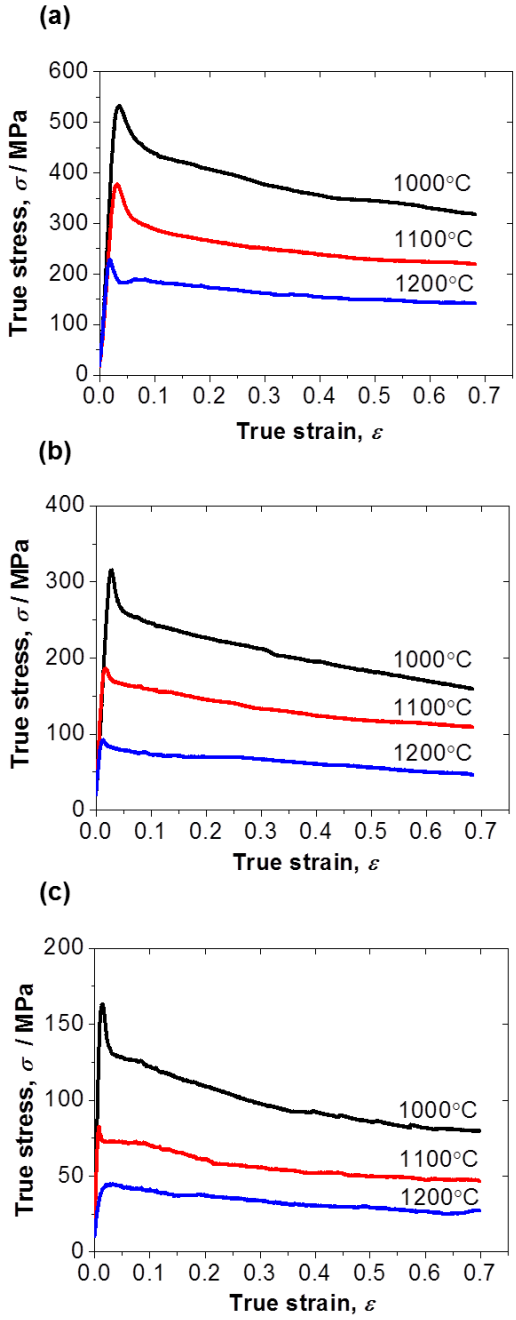

Figure 2.3 True stress-strain curves of the equiatomic HfNbTaTiZr at different deformation temperatures and different strain rates. (a) Strain rate of 10^{-2} s^{-1}, (b) 10^{-3} s^{-1}, (c) 10^{-4} s^{-1}.

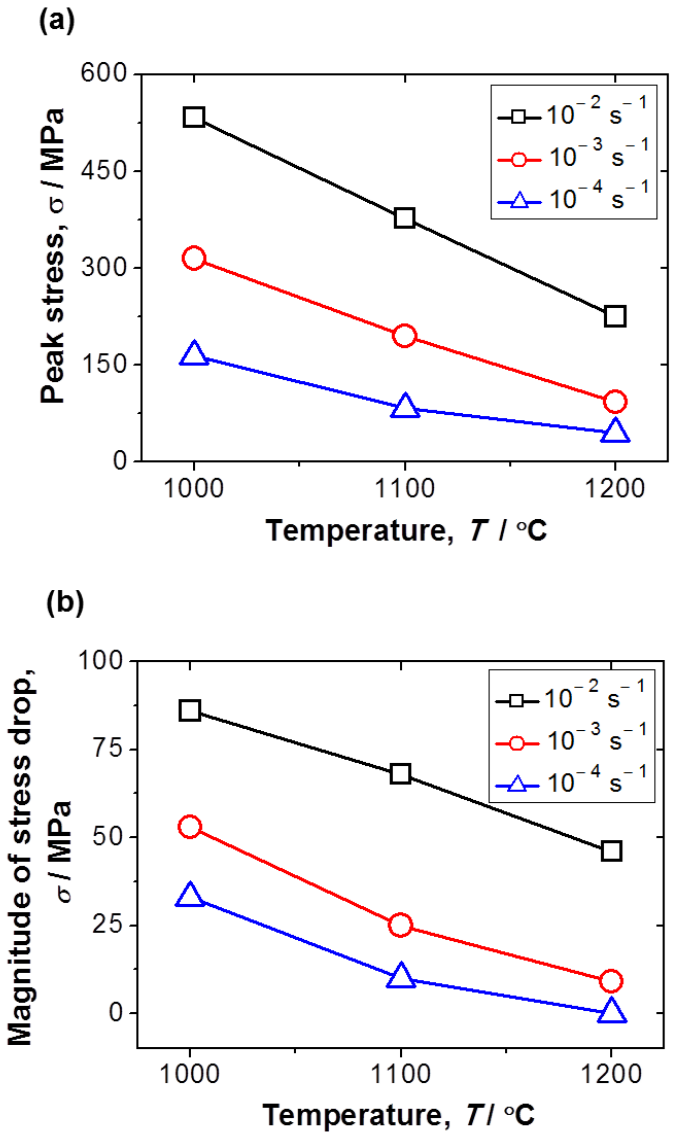

Figure 2.4 Effects of deformation temperatures and strain rates on (a) the peak stress, and (b) the magnitude of stress drop.

2.3.2. Flow Stress Analysis

For optimizing deformation conditions at high temperatures to control microstructure and texture of the present alloy in future, a constitutive relationship between deformation factors, i.e., flow stress (σ), deformation temperature (T), strain rate ($\dot{\varepsilon}$), and strain (ε), should be understood. The relationship between these factors is expressed as an appropriate constitutive equation. The flow stress analysis was carried out by using a widely accepted Arrhenius-type power law relationship [4,5],

$$\dot{\varepsilon} = A\,\sigma^{n} \exp(-Q/RT) \tag{2.1}$$

where, $\dot{\varepsilon}$ is the strain rate (s^{-1}), A a material constant, σ the flow stress (MPa) at a constant strain (or the steady-state stress), n the stress exponent, Q the activation energy for hot-deformation (kJ mol^{-1}), R the gas constant (8.314 J $K^{-1}mol^{-1}$), and T the deformation temperature (K). Stress-strain data obtained from the present experiments (**Figure 2.3**) were used to determine the constants. In general, the activation energy for hot-deformation (Q) is estimated by differentiating **Equation 2.1** with respect to the deformation temperature and strain rate that yields the following equation,

$$Q = R[\partial \log(\dot{\varepsilon})/\partial log\,(\sigma)]_{T}[\partial \log(\sigma)/(1/T)]_{\dot{\varepsilon}} \tag{2.2}$$

For calculating the apparent activation energy (Q), the flow stresses ($\log(\sigma)$) at $\varepsilon = 0.1$ were plotted as log(strain rate) as a function of ($\log(\sigma)$) and as a function of $1/T$ in **Figure 2.5 a** and **Figure 2.5 b**, respectively. Linear relationships nearly parallel for different strain rates were obtained. Average values of the slopes obtained from **Figure 2.5 a** and **Figure 2.5 b** were 3.2 and 4.6 respectively. These two quantities gave the apparent activation energy of

~124 kJmol-1 at the specified strain ε = 0.1. The apparent activation energy for the hot-deformation was also estimated at each strain and shown in **Figure 2.5 c**. The apparent activation energy obtained gradually decreased with increasing the strain, but all values were within a narrow range of 123 ~ 114 kJmol^{-1}. Especially, the activation energy after strain of 0.3 was nearly constant (113~114 kJ mol^{-1}). The relatively large activation energy at a strain of 0.1 (124 kJ mol^{-1}) is probably affected by the stress drop observed in the stress-strain curves (**Figure 2.3**). Senkov et al. [6] has reported an activation energy (*Q*) of ~226 kJmol^{-1} for hot-deformation of the same alloy, which is higher than the values obtained in the present study (123 ~ 114 kJ mol^{-1}). The observed difference might be due to differences in the selected deformation conditions. They studied the hot-deformation of equiatomic HfNbTaTiZr alloy in uniaxial compression at temperatures of 800°C ~ 1200°C and strain rates of 10^{-3} s^{-1} ~ 10^{-5} s^{-1} [6]. They also reported that the HfNbTaTiZr alloy showed high strength and susceptible to deformation twinning during deformation in the intermediate temperatures (<1000°C). It should be noted, furthermore, they also reported second-phase nano-particles precipitated during deformation at intermediate temperatures. Consequently, the high strength and the operation of different deformation mechanisms could be a reason for the difference in the obtained *Q* values. It is worth reminding that the present high temperature deformation was carried out where BCC single phase is stable (≥1000°C). The *Q* value obtained in the present study is lower than the *Q* for self-diffusion of pure BCC elements included in the HfNbTaTiZr alloy but somehow close to the *Q* of high-temperature β phase (BCC) of Ti and Zr. **Table 2.1** shows the activation energy for the self-diffusion of different elements [7]. Although *Q* for high temperature deformation is often correlated to the rate-controlling mechanism governed by different kinds of diffusion, the lack of diffusion data in the present alloy limits consideration between the rate-controlling mechanism and *Q* obtained in the present study.

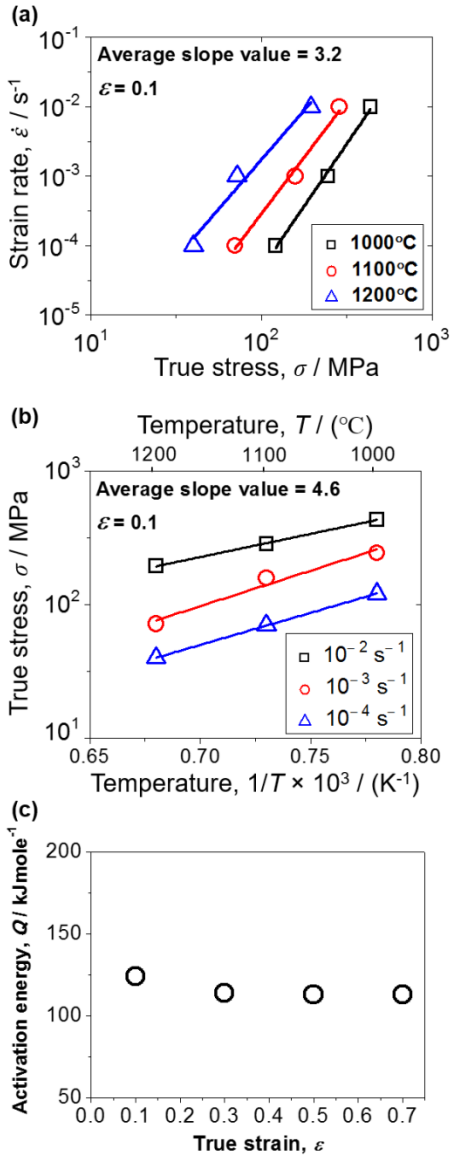

Figure 2.5 Flow stress analysis of the HfNbTaTiZr alloy showing linear fit for the (a) flow stress vs. strain rate and (b) flow stress vs. $1/T$ obtained from the flow stresses at strain ε = 0.1, (c) The estimated apparent activation energy for hot deformation of HfNbTaTiZr plotted as a function of strain, ε.

Table 2.1 Activation energy for self-diffusion of different elements and the temperature ranges.

Element	α (HCP) – β (BCC) Transition temperature (°C)	Available data for the activation energy for self-diffusion	Activation energy for Self-diffusion, Q_s (kJmol^{-1})	References
Hf	1743°C	Above β-transition temperature	162 kJmol^{-1}	[7,8]
Ti	882°C		130 kJmol^{-1}	
Zr	862°C		116 kJmol^{-1}	
Nb	-	1080°C - 2420°C	436 – 350 kJmol^{-1}	
Ta	-	1827°C - 2527°C	516 – 386 kJmol^{-1}	

It is well known that two variables in hot-deformation, i.e., deformation temperature (T) and strain rate ($\dot{\varepsilon}$), can be combined into a single parameter, Zener-Hollomon parameter (Z) [9], given as,

$$Z = \dot{\varepsilon} \exp(Q/RT) \tag{2.3}$$

The Z parameter is considered as a temperature-compensated strain rate having the unit of s^{-1}. Comparing **Equation 2.1** with **Equation 2.3**, a relationship shown below is obtained:

$$\log(Z) = \log(A) + n \log(\sigma) \tag{2.4}$$

In **Figure 2.6**, flow stresses at different strains are plotted against Z in log-log scales. The apparent activation energy (Q) obtained at each strain in **Figure 2.5** was used for calculating Z by **Equation 2.3**. At each strain, the flow stresses laid on a single straight line. Although there were slightly different tendencies between different strain rates, they were possibly because the flow stresses did not reach steady-states. From **Figure 2.6**, nearly constant strain exponent, n = 2.8 ~ 2.9, was obtained.

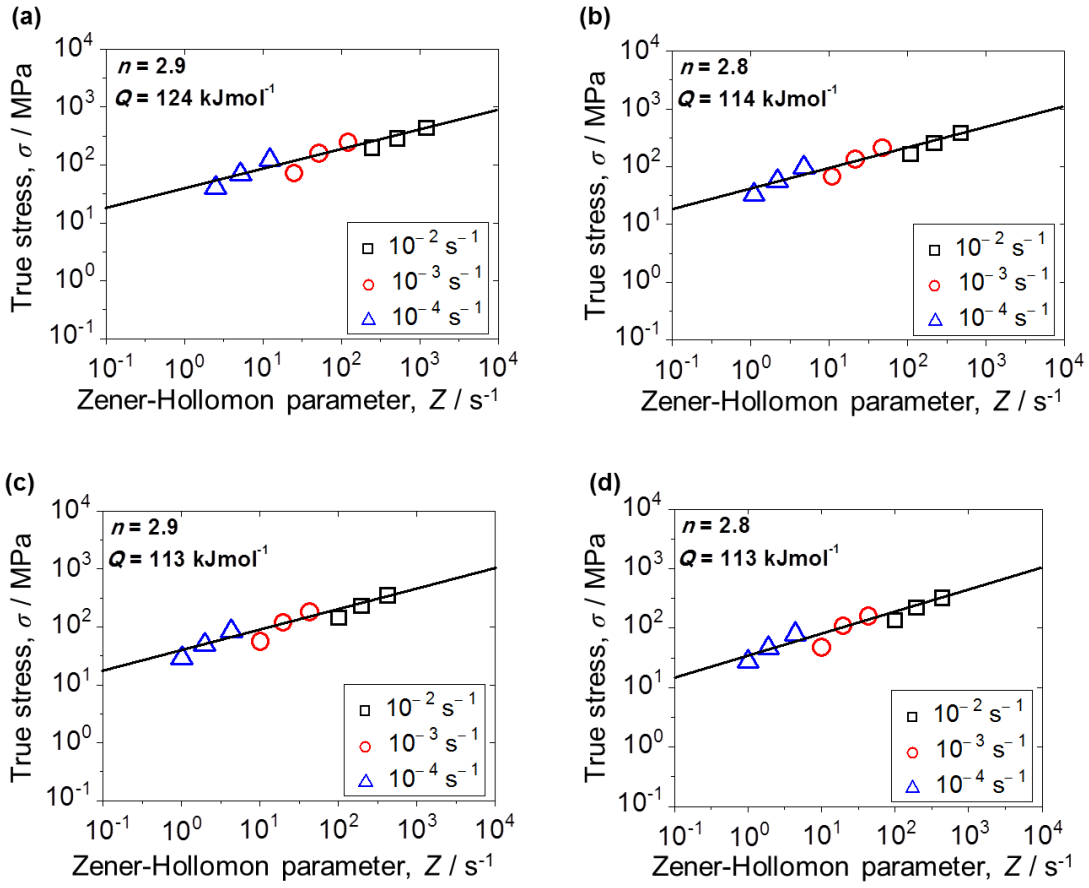

Figure 2.6 Flow stresses at different strains ((a) ε = 0.1, (b) ε = 0.3, (c) ε = 0.5, (d) ε = 0.69) plotted as a function of Zener-Hollomon parameter (Z). The activation energy (Q) obtained at each strain in **Fig.2.5** was used for calculating Z.

2.3.3. Microstructure Evolution

Inverse pole figure (IPF) maps obtained by the EBSD analysis of the HfNbTaTiZr specimens hot-compressed by 50% reduction (ε = 0.69) at different temperatures and strain rates are shown in **Figure 2.7**. Colors in the IPF maps indicate crystallographic orientations parallel to the compression axis (C.A.) according to the key stereographic triangle shown in the figure. In most of the specimens, fine, equiaxed grains were observed along initial grain boundaries to form necklace-like structures. The necklace structure composed of fine-grains is visually shown in **Figure 2.8** for the specimen deformed at 1000°C and 10^{-2} s^{-1}. The high magnification EBSD maps clearly revealed fine dynamically recrystallized (DRX) grains. Similar approach was used to obtain valid information on DRX grain size for all deformation conditions in the present study. Both fractions and grain size of the fine, equiaxed grains increased with increasing the deformation temperature or decreasing the strain rate. In the specimen deformed at 1200°C and 10^{-4} s^{-1} (**Figure 2.7 i**), more homogeneous microstructure composed of coarse, equiaxed grains was observed, rather than the necklace structures. Initial grains surrounded by the necklace structures of fine, equiaxed grains were elongated to directions perpendicular to C.A. They mostly showed red or blue colors including color gradations inside, which indicates that the elongated initial grains preferentially have <001> or <111> orientations parallel to C.A. and involve misorientations inside. The <001> and <111> orientations parallel to C.A. are known as the typical deformation texture of BCC metals and alloys deformed in compression [10]. On the other hand, the necklace structures seemed not to have preferred orientations.

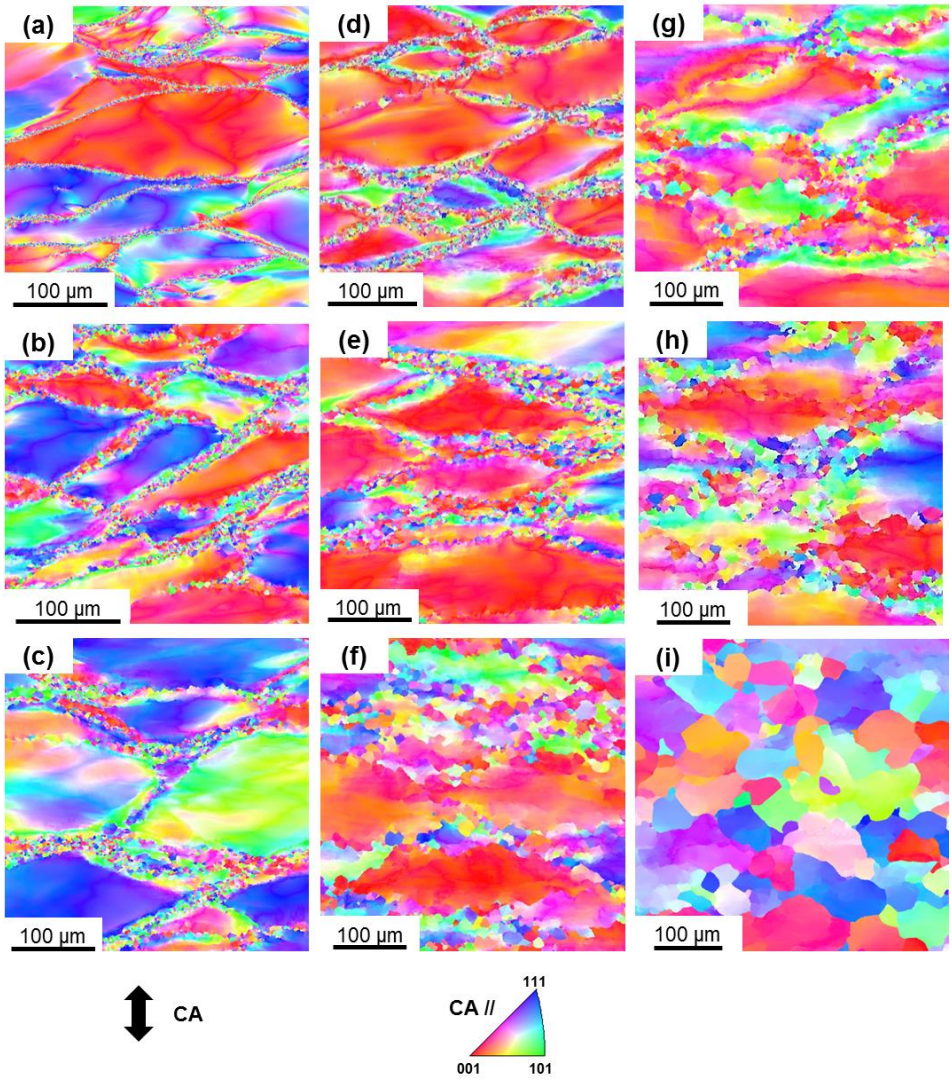

Figure 2.7 EBSD inverse pole figure (IPF) maps of the specimens hot-compressed to 50% reduction (ε = 0.69) at various temperatures and strain rates. (a-c) Deformed at a strain rate of 10^{-2} s^{-1}, (d-f) 10^{-3} s^{-1}, and (g-i) 10^{-4} s^{-1}. (a,d,g) Deformed at 1000°C, (b,e,h) 1100°C, and (c,f,i) 1200°C. Colors in the IPF maps indicate crystallographic orientations parallel to the compression axis (C.A.), according to the key stereographic triangle indicated in the figure. The C.A. direction is parallel to the vertical direction of the microstructures.

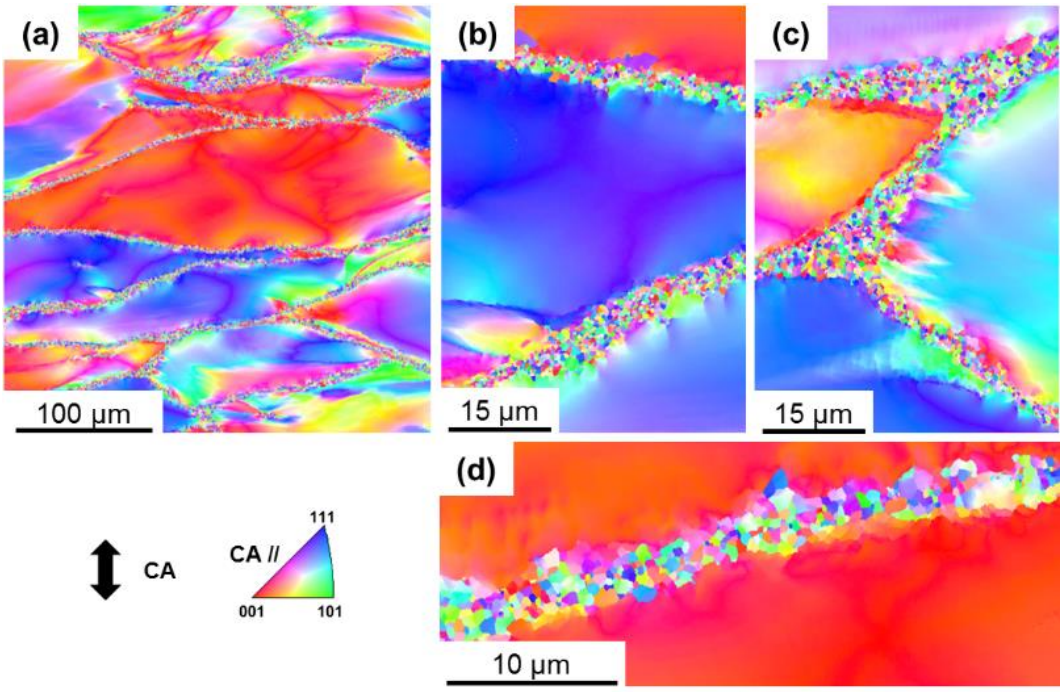

Figure 2.8 EBSD inverse pole figure (IPF) maps of the specimen hot-compressed to 50% reduction (ε = 0.69) at 1000°C and 10^{-2} s^{-1}. (a) EBSD IPF map showing necklace-like structure. (b-d) EBSD IPF maps at relatively high-magnification confirmed necklace structure composed of fine DRX grains. The C.A. direction is parallel to the vertical direction of the microstructures.

The observed necklace structures of fine, equiaxed grains are typically observed in metals and alloys dynamically recrystallized during hot-deformation [11]. The temperature and strain rate dependences of the necklace structures obtained in this study agreed with the features of dynamic recrystallization (DRX). **Figure 2.9** shows grain boundary maps superimposed on image quality (IQ) maps obtained by the EBSD measurement and analysis, where red and blue lines indicate low angle grain boundaries (LAGBs) having misorientations (θ), $2° \leq \theta < 15°$, and high angle grain boundaries (HAGBs) with $\theta \geq 15°$, respectively. The IQ corresponds to the quality of Kikuchi-line obtained at each measurement point in the EBSD mapping. **Figure 2.9** clearly indicates that most of the fine

and equiaxed grains in the necklace structures are surrounded by blue HAGBs. Thus, it can be concluded that the fine and equiaxed grains are recrystallized grains. As all the specimens were water-quenched immediately after the compression deformation, it is also possible to conclude that the fine and equiaxed grains are DRX grains formed during the deformation. The more homogeneous microstructure composed of coarse grains observed in the specimen deformed at 1200°C and 10^{-4} s^{-1} (**Fig.2.9 i**) probably corresponds with grain growth of DRX grains. It should be noted, by the way, that necklace DRX structures have been typically observed in face-centered cubic (FCC) metals and alloys with medium or low stacking-fault energies but rarely observed in BCC metals and alloys. In this sense, the clear necklace structures of DRX grains observed in the present study are characteristic in the HfNbTaTiZr BCC-HEA.

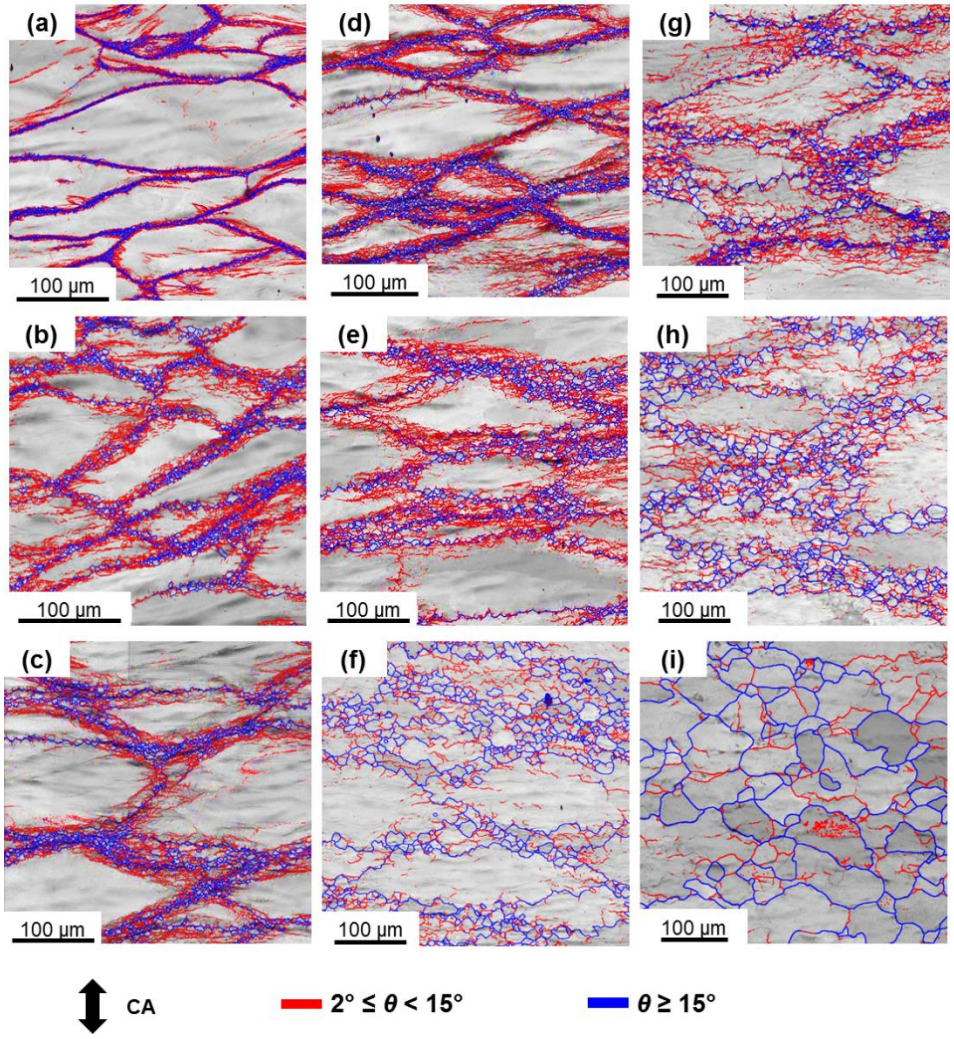

Figure 2.9 EBSD grain boundary and image quality (IQ) maps of the specimens hot-compressed to 50% reduction (ε = 0.69) at various temperatures and strain rates. (a-c) Deformed at a strain rate of 10^{-2} s^{-1}, (d-f) 10^{-3} s^{-1}, and (g-i) 10^{-4} s^{-1}. (a,d,g) Deformed at 1000°C, (b,e,h) 1100°C, and (c,f,i) 1200°C. Low angle grain boundaries with misorientations (θ), $2° \leq \theta < 15°$ and high angle grain boundaries with $\theta \geq 15°$ are shown in red and blue lines, respectively. The C.A. direction is parallel to the vertical direction of the microstructures.

DRX grains could be distinguished from unrecrystallized matrix in the EBSD microstructures by the use of grain orientation spread (GOS) parameter. The GOS represents degree of orientation spread in each grain, which is obtained by measuring misorientation between EBSD data points within a grain and averaging the misorientations [12]. DRX grains should involve lower misorientation inside than the unrecrystallized matrix, since DRX grains newly appear at later stages of deformation. A worked out example for separating DRX grains from the overall microstructure using GOS approach is shown in **Figure 2.10**. In the present microstructures, DRX grains could be successfully extracted as the grains having GOS $\leq 2°$. Here, the grains were determined as the regions surrounded by HAGBs. The DRX fraction and the average sizes of DRX grains quantitatively evaluated from the GOS-based analysis are plotted as a function of Z in **Figure 2.11 a**-**b**, respectively. Here an apparent activation energy Q = 113 kJ mol^{-1} was used to calculate Z. As was qualitatively observed in **Figures 2.7** and **2.8**, the DRX fraction and grain size both decreased with increasing Z (i.e., with decreasing the deformation temperature or increasing the strain rate). However, the changes in the DRX fraction and grain size were not perfectly smooth but had gaps between different strain rates. The gaps seemed to correspond to those observed in **Figure 2.6**, which suggests that the Z parameter used in this study does not perfectly describe the hot-deformation behaviors. Thus, the DRX fractions and grain size were re-plotted as a function of the flow stress (log σ) in **Figure 2.11 c**-**d**, respectively. **Figure 2.11** showed that the DRX fraction and grain size both decreased with increasing the flow stress, and they laid on smoother tendencies than those plotted against Z. The tendencies agreed with typical features observed in DRX of metals and alloys [13,14]. It is noteworthy that the specimens deformed under relatively high Z conditions, like 1000°C / 10^{-2} s^{-1} and 1100°C / 10^{-2} s^{-1}, showed ultrafine grain sizes of 0.7 μm and 1.2 μm respectively. It is surprising that such ultrafine grain sizes were obtained from DRX at high temperatures (> 1000°C) in BCC crystals, even though they were partially recrystallized microstructures. It can be concluded that grain growth of the DRX grains in the hot-deformed HfNbTaTiZr BCC-HEA is greatly suppressed, which might be related to sluggish diffusion expected in HEAs [15].

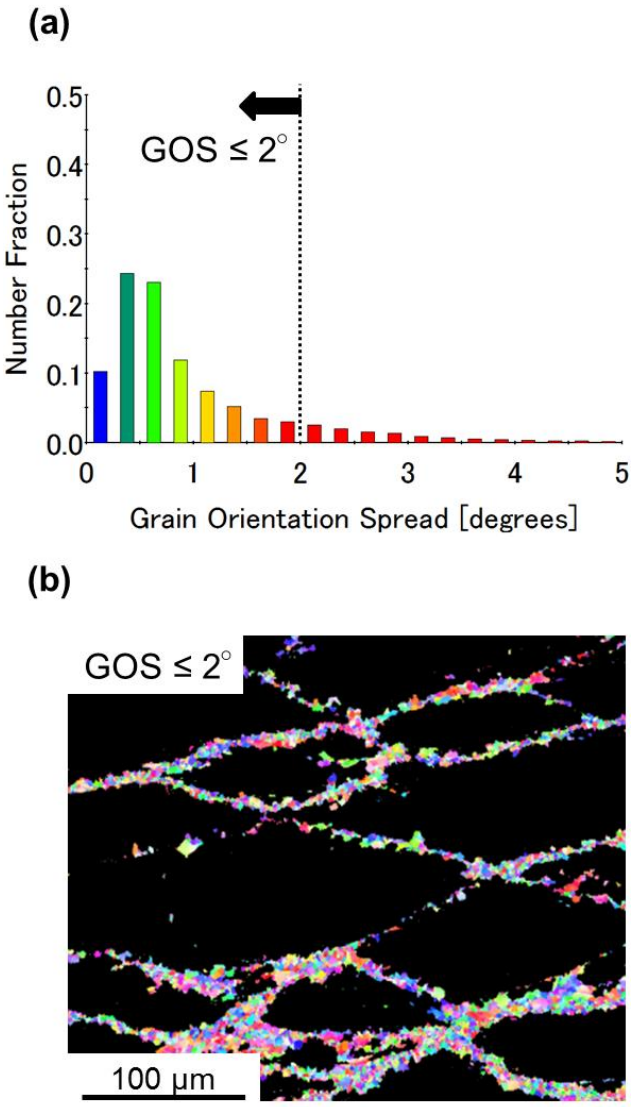

Figure 2.10 DRX grains were separated from the overall microstructure based on grain orientation spread (GOS) approach in EBSD analysis. (a) Example of GOS distribution in a dynamically recrystallized specimen deformed to a strain of ε ~0.69 at 1000°C and 10^{-3} s^{-1}, showing the selected criteria *GOS* ≤ *2°* for separating DRX grains from overall microstructure. (b) EBSD IPF map showing DRX grains extracted using the criteria *GOS* ≤ *2°*. Unrecrystallized regions are painted black.

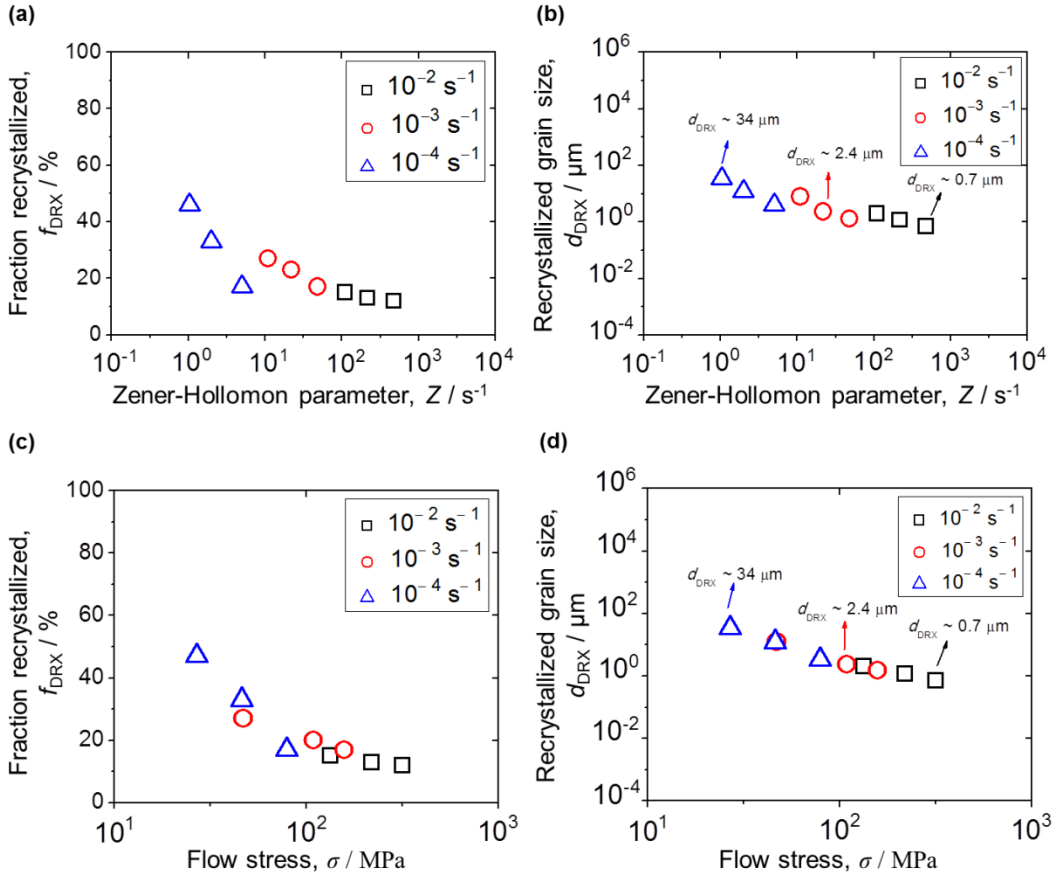

Figure 2.11 (a) Fraction recrystallized (f_{DRX}) and (b) DRX grain size (d_{DRX}) in the specimens hot-compressed by 50% reduction (ε = 0.69) plotted as a function of Zener-Hollomon parameter (Z). (c) Fraction recrystallized (f_{DRX}) and (d) DRX grain size (d_{DRX}) in the specimens hot-compressed by 50% reduction (ε = 0.69) plotted as a function of the flow stress (σ).

2.4. Discussions

2.4.1. Stress Drop at High Temperature

Sharp drops of the flow stress were clearly observed at early stages of hot-compression in the HfNbTaTiZr HEA (**Figure 2.3**). Stress-drops in hot-deformation of HfNbTaTiZr were also reported by Senkov et al. [6]. Generally speaking, such a sharp drop of the flow stress (or yield-drop) is considered to be caused by scarcity of mobile dislocations in metallic materials [16]. Well-known yield-drop phenomenon in carbon steels is a typical example, where dislocations are pinned by solute carbon atoms (Cottrell atmosphere) [17]. In the present case, however, pinning of dislocations by interstitial solute atoms like carbon is not likely to occur, since the deformation was carried out at high temperatures (≥1000°C). One possible situation is dislocation locking by substitutional solute elements. In fact, yield-drop like phenomena have been reported in Fe-Mo [18], Al-Mg [19] and β-Ti alloys [20].

For checking the possibility, interrupted compression tests at high temperature were carried out for the HfNbTaTiZr alloy specimens. The specimens were heated up to 1000°C, held for 900 s, and then compressed at a strain rate of 10^{-3} s^{-1}, in the same way shown in **Figure 2.2**. In the interrupted tests, however, the compression was stopped at a strain of $\varepsilon \sim 0.1$, and then re-started after an interval of 0 s, 120 s, 300 s, or 600s. The resultant stress-strain curves are shown in **Figure 2.12**. All the specimens showed clear stress-drops in the first step of deformation up to $\varepsilon \sim 0.1$. It could be found that the specimen re-loaded after an interval of 0 s did not show the stress-drop again, but the stress-strain curve smoothly came back to the extrapolation of the curve in the first-step deformation and the total stress-strain curve was continuous. On the other hand, when the specimens were held for 120 s, 300 s, or 600 s at 1000°C till re-loading, the stress-strain curves again showed stress-drops at the beginning of the second-step of deformation. Furthermore, the stress-drop became sharper and the amount of the stress-drop became larger with increasing the holding time at 1000°C in **Figure 2.12**. The results clearly suggest that there were enough amounts of free dislocations introduced in the first-step deformation in the crystals when

the second-step deformation was started immediately after the interruption. On the other hand, dislocations introduced in the first-step deformation were again locked during holding at high temperature after the interruption. Probably any solute atoms (or any element(s)) diffused to make atmosphere around dislocations during holding at 1000°C after the interruption of the first deformation. The present experimental result indicated that the magnitude of the stress drop decreased with increasing the deformation temperature or decreasing the strain rate (**Figures 2.3** and **2.4**) supports such a consideration, since more chances of thermal activation for unlocking the dislocation-solute interaction are expected at higher temperature and lower strain rate.

It can be concluded that the sharp stress-drop (yield-drop) observed in the hot-deformation of HfNbTaTiZr is probably due to dislocation unlocking by any solute atoms. Here, however, it is impossible to distinguish solvent and solutes in equi-atomic HEAs including the present HfNbTaTiZr alloy. Thus it is difficult so far to conclude which element(s) in the present HfNbTaTiZr alloy induces the dislocation locking phenomenon. Originally it has been considered that crystal lattices of equi-atomic HEAs are locally distorted because of the mixture of atoms having different atomic radii. For understanding the essential physics of plastic deformation in such equi-atomic HEAs, to clarify the solute-dislocation interaction observed in the present study would be important in future.

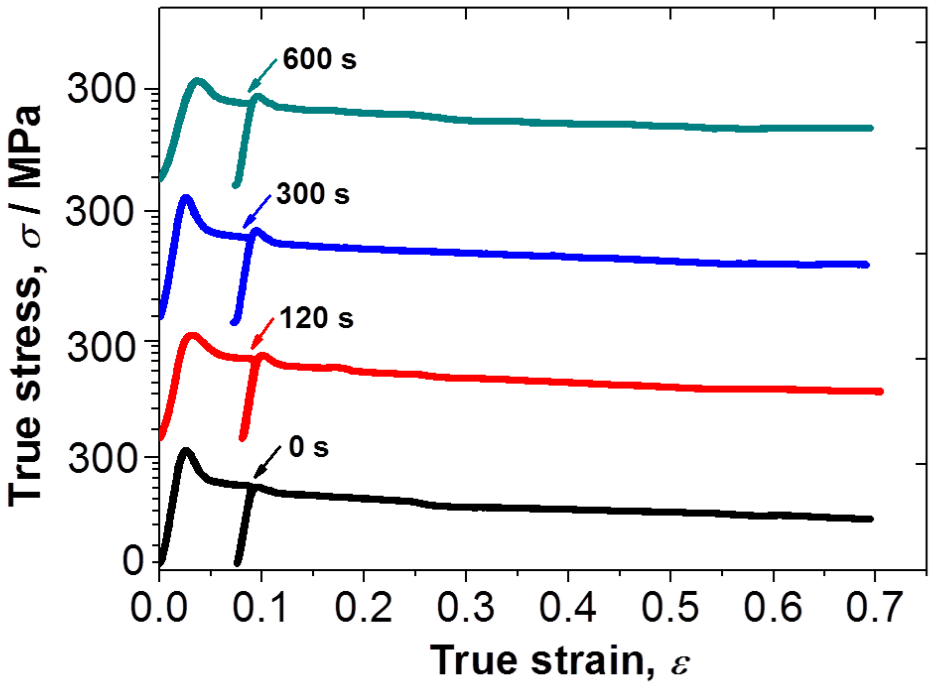

Figure 2.12 Stress-strain curves obtained from the interrupted compression test, where the compression tests at 1000°C and 10^{-3} s^{-1} were stopped at a strain of ~0.1 and then re-started after an interval (holding) for 0 s, 120 s, 300 s, or 600 s.

2.4.2. Correlation between Microstructure and Flow Stress

The reason for the sharp stress-drop observed at early stage of hot-deformation in the present HfNbTaTiZr alloy was discussed and clarified in the former section. In the present section, the gradual decrease in the flow stress (gradual softening) after the stress drop is discussed, correlating with the microstructure evolution observed. Dynamic recrystallization (DRX) is one of the softening processes that simultaneously occur during deformation at elevated temperatures. DRX grains often appear along initial grain boundaries (GBs) [11,21]. In the present study, DRX grains formed along initial grain

boundaries and resultant necklace structures were confirmed under most deformation conditions (**Figures 2.7** and **2.9**). The result indicates that DRX is one of the primary softening processes. DRX has been observed mostly in the materials where dynamic recovery (DRV) process is suppressed. This is because DRV decreases the dislocation density in crystals. The high dislocation density is however the driving force for recrystallization. Face-centered cubic (FCC) metals and alloys having medium or low stacking fault energies often exhibit DRX due to their limited DRV. On the contrary, it is known that DRV is enhanced to occur in BCC metals and alloys and in FCC metals and alloys having high stacking fault energies (like aluminum and its alloys), so that DRX in those materials are limitedly reported [11,21]. In BCC metals and alloys, diffusivity of atoms is originally higher owing to their looser packing of atoms than FCC crystals. Additionally, cross-slip of screw dislocations is easy to occur in BCC and high stacking-fault energy FCC. They are the reasons for the enhanced DRV (and the suppressed DRX) in those materials. In that sense, it is quite interesting that typical necklace-type DRX easily happened and very fine grain sizes of the DRX grains were observed in the present BCC HEA (HfNbTaTiZr). It has been proposed that HEAs exhibit sluggish diffusion as one of their natures [15]. Eleti et al. [22] and Stepanov et al. [23] have reported enhanced DRX in CoCrFeMnNi equi-atomic HEA during hot-deformation. The FCC HEA (CoCrFeMnNi) also showed typical necklace structures composed of very fine DRX grains, which is similar to the present result in the BCC HfNbTaTiZr alloy. The experimental evidences of enhanced DRX and resultant fine DRX grains in two kinds of HEAs having different crystal structures might suggest a possibility of sluggish diffusion leading to the suppression of DRV in HEAs regardless of crystal structure.

The gradual decrease in the flow stress with the progress of hot deformation observed in the present study (**Figure 2.3**) might be explained by the occurrence of DRX. However, as was shown in **Figure 2.11 a**, the fractions recrystallized in microstructures were always low (less than 50% and in most cases below 30%) even after 50% compression (ε = 0.69) in the present alloy. In other words, most of the areas in microstructures were unrecrystallized (and thus strain-hardened) during the present hot-

deformation, which seems somehow contradictory to the continuous softening. **Figures 2.13** and **2.14** show inverse pole figures of the unrecrystallized regions and recrystallized regions, respectively in the specimens hot-compressed by 50% at different temperatures and strain rates. The unrecrystallized and recrystallized regions were distinguished by the use of the criterion, GOS $\leq 2°$, described in the section 2.3.3. As was qualitatively observed in the IPF color maps (**Figure 2.7**), unrecrystallized regions showed <001> and/or <111> fiber textures. They are typical compression texture in BCC metals, which indicates that the unrecrystallized initial grains were plastically deformed by conventional dislocation slips, like {110}<111>, {112}<111>, and {123}<111> [10]. That is, the unrecrystallized matrix having major portions in microstructures should be certainly strain-hardened more or less during the hot-deformation. Although the present alloy has BCC crystal structure, DRV might be suppressed, as was discussed above. On the other hand, DRX grains did not have preferred orientation but showed rather random orientation distribution in **Figure 2.14**.

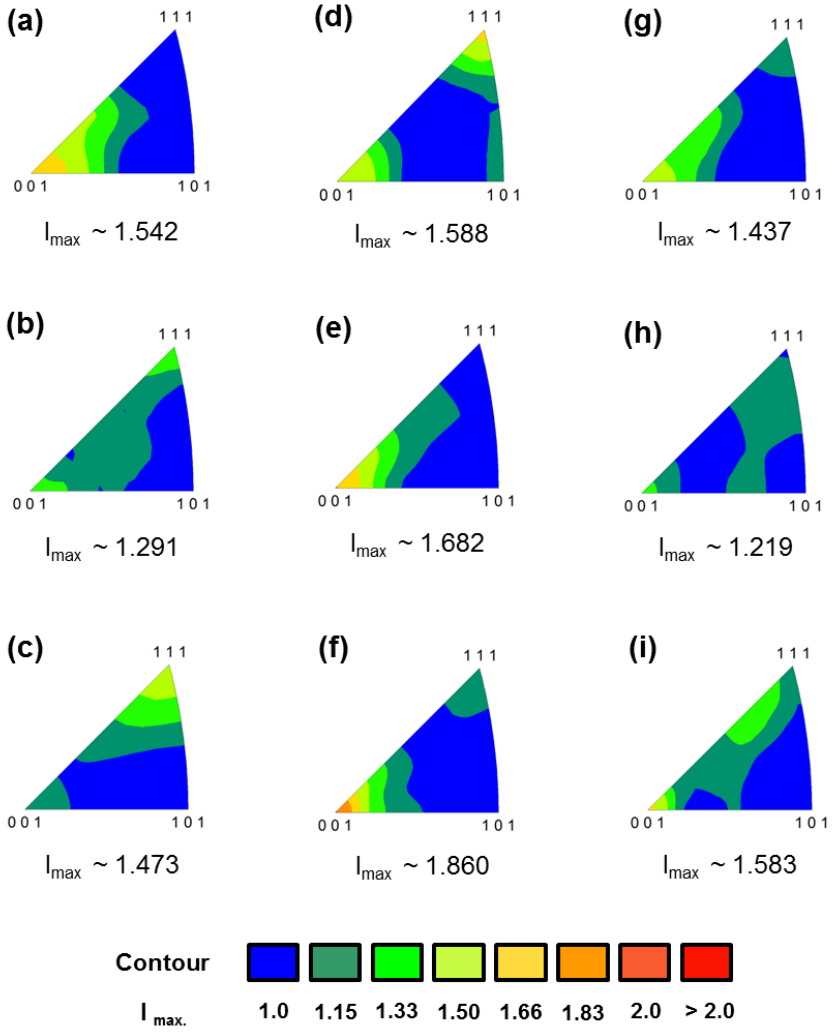

Figure 2.13 EBSD inverse pole figures (IPF) showing crystallographic orientations parallel to the compression axis (C.A.) of the unrecrystallized regions (*GOS* > *2*°) in the specimens 50% hot-compressed at various temperatures and strain rates. (a-c) Deformed at a strain rate of 10^{-2} s^{-1}, (d-f) 10^{-3} s^{-1}, and (g-i) 10^{-4} s^{-1}. (a,d,g) Deformed at 1000°C, (b,e,h) 1100°C, and (c,f,i) 1200°C. Colors in IPFs indicate intensities according to the scale shown in the figure. I_{max} indicates the maximum intensity in each IPF plot.

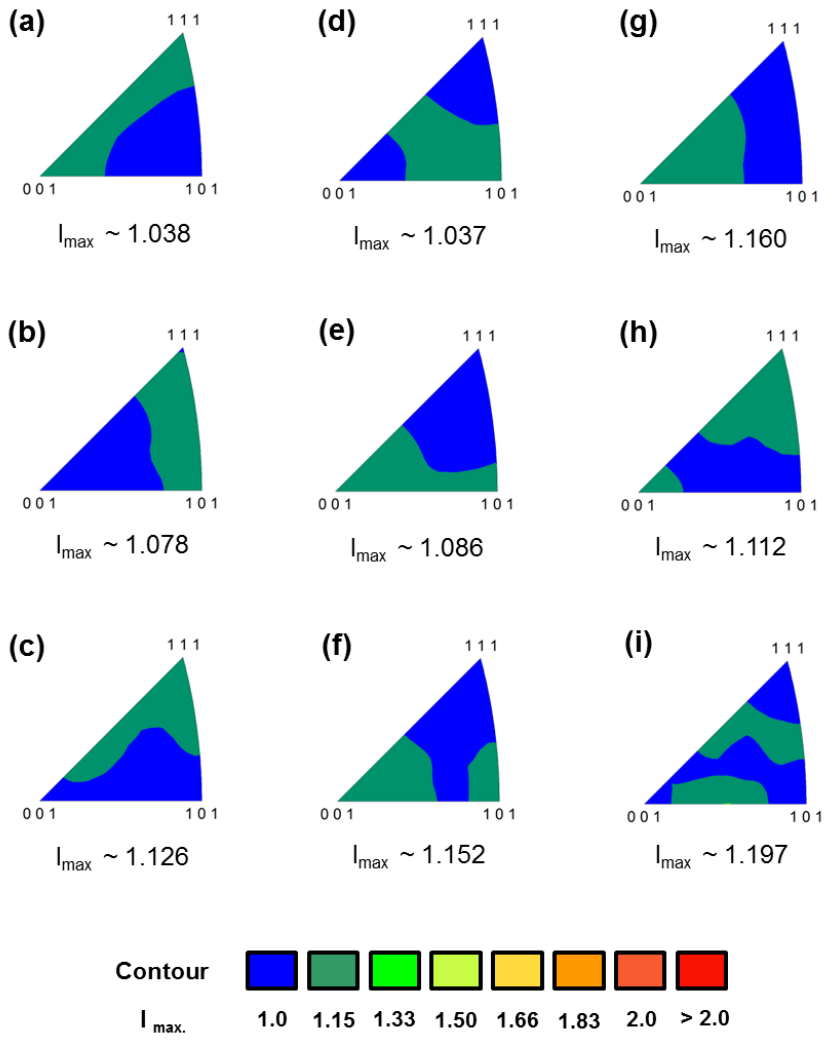

Figure 2.14 EBSD inverse pole figures (IPF) showing crystallographic orientations parallel to the compression axis (C.A.) in dynamically recrystallized regions ($GOS \leq 2°$) in the specimens 50% hot-compressed at various temperatures and strain rates. (a-c) Deformed at a strain rate of 10^{-2} s^{-1}, (d-f) 10^{-3} s^{-1}, and (g-i) 10^{-4} s^{-1}. (a,d,g) Deformed at 1000°C, (b,e,h) 1100°C, and (c,f,i) 1200°C. Colors in IPFs indicate intensities according to the scale shown in the figure. I_{max} indicates the maximum intensity in each IPF plot.

As was shown in **Figure 2.6**, the stress exponent, *n*, could be estimated from the flow stress analysis. It is known that the strain-rate sensitivity, *m*, has a relationship with *n* as, $m = 1/n$ [3]. Then, the *n* and *m* values obtained at different strains (**Figure 2.6**) are plotted as a function of strain in **Figure 2.15**. Both *n* and *m* showed nearly constant values during the hot-deformation. It is, however, noteworthy that the strain-rate sensitivity (*m*) shows a high value of ~0.35. It has been known that the strain-rate sensitivity (*m*) becomes larger than 0.3 when superplasticity by grain boundary sliding (GBS) occurs [24,25]. The large *m*-value obtained in the present study suggests an occurrence of GBS. It is rather surprising if the heterogeneous necklace microstructures observed in the present material (**Figure 2.9**) dominantly show GBS. However, the fine grain sizes in the necklace regions are preferable for GBS. The occurrence of GBS in the fine-grain regions might explain the continuous softening in the flow curves. The random texture of DRX grains shown in **Figure 2.14** seems to agree with the occurrence of GBS [24]. The possibility of GBS in the DRX necklace structure of HfNbTaTiZr HEA will be discussed more in details in the following **Chapter 3**.

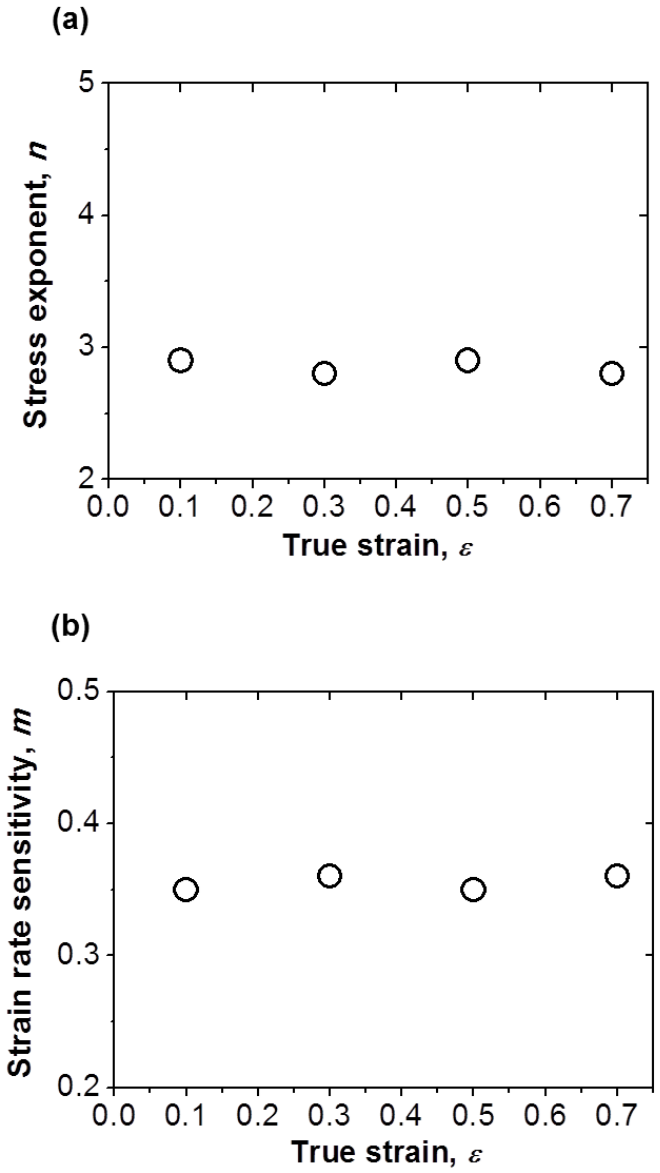

Figure 2.15 (a) Stress exponent, *n*, and (b) Strain-rate sensitivity, *m*, as a function of strain, ε.

2.5. Conclusions

Deformation behavior and microstructural evolution of an equiatomic HfNbTaTiZr HEA was systematically studied by the use of hot-compression test at different temperatures ranging from 1000°C to 1200°C and different strain rates from 10^{-4} s^{-1} to 10^{-2} s^{-1}. Based on the stress-strain behaviors and microstructural observations, the following conclusions were drawn in this chapter:

1 Stress-strain curves for most of the hot-compressed conditions showed sharp drops of the flow stress around yielding followed by continuous flow softening. When the compression at 1000°C was stopped just after the sharp stress-drop and immediately restarted, the stress-drop disappeared. On the other hand, when the specimens were held at 1000°C for 120 s ~ 600 s after quitting the hot-compression, the sharp stress-drop occurred in subsequent re-loading and the degree of the stress drop increased with increasing the holding time. Based on these results, the sharp drop of the flow stress in HfNbTaTiZr was concluded to be attributed to dislocation unlocking by any substitutional solute atom(s) (or any element(s)). In correlation to the continuous flow softening observed after the sharp stress-drop, characteristic necklace microstructures composed of coarse unrecrystallized grains surrounded by fine dynamically recrystallized grains were observed. The occurrence of dynamic recrystallization (DRX) was considered as one of the reasons for the flow softening after the stress drop.

2 Apparent activation energy (Q) for high-temperature deformation of HfNbTaTiZr was evaluated as 124 ~ 113 $kJmol^{-1}$ from the stress-strain data obtained through the hot-compression. The evaluated Q was lower than the activation energies for self-diffusion of the pure elements included in the alloy, but somehow close to the activation energies for self-diffusion in high-temperature β phase (BCC) of Ti and Zr.

3 Depending on the deformation conditions, DRX grain sizes ranged from 0.7 μm to 34 μm. The fine DRX grain sizes suggested sluggish diffusion in the HfNbTaTiZr HEA.

The DRX fraction and DRX grain size were well organized as a function of the flow stress rather than Z calculated by the use of the activation energy of 113 kJmol^{-1}. The DRX fraction and the DRX grain size increased with decreasing the flow stress. In the necklace DRX microstructures, coarse unrecrystallized grains had <001> and <111> fiber textures parallel to the compression axis, which suggested plastic deformation by dislocation slips similar to conventional BCC metals and alloys. On the other hand, the DRX grains did not have textures but rather randomly oriented.

4 The flow stress analysis indicated high strain-rate sensitivity (m) of 0.35 in the hot-compression, which suggested a possibility of grain boundary sliding (GBS) even in the heterogeneous necklace microstructures composed of coarse unrecrystallized regions and fine DRX grains. The fine DRX grains were considered preferable for the occurrence of GBS, and the nearly random texture observed for the DRX grains coincided with GBS.

References

[1] O.N. Senkov, G.B. Wilks, D.B. Miracle, C.P. Chuang, P.K. Liaw, Refractory high-entropy alloys, Intermetallics. 18 (2010) 1758–1765. doi:https://doi.org/10.1016/j.intermet.2010.05.014.

[2] O.N. Senkov, J.K. Jensen, A.L. Pilchak, D.B. Miracle, H.L. Fraser, Compositional variation effects on the microstructure and properties of a refractory high-entropy superalloy AlMo0.5NbTa0.5TiZr, Mater. Des. 139 (2018) 498–511. doi:https://doi.org/10.1016/j.matdes.2017.11.033.

[3] A.H. Chokshi, High temperature deformation in fine grained high entropy alloys, Mater. Chem. Phys. 210 (2018) 152–161. doi:https://doi.org/10.1016/j.matchemphys.2017.07.079.

[4] C.M. Sellars, W.J.M. Tegart, Hot Workability, Int. Metall. Rev. 17 (1972) 1–24. doi:10.1179/imtlr.1972.17.1.1.

[5] H.J. McQueen, N.D. Ryan, Constitutive analysis in hot working, Mater. Sci. Eng. A. 322 (2002) 43–63. doi:https://doi.org/10.1016/S0921-5093(01)01117-0.

[6] O.N. Senkov, J.M. Scott, S. V Senkova, F. Meisenkothen, D.B. Miracle, C.F. Woodward, Microstructure and elevated temperature properties of a refractory TaNbHfZrTi alloy, J. Mater. Sci. 47 (2012) 4062–4074. doi:10.1007/s10853-012-6260-2.

[7] G. Neumann, C. Tuijn, Self-diffusion and Impurity Diffusion in Pure Metals, first ed., Elsevier, Oxford, 2009.

[8] N.L. Peterson, Self-diffusion in pure metals, J. Nucl. Mater. 69–70 (1978) 3–37. doi:https://doi.org/10.1016/0022-3115(78)90234-9.

[9] C. Zener, J.H. Hollomon, Effect of Strain Rate Upon Plastic Flow of Steel, J. Appl. Phys. 15 (1944) 22–32. doi:10.1063/1.1707363.

[10] C.N. Reid, W.S. Owen, Deformation Geometry for Materials Scientists, first ed., Elsevier, 1973.

[11] F.J. Humphreys, M. Hatherly, Chapter 13 - Hot Deformation and Dynamic Restoration, in: F.J. Humphreys, M.B.T.-R. and R.A.P. (Second E. Hatherly (Eds.), Elsevier, Oxford, 2004: p. 415–V. doi:https://doi.org/10.1016/B978-008044164-1/50017-7.

[12] F. Wagner, N. Allain-Bonasso, S. Berbenni, D.P. Field, On the Use of EBSD to Study the Heterogeneity of Plastic Deformation, Mater. Sci. Forum. 702–703 (2012) 245–252. doi:10.4028/www.scientific.net/MSF.702-703.245.

[13] A. Galiyev, R. Kaibyshev, G. Gottstein, Correlation of plastic deformation and dynamic recrystallization in magnesium alloy ZK60, Acta Mater. 49 (2001) 1199–1207. doi:https://doi.org/10.1016/S1359-6454(01)00020-9.

[14] A. Belyakov, H. Miura, T. Sakai, Dynamic recrystallization under warm deformation of a 304 type austenitic stainless steel, Mater. Sci. Eng. A. 255 (1998) 139–147. doi:https://doi.org/10.1016/S0921-5093(98)00784-9.

[15] K.-Y. Tsai, M.-H. Tsai, J.-W. Yeh, Sluggish diffusion in Co–Cr–Fe–Mn–Ni high-entropy alloys, Acta Mater. 61 (2013) 4887–4897. doi:https://doi.org/10.1016/j.actamat.2013.04.058.

[16] G.E. Dieter, Mechanical Metallurgy, third ed., Mc-Graw Hill, 1986.

[17] E.O. Hall, Yield point phenomena in metals and alloys, Plenum Press, New York, 1970.

[18] H. OIKAWA, S. NANBA, Transition of Deformation Behavior of Fe-2.1mol%Mo Alloy in the Power-law Creep Regime, Trans. Iron Steel Inst. Japan. 27 (1987) 402–407. doi:10.2355/isijinternational1966.27.402.

[19] R. Horiuchi, H. Yoshinaga, S. Hama, New Yielding Phenomenon in Some Aluminium Alloys at High Temperatures, Trans. Japan Inst. Met. 6 (1965) 123–130.

doi:10.2320/matertrans1960.6.123.

[20] I. Weiss, S.L. Semiatin, Thermomechanical processing of beta titanium alloys—an overview, Mater. Sci. Eng. A. 243 (1998) 46–65. doi:https://doi.org/10.1016/S0921-5093(97)00783-1.

[21] R.D. Doherty, D.A. Hughes, F.J. Humphreys, J.J. Jonas, D.J. Jensen, M.E. Kassner, W.E. King, T.R. McNelley, H.J. McQueen, A.D. Rollett, Current issues in recrystallization: a review, Mater. Sci. Eng. A. 238 (1997) 219–274. doi:https://doi.org/10.1016/S0921-5093(97)00424-3.

[22] R.R. Eleti, T. Bhattacharjee, L. Zhao, P.P. Bhattacharjee, N. Tsuji, Hot deformation behavior of CoCrFeMnNi FCC high entropy alloy, Mater. Chem. Phys. 210 (2018) 176–186. doi:https://doi.org/10.1016/j.matchemphys.2017.06.062.

[23] N.D. Stepanov, D.G. Shaysultanov, N.Y. Yurchenko, S. V Zherebtsov, A.N. Ladygin, G.A. Salishchev, M.A. Tikhonovsky, High temperature deformation behavior and dynamic recrystallization in CoCrFeNiMn high entropy alloy, Mater. Sci. Eng. A. 636 (2015) 188–195. doi:https://doi.org/10.1016/j.msea.2015.03.097.

[24] K.A. Padmanabhan, G.E. Davies, Superplasticity: Mechanical and Structural Aspects, Environmental Effects, Fundamentals and Applications, Springer, 1980.

[25] O.D. Sherby, J. Wadsworth, Superplasticity—Recent advances and future directions, Prog. Mater. Sci. 33 (1989) 169–221. doi:https://doi.org/10.1016/0079-6425(89)90004-2.

Chapter 3

Dynamic Recrystallization and Related Deformation Mechanisms in Equiatomic HfNbTaTiZr Refractory High Entropy Alloy

3.1. Introduction

Nucleation of new strain-free grains simultaneously during deformation at high temperatures is referred to *Dynamic recrystallization* (DRX). DRX is mostly observed in face-centered cubic (FCC) metals and alloys having low stacking fault energies (low-SFE). As is well known, when the stacking fault energy is low, (a/2)<110> perfect dislocations in FCC tend to dissolve into two Shockley partial dislocations, (a/6)<112> on {111} slip planes. As Shockley partial dislocations generally have mixed nature of screw and edge, cross-slip of dislocations is difficult to happen, so that recovery by the aid of cross-slip of screw dislocations is suppressed in low-SFE FCC metals and alloys. As a result, dislocation density (i.e., the driving force for recrystallization) in such materials greatly increases during deformation, leading to DRX. DRX preferentially occurs along initial grain boundaries (GBs). DRX at GBs is often initiated by the grain boundary bulging process found by Bailey and Hirsch [1]. Although there have been several arguments on the mechanism of bulging process, the most widely accepted assumption is the localized strain induced grain boundary migration [2–4]. As the deformation progresses, developed bulges eventually transform to form equiaxed DRX grains decorating initial GBs. Thus, resulting microstructures are often referred to the necklace-like structure.

In contrast, it is known that dynamic recovery (DRV) is enhanced to occur in BCC metals and alloys and in FCC metals and alloys having high stacking fault energies (like

aluminum and its alloys), so that DRX in those materials are limitedly reported [5]. In BCC metals and alloys, diffusivity of atoms is originally higher owing to their looser packing of atoms than FCC crystals. Additionally, cross-slip of screw dislocations is easy to occur in BCC and high stacking-fault energy FCC metals and alloys, since dislocations are not resolved in planar way. As a result, it is anticipated that the necessary dislocation density (i.e., the driving force for the formation of DRX grains) for the initiation of DRX is difficult to be acquired during hot-working of BCC metals and alloys. Consequently, the initiation of DRX and formation of the characteristic necklace-like structure is suppressed in those materials.

However, as was shown in **Chapter 2**, the HfNbTaTiZr HEA having single phase BCC crystal structure exhibited the characteristic necklace-like DRX structures. Recently, Eleti et al. [6] have reported necklace-like DRX structures in the hot-deformation of CoCrFeMnNi HEA with single phase FCC structure having low-SFE. The experimental evidences of the characteristic necklace-like DRX structure in two kinds of HEAs having different crystal structures might suggest a possibility of sluggish diffusion leading to the suppression of DRV in HEAs regardless of crystal structure. Accordingly, the observations shown in **Chapter 2** widen the possibility to understand the fundamental nature of HEAs having BCC crystal structure. Furthermore, high temperature flow stress analysis of HfNbTaTiZr estimated in **Chapter 2** indicated high strain-rate sensitivity (m), m ~0.35. The estimated m value is obviously higher than the m value generally accepted for grain boundary sliding (GBS) mechanism, i.e., $m > 0.3$. This suggested that the necklace structure composed of fine DRX grains might show GBS mechanism. Therefore, the primary objective of the present chapter is to investigate the evolution of necklace DRX structure and related deformation mechanisms in the HfNbTaTiZr alloy having BCC crystal structure during high temperature deformation.

3.2. Experimental Procedures

3.2.1. High-Temperature Compression Tests

In **Chapter 2**, microstructural evolution was investigated at wide ranges of deformation temperatures ranging from 1000°C to 1200°C and different strain rates from 10^{-4} s^{-1} to 10^{-2} s^{-1}. The typical DRX necklace structure was observed for various deformation conditions was shown in **Chapter 2, Figure 2.9 (a-e, g)**. It is noteworthy furthermore that the necklace structures in those deformation conditions showed ultrafine and near-ultrafine DRX grains (d ~ 0.7 – 3.4 μm). Considering the observed DRX grain sizes and DRX fractions at various temperatures and different strain rates, the specimen deformed at 1000°C and 10^{-3} s^{-1} showed necklace structure composed of ultrafine DRX grains, d ~1.5 μm and moderate DRX fraction, f_{DRX} ~17%. Therefore, in the present chapter, the deformation temperature 1000°C for the strain rate 10^{-3} s^{-1} was selected to understand the evolution of DRX and related deformation mechanisms in the HfNbTaTiZr HEA.

The as-cast HfNbTaTiZr equiatomic BCC HEA was used in this study. Details of the starting as-cast material are already shown in **Chapter 2**. The initial as-cast structure consisted of coarse equiaxed grains with grain sizes of 140~400 μm. Selection of the coarse-grained specimens for hot-deformation tests makes it easy to distinguish the evolution of microstructures in grain boundary regions and at grain interiors. Cylindrical specimens having dimensions 8 mm in diameter and 12 mm in height were cut from the as-cast material by the use of an electric discharge wire-cutting machine. Uniaxial compression tests were carried out in a thermo-mechanical processing simulator (model: Thermecmastor-Z, Fuji Electronic Industrial Company Ltd.). **Figure 3.1** schematically illustrates the thermo-mechanical processing pattern tested in the present chapter. The specimens were heated from room temperature to a set deformation temperature at a heating rate of 10°C s^{-1} by an induction heating system equipped in the physical simulator and held isothermally for 900 seconds before compression, in order to homogenize temperature of the specimens. For precise temperature control and measurement, a

thermocouple was welded at mid-height positions on side surfaces of the cylindrical specimens. Mica plates and glass powder were used as insulator and lubricant in the compression, respectively. Uniaxial compression was carried out at the deformation temperature 1000°C for the strain rate 10^{-3} s^{-1} in a vacuum atmosphere. The compression tests were carried out to different true strains, i.e., $\varepsilon \sim 0.06$, 0.08, 0.1, 0.3, 0.5, and 0.69. The specimens were water quenched immediately after the compression and provided for microstructural observations.

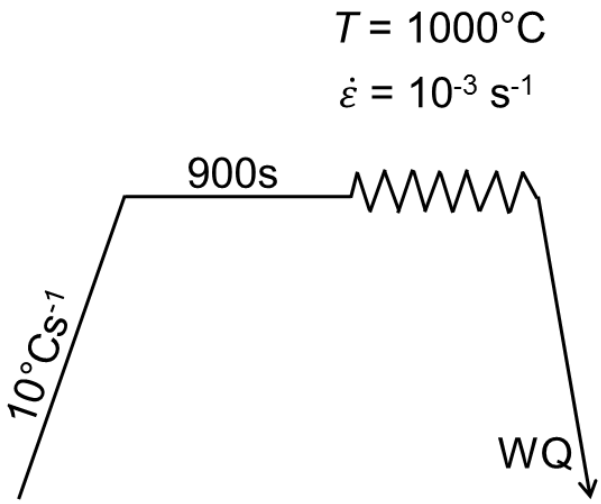

Figure 3.1 Schematic diagram showing the thermo-mechanical process and processing conditions in the hot-compression tests.

3.3. Results

3.3.1. Stress-Strain Curve and Flow Behavior

Figure 3.2 shows the compressive stress-strain curve of the HfNbTaTiZr RHEA at 1000°C and a strain rate of 10^{-3} s^{-1}. The stress-strain curve showed a distinctive sharp drop in the flow stress around yielding, followed by a continuous decrease in the flow stress. The

flow behaviors associated with the microstructural aspects are discussed in the later part of this chapter.

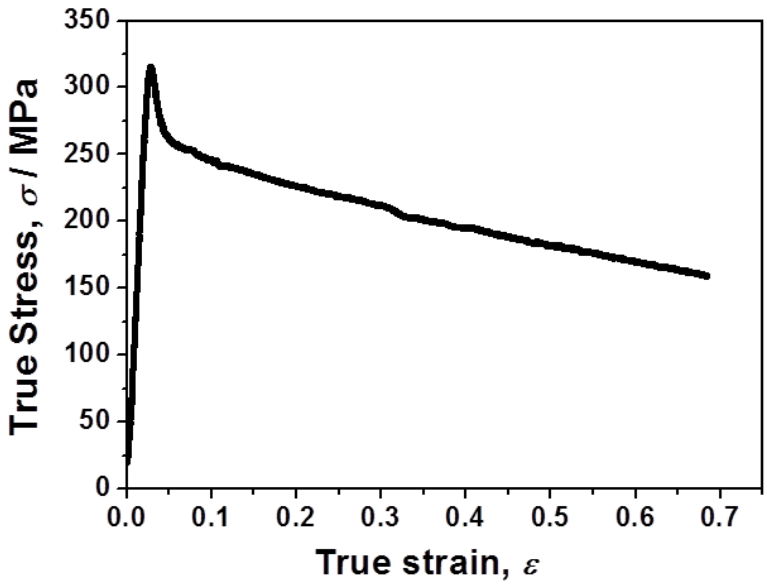

Figure 3.2 Compressive stress-strain curve of the equiatomic HfNbTaTiZr refractory high entropy alloy hot-compressed at 1000°C and a strain rate of 10^{-3} s^{-1}. Compressed to 50% reduction in height, corresponding to an equivalent true strain of ε ~0.69.

3.3.2. Evolution of Microstructure and Texture

Microstructural changes in the HfNbTaTiZr HEA during high-temperature deformation to different true strains ranging from ε ~0.06 to 0.69 are shown in **Figure 3.3**. The microstructures shown in **Figure 3.3** are EBSD inverse pole figure (IPF) maps where colors indicate crystallographic orientations parallel to the compression axis (C.A.), according to the key stereographic triangle inserted. High magnification images corresponding to the microstructures shown in **Figure 3.3** are shown in **Figure 3.4**. Microstructures indicated an evolution of fine, equiaxed grains along initial grain boundaries. The observed fine, equiaxed grains resembled the characteristic necklace-like structure often observed in dynamically recrystallized (DRX) metals and alloys occurring

during hot-deformation. At the same time, unrecrystallized deformed matrix surrounded by the DRX necklace structures was also observed (**Figure 3.3**). Initial deformed grains surrounded by the necklace structures were elongated to directions perpendicular to C.A.

The evolution of microstructure at early stages of deformation was characterized by serrations, and significant bulging of initial grain boundaries (**Figure 3.4 (a-c)**). With increasing the deformation strain ($\varepsilon \geq 0.1$), grain boundary bulging led to the formation of necklace structure of DRX grains (**Figure 3.4 (d-f)**). The evolution of equiaxed DRX grains resulted from grain boundary bulging is one of the typical processes for the formation of necklace structure [1]. It should be noted that DRX grains in the necklace structure obtained for the present deformation condition at 1000C and 10^{-3} s^{-1} showed ultra-fine grain sizes ($d \leq 1.5$ μm). The volume fraction of DRX grains was quantified by separating DRX grains from overall microstructures of EBSD analysis. Grain orientation spread (GOS) approach was used to identify DRX grains, which was already discussed in **Chapter 2**. Grains satisfying GOS $\leq 2°$ were considered as DRX grains. The volume fraction of DRX grains (f_{DRX}, %) increased with increasing the deformation strain, as shown in **Figure 3.5 a**. EBSD scan data were obtained in multiple locations to determine the average DRX grain size (d_{DRX}, μm). The average DRX grain size was measured using the line intercept method. The increase of deformation strain scarcely affected the DRX grain size, as shown in **Figure 3.5 b**. The DRX grains size stability of the HfNbTaTiZr HEA during high temperature deformation is explained in the later part of this chapter concerning the high temperature deformation mechanisms. Here it is worth noting that the present alloy has the single phase BCC structure. As was already mentioned in the introduction section, the possibility of DRX is suppressed in BCC materials due to their enhanced DRV. However, the present results showed the characteristic DRX necklace structure and inhibited grain growth during the progress of deformation. In the context of above results, it can be concluded that the hot-deformation behaviors of HfNbTaTiZr BCC-HEA might be related to suppressed DRV in HEAs [7].

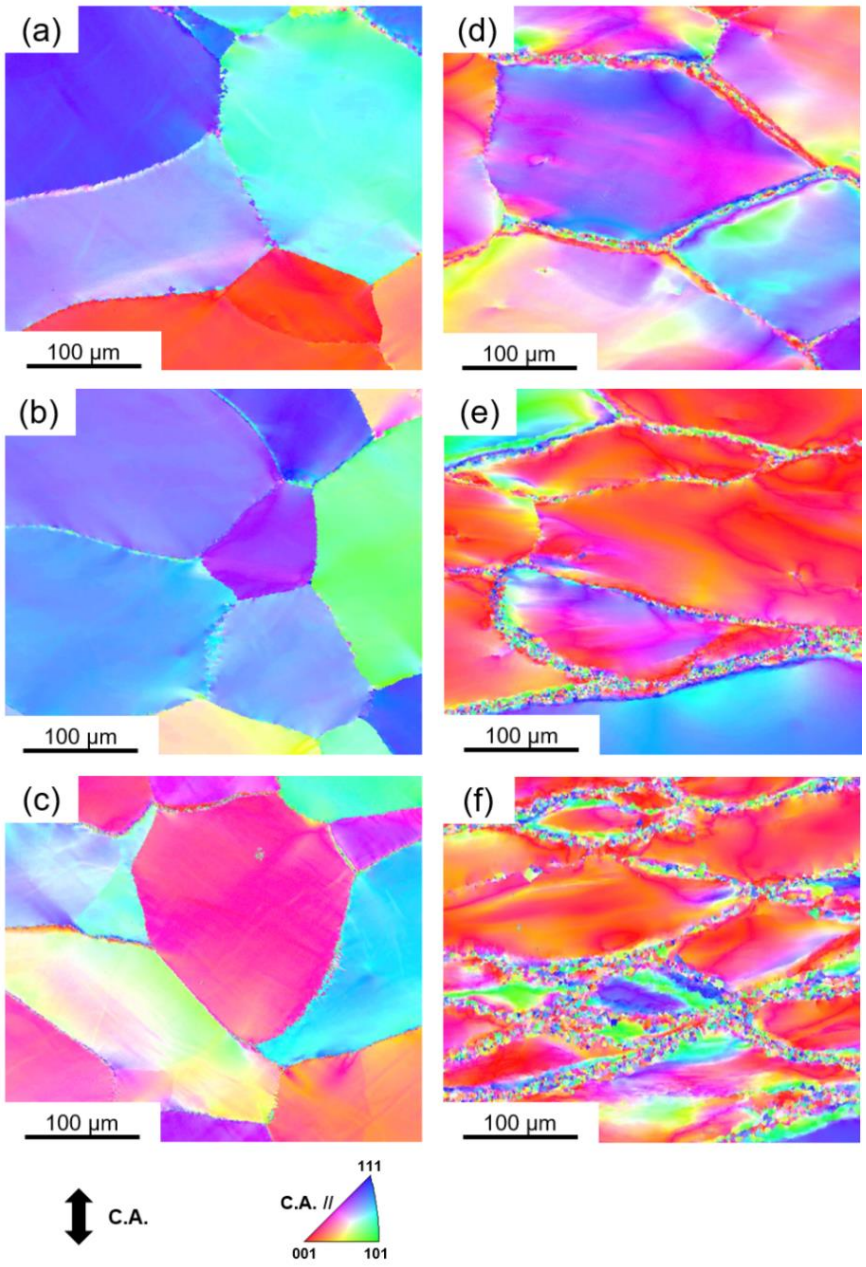

Figure 3.3 EBSD inverse pole figure (IPF) maps of the specimens hot-compressed to different strains at 1000°C and 10^{-3} s^{-1}, showing the evolution of dynamic recrystallization (DRX): (a) ε ~0.06, (b) ε ~0.08, (c) ε ~0.1, (d) ε ~0.3, (e) ε ~0.5, (f) ε ~0.69.

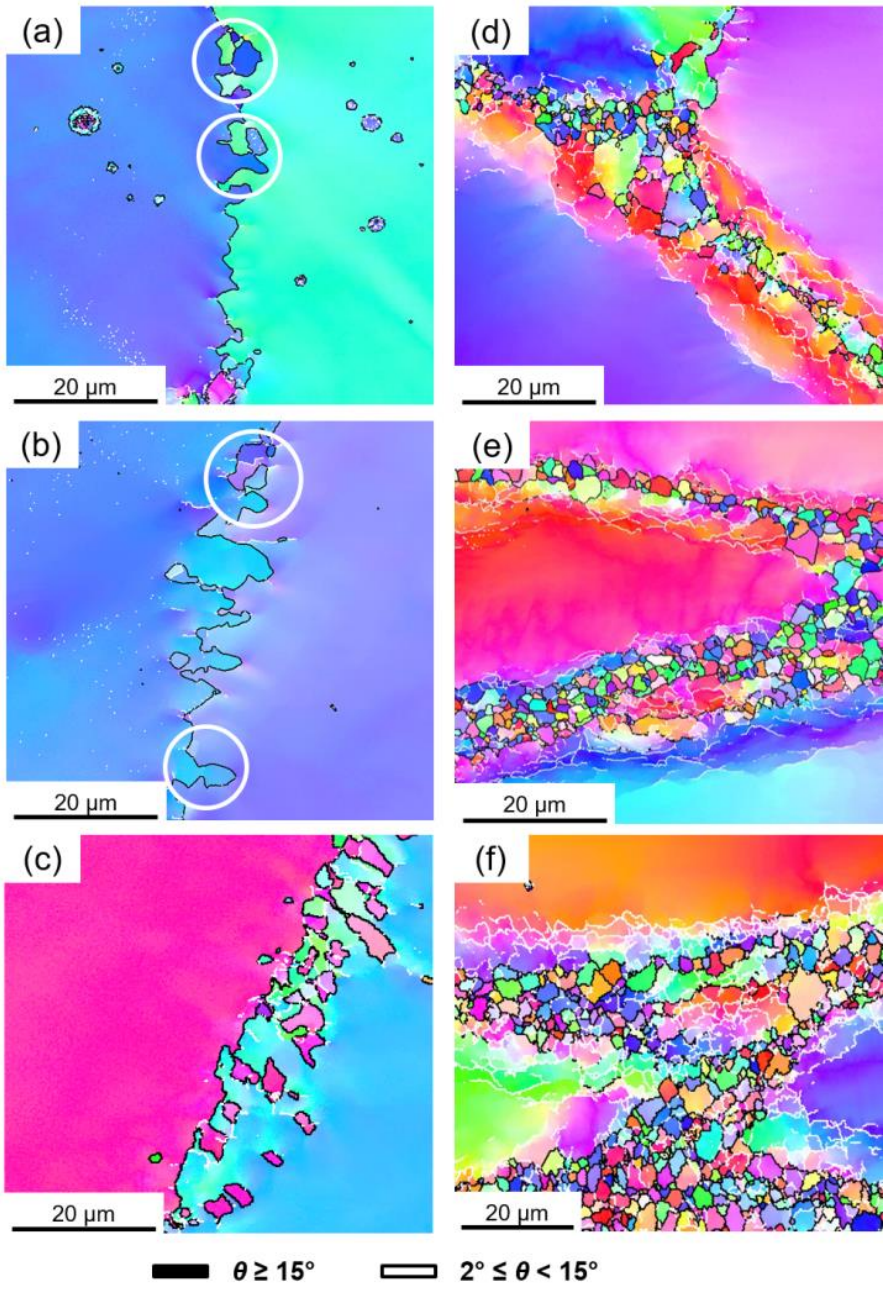

Figure 3.4 High magnification EBSD-IPF maps of the HfNbTaTiZr specimens hot-compressed to different strains at 1000°C and 10^{-3} s^{-1}, corresponding to the microstructures shown in **Figure 3.3**. (a) ε ~0.06, (b) ε ~0.08, (c) ε ~0.1, (d) ε ~0.3, (e) ε ~0.5, (f) ε ~0.69.

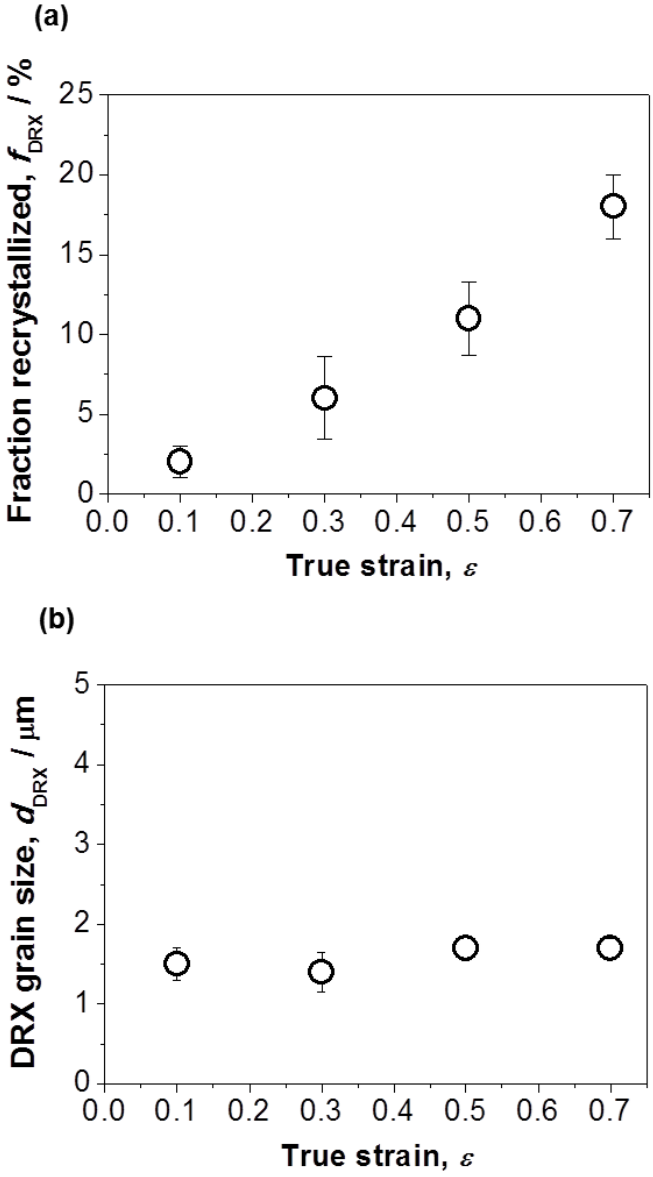

Figure 3.5 (a) Fraction recrystallized (f_{DRX}) and (b) DRX grain size (d_{DRX}) in the specimens hot-compressed to different strains at 1000°C and 10^{-3} s^{-1}. Plotted as a function of true compression strain, ε.

Some portions of grain boundary bulging and the newly formed DRX grains had similar orientations to those of the parent grains, as shown in circles of **Figure 3.4 (a,b)**. Here, the specimen hot-compressed to ε ~0.1 is selected as a typical example to explain this point. As shown in **Figure 3.6**, the newly formed DRX grains showed red colors, i.e., <001> orientation parallel to C.A. The observed orientation was identical to the orientation of the parent grain. To evaluate the orientation relationship between the deformed matrix and the DRX necklace structure furthermore, large area EBSD scans were performed for the specimens deformed to different strains, ε ~0.3, 0.5, and 0.69, at 1000°C and 10^{-3} s^{-1}. The specimens showed notable DRX fractions. Microstructures and the corresponding texture for the deformed and DRX grains are shown in **Figure 3.7**. It is interesting to note that the coarse unrecrystallized grains preferentially showed <001> and/or <111> orientations parallel to C.A. The <001> and <111> orientations parallel to C.A. are known as the typical deformation texture of BCC metals and alloys deformed in compression [8]. On the other hand, DRX grains in the specimens deformed to different strains of ε ~0.3, 0.5, and 0.69 showed no preferred orientations. Thus, it can be concluded that the orientation of the newly formed fine DRX grains at ε ~0.1, which were developed from bulging of initial grain boundaries had the same orientation as that of the parent grain, but showed rather random texture with the progress of DRX. The loss of preferred orientations of the DRX grains will be discussed in the later part of this chapter by considering the deformation mechanisms in the necklace structure composed of fine, equiaxed DRX grains.

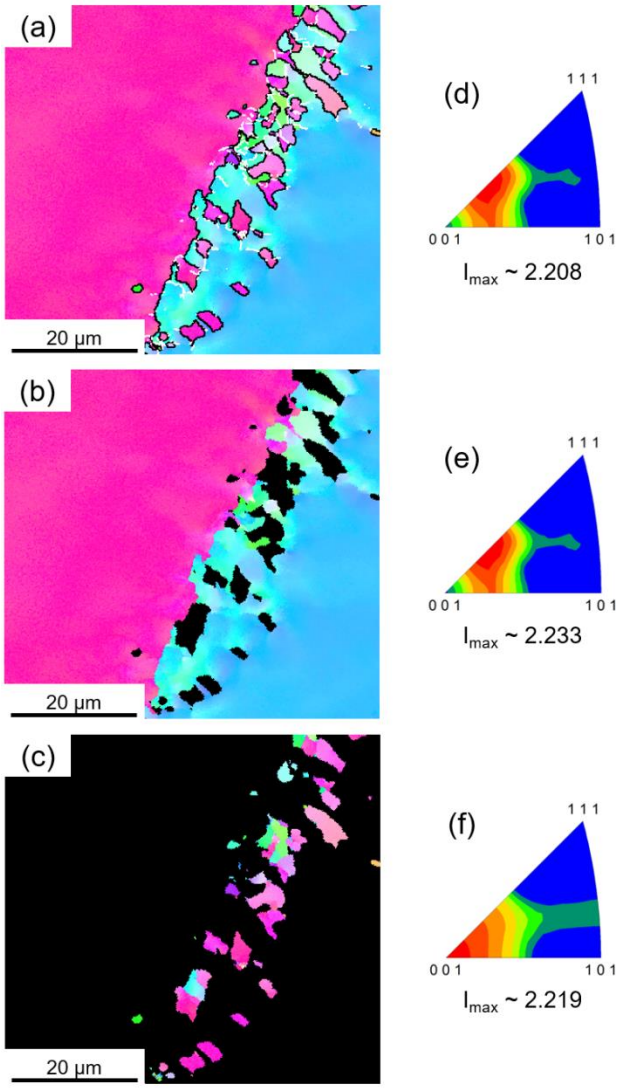

Figure 3.6 EBSD IPF maps and the corresponding IPF plots of the specimen hot-compressed to ε ~0.1 at 1000°C and 10^{-3} s^{-1}, showing orientation relationships between the parent grain and the newly formed DRX grains. (a,d) IPF map of overall microstructure and corresponding inverse pole figure showing orientations parallel to CA. (b,e) IPF map of deformed (unrecrystallized) parent grains (*GOS* > *2*°) and corresponding inverse pole figure. (c,f) IPF map of DRX grains (*GOS* ≤ *2*°) and corresponding inverse pole figure.

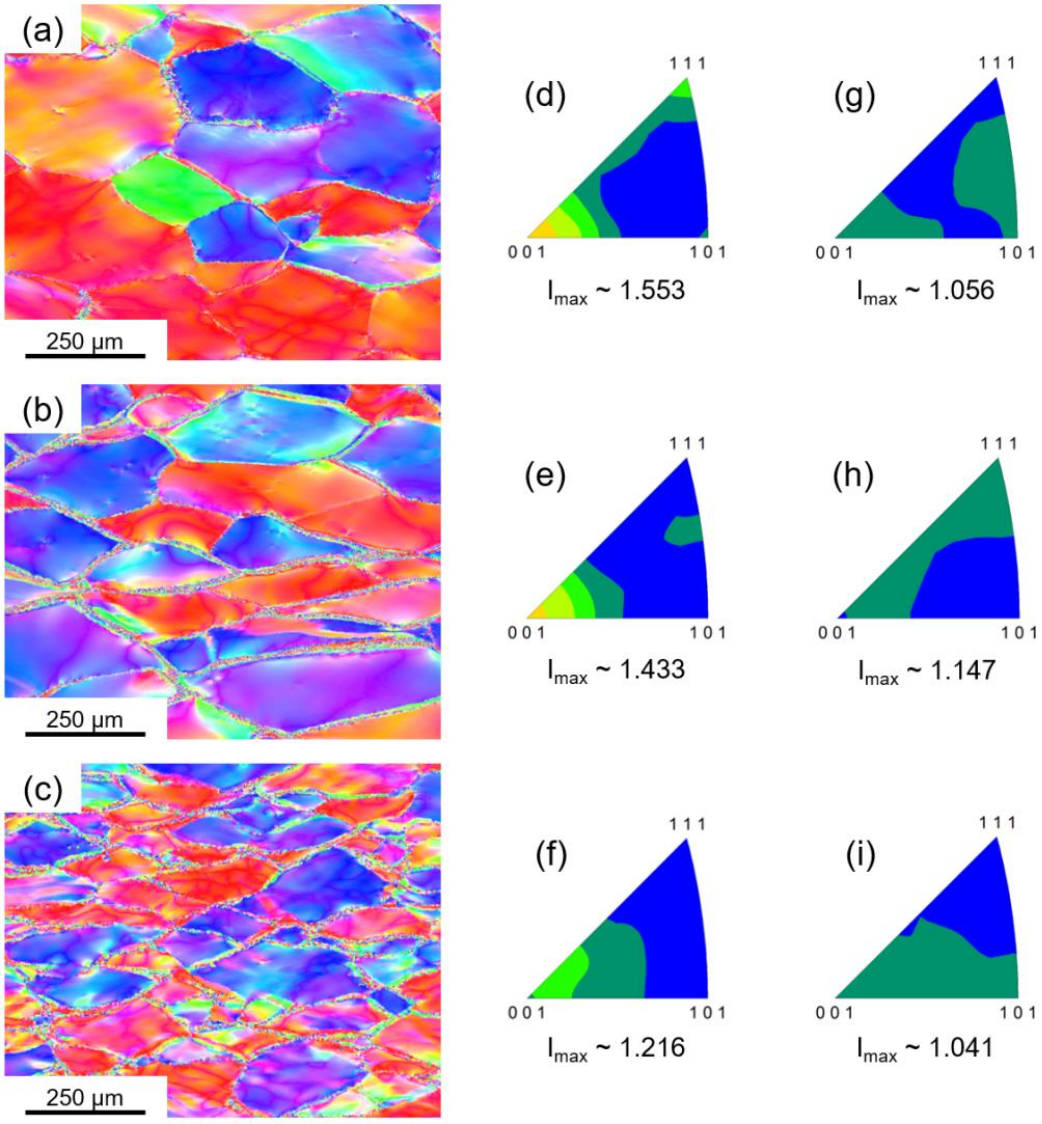

Figure 3.7 (a-c) EBSD IPF maps showing crystallographic orientations parallel to the compression axis (C.A.) for the specimens deformed to ε ~0.3, ε ~0.5, and ε ~0.69 respectively, at 1000°C and 10^{-3} s^{-1}. (d-f) Inverse pole figures showing orientations parallel to CA of the unrecrystallized regions (*GOS* > *2*°), and (g-i) the recrystallized regions (*GOS* ≤ *2*°).

3.4. Discussion

3.4.1. Evolution of DRX Necklace Structure

Evolution of microstructure during hot-deformation of HfNbTaTiZr HEA was characterized by the formation of necklace-like DRX structure. For initiating DRX (recrystallization during deformation at elevated temperatures), enough stored energy (i.e., high density of dislocations) is necessary. Dislocations are most likely stored near initial grain boundaries, deformation bands, and interfaces with second phases in microstructures. In such heterogeneously deformed sites, not only highly stored dislocations but also large local misorientations may develop. As a result, DRX grains are often initiated along initial grain boundaries to form necklace-like structures. In that sense, the DRX microstructure observed in the present hot-deformed HfNbTaTiZr HEA is a typical and possible structure. However, materials deformed at elevated temperatures often cannot store sufficient energy to induce recrystallization, due to the simultaneously occurring dislocation annihilation process which is called dynamic recovery (DRV) [5].

It should be noted that the present alloy has a single phase body-centered cubic (BCC) structure. The notable grain boundary bulging and typical necklace structures of DRX grains observed in the present HfNbTaTiZr alloy are uncommon in BCC metals and alloys. BCC metals and alloys undergo enhanced DRV during deformation at high-temperatures. The enhanced DRV in BCC metals and alloys is primarily attributed to the enhanced diffusion in the BCC structure having looser packing of atoms than close-packed face-centered cubic (FCC) metals and alloys. Additionally, the enhanced DRV in BCC is also due to the cross slip of screw dislocations, since different from FCC metals and alloys having medium to low stacking fault energies of {111} plane dislocations in BCC crystal do not dissolve into partial dislocations in planar manner (like Shockley partial in FCC). As a result, dislocations introduced in plastic deformation are quickly annihilated especially at elevated temperatures, leading to the inhibition of recrystallization (DRX). Despite such typical tendencies in conventional BCC metals and alloys, the present HfNbTaTiZr BCC alloy showed the characteristic grain boundary bulging and typical DRX necklace structure,

as was shown in **Figure 3.4 a-c**. Grain boundary bulging similar to the present one was reported in an ordered Ni_3Al intermetallic compound [2], pure Cu [9], and CoCrFeMnNi FCC-HEA [10].

The complicated shapes of grain boundary bulging would lead to localized and heterogeneous deformation near the corner of the jigsaw-shaped grain boundaries [1,2,4]. Such a local deformation can introduce excess dislocations and local misorientations that assist the transformation of bulge portions into equiaxed regions surrounded by high-angle grain boundaries, i.e., DRX grains along initial grain boundaries. This is thought to be the formation process of the necklace structures of the DRX grains. It is noteworthy furthermore that the necklace structures composed of ultrafine and near-ultrafine DRX grains (d ~ 0.7 – 3.4 μm) formed under wide range of deformation conditions in the present HfNbTaTiZr alloy (**Chapter 2, Figure 2.9 (a-e, g)**). It should be enhanced again that diffusion in BCC is faster than close-packed FCC (or HCP), so that grain growth in BCC metals and alloys is usually quick. For example, in Ti and its alloys which have BCC β phase at high temperature, significant grain growth of β happens to result in very coarse grain structures with sizes over several hundred micrometers [11]. The stable DRX grain size observed in the present BCC-HEA indicates an inhibition of grain growth, which is explained in the next paragraph.

The onset of DRX induces heterogeneous microstructures (necklace structures) composed of strain-hardened initial grains surrounded by fine DRX grains with low dislocation densities. Therefore, the DRX necklace region is considered softer than the unrecrystallized region inside. Here, it is noteworthy that the softer necklace regions were composed of ultrafine grain size of d ~1.5μm under the present deformation condition, at 1000°C and 10^{-3} s^{-1}. The fine grain size may change the deformation mechanism at elevated temperatures. It is noteworthy furthermore, the present HfNbTaTiZr HEA showed high strain rate sensitivity, m > 0.35 (refer to **Chapter 2**) indicating the possibility of grain boundary sliding (GBS) mechanism.

In order to verify the possibility of GBS, compression test was carried out using the as-cast specimens having a rectangular prismatic shape of $6 \times 6 \times 9$ mm^3, for making it possible to observe flat surfaces before and after deformation. The specimen was initially deformed at 1000°C to a true strain ε ~0.3 at a strain rate 10^{-3} s^{-1} along the thermo-mechanical procedure shown in **Figure 3.1**, in order to introduce a necklace DRX structure. After the first step of deformation to ε ~0.3, all side-surfaces of the specimen were carefully polished to realize flat surfaces. One of the facets of the sample was electropolished for subsequent observations. Marker grids having dimentions 50 µm (length) × 40 µm (height) × 0.3 µm (depth) were drawn in DRX regions using focused ion beam (FIB) (Model: FEI Quanta 3D 200i). Each marker line on the grid was separated by ~ 5µm apart. Then, the specimen was furthermore deformed (re-compressed) to a total strain of ε ~0.45 (additional strain after the first step, ε ~0.15) and cooled by Ar gas to room temperature. **Figure 3.8** shows the SEM-BSE images of the marker grids in the DRX regions before and after re-compression. The re-compressed specimen clearly showed shear offsets of the marker grids at grain boundaries of DRX grains. The result is a direct evidence for the occurrence of GBS in the equiatomic HfNbTaTiZr HEA. Here, it could be noted that GBS is a relative motion of grains by simple shear parallel to the grain boundary which can subject grains to rotate. As a result, grains deforming by GBS often remain equiaxed and shows inhibited grain growth. Therefore, it could be concluded that the high temperature DRX grains size stabiliy of HfNbTaTiZr could be due to the possibility of GBS mechanism. It should be noted that the specimen did not have a fully fine grained structure but a heterogeneous necklace microstructure composed of unrecrystallized coarse grains (core regions) and surrounding fine DRX grains (necklace regions). GBS in such heterogeneous microstructures cannot be found in previous literature.

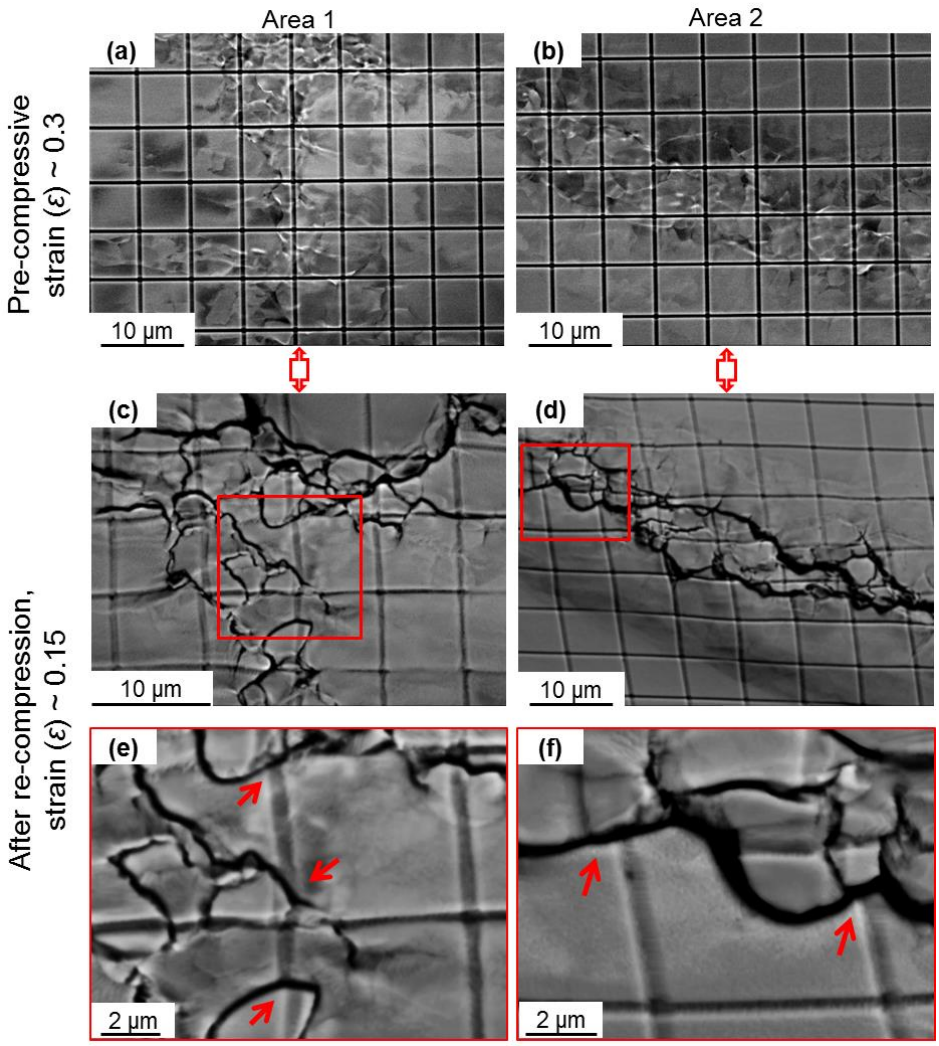

Figure 3.8 SEM-BSE images of the specimen hot-compressed at 1000°C and a strain rate of 10^{-3} s^{-1}. (a,b) FIB marker grids near DRX necklace regions (area 1 and area 2) in the specimen pre-compressed to a strain of ε ~0.3. (c and d) Identical areas of (a) and (b), respectively, after the second step of hot compression to a total strain of ε ~0.45(additional strain after the first step, ε ~0.15), showing offsets of the marker lines. (e,f) High magnification images of the regions surrounde by red rectangles in (c,d), where shear offsets of the marker lines at grain boundaries of fine DRX grains are pointed by red arrows. The C.A. direction is parallel to the vertical direction of the microstructures.

3.4.2. Influence of GBS on Microstructure Evolution

The microstructure evolution was carefully studied in the former sections, and the occurrence of GBS along the necklace regions of ultrafine DRX grains was confirmed. Here, the influence of the occurrence of GBS on the evolution of microstructure is discussed. **Figure 3.9** shows large area EBSD scans for the specimens deformed to different strains, ε ~0.3, 0.5, and 0.69, at 1000°C and 10^{-3} s^{-1}, under which notable DRX fractions were obtained. Microstructural observations showed development of mesoscopic bands. The bands are highlighted by yellow broken lines. In the present case, a band is composed of ultrafine DRX grains. As shown in **Figure 3.9 a**, at the deformation strain ε ~0.3, two grains, denoted as G1 and G2 are connected by band shown by the yellow broken lines. **Figure 3.9 b** shows that the number of grains connected by the band increased with the increase of deformation strain ε ~0.5. At the strain ε ~0.69, several interconnected bands developed diamond-shaped grain morphology, shown in **Figure 3.9 c.** It is also noteworthy that regions of intense low angle grain boundaries (LAGBs) with misorientations (θ), $2° \leq \theta < 15°$, were observed on both sides of necklace regions composed of DRX grains. It is worth mentioning furthermore, on the same microstructures unconventional grain boundary junctions were observed. **Figure 3.10** shows the microstructural characteristics such as 'Y'-type junctions, 'T'-type junctions, and 'X'-type junctions highlighted as circle, triangle, and diamond symbols in yellow color respectively. Moreover, it was apparent that the 'Y'-type junctions decreased, whereas 'T'-type and 'X'-type junctions increased with the increase of deformation strain.

Development of the bands along grain boundaries similar to the present case was reported in a superplastically deformed Zn-22%Al alloy [12]. The development of such bands was primarily considered due to migration of triple junctions (TJs). Basically, GBS is a simple shear deformation along grain boundaries. However, grain boundaries are not perfectly flat surfaces but generally have curvature composed of steps and ledges in an atomistic scale. Furthermore, there must be discontinuities at grain boundary triple

junctions (exactly speaking, triple junction lines). Thus, GBS must be accommodated by additional processes to avoid nucleation of voids or duplication of mass at such regions.

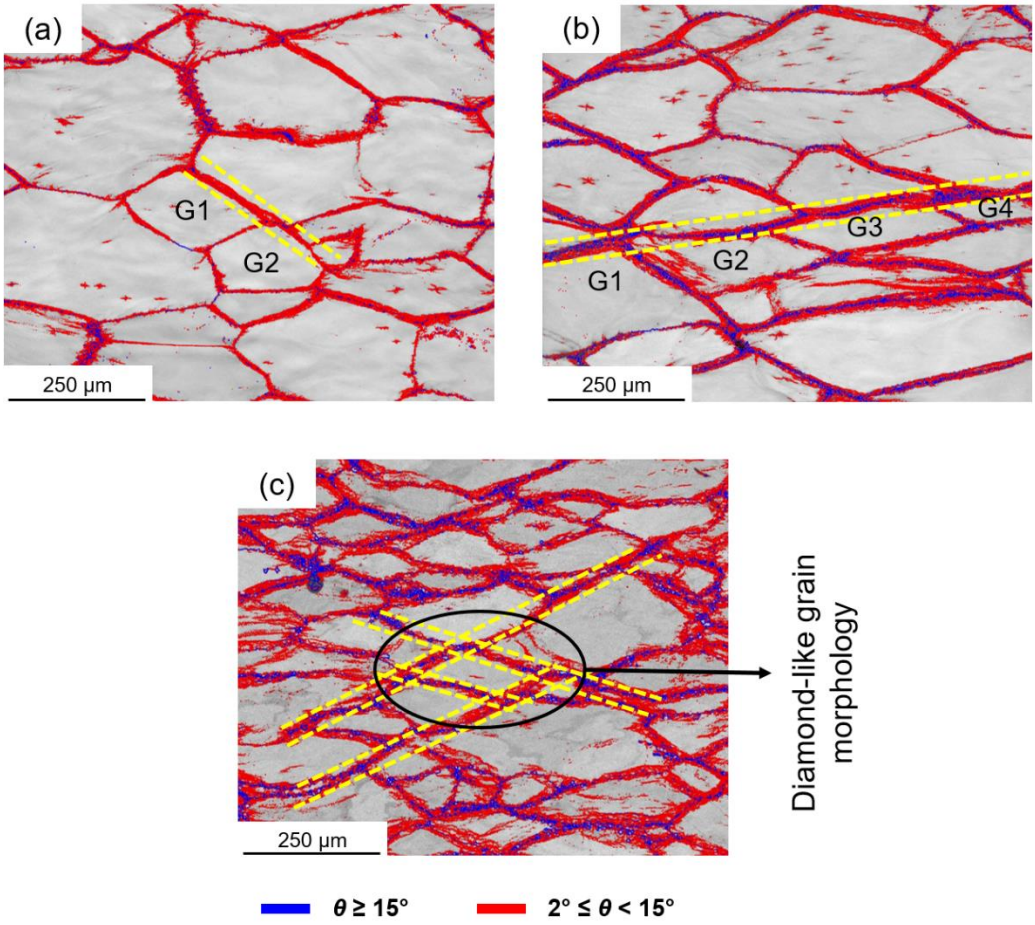

Figure 3.9 EBSD grain boundary and image quality (IQ) maps of the specimens hot-compressed at 1000°C for the strain rate 10^{-3} s^{-1} for different strain intervals showing mesoscopic bands and the developed diamond-like grain morphology shown in yellow broken lines; (a-c) for strain intervals ε ~0.3, ε ~0.5, and ε ~0.69 respectively. Low angle grain boundaries with misorientations (θ), $2° \leq \theta < 15°$ and high angle grain boundaries with $\theta \geq 15°$ are shown in red and blue lines, respectively. The C.A. direction is parallel to the vertical direction of the microstructures.

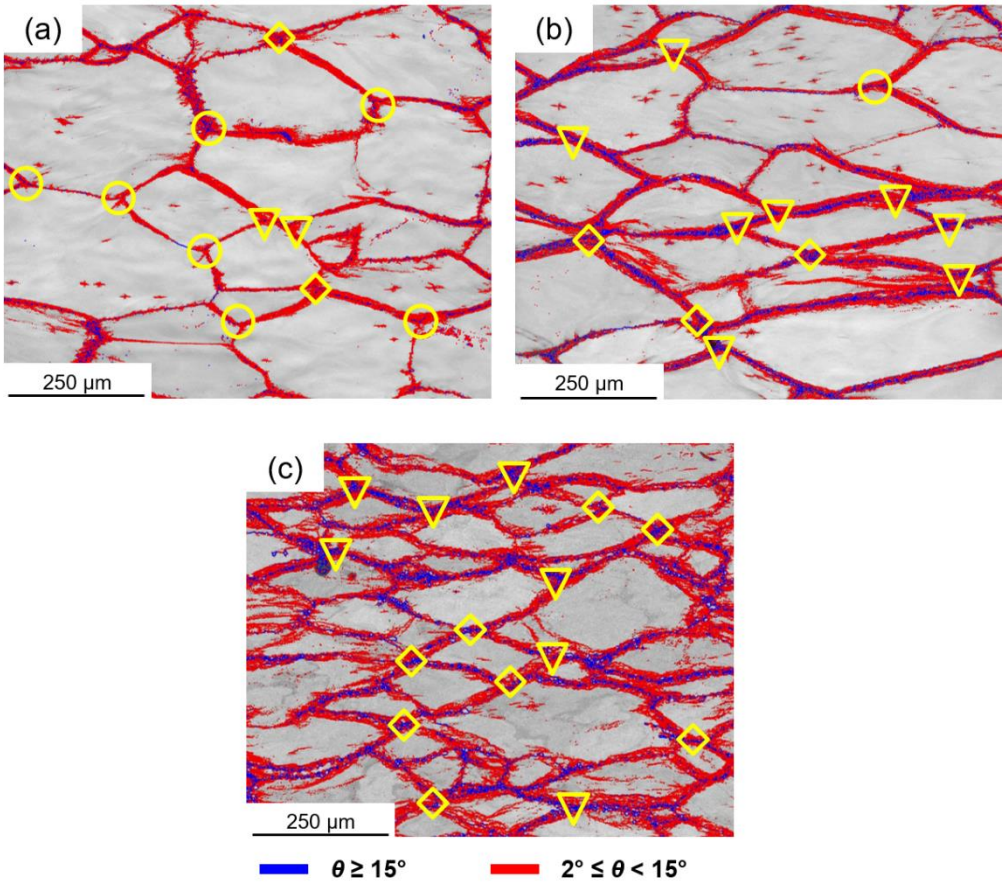

Figure 3.10 EBSD grain boundary and image quality (IQ) maps of the specimens hot-compressed at 1000°C for the strain rate 10^{-3} s^{-1} for different strain intervals showing 'Y'-type, 'T'-type, and 'X'-type junctions shown in yellow circle, triangle, and diamond shapes respectively; (a-c) for strain intervals ε ~0.3, ε ~0.5, and ε ~0.69 respectively. Low angle grain boundaries with misorientations (θ), $2° \leq \theta < 15°$ and high angle grain boundaries with $\theta \geq 15°$ are shown in red and blue lines, respectively. The C.A. direction is parallel to the vertical direction of the microstructures.

TJ migration obviously requires mass transport across the boundary. A large number of different investigators have suggested several possibilities of mass transfer [13–16]. Ashby and Verrel [17], Raj and Ashby [18] suggested that GBS obstructed at TJs could be understood in terms of accommodation by diffusion. Obstructed GBS at the TJ results in the stress concentration which might lead to generation of excess dislocations. The availability of excess defects in the adjacent region of TJ can enhance the rate of diffusion, thus TJ migration could be realized. In addition, Astanin et al. [19] investigated GBS in the Al tri-crystals. They found that straightening of TJ takes place by the TJ migration. The same process might hold true for the present study in terms of considering microstructural similarities. **Figure 3.11** shows a schematic illustration concerning the possibility of TJ migration and its assistance in the transition of 'Y'-type junction to 'T'-type or 'X'-type junction. It is worth emphasizing that the initial GBs in the present deformation condition were replaced by the DRX necklace structure. As TJs were already occupied by DRX grains which are susceptible to GBS mechanism, perhaps TJs might assist the deformation by local migration which leads to the transition of 'Y'-type junction to 'T'-type junction that resemble as a mesoscopic band as experimentally observed. It could be suggested that the frequent occurrence of such TJ migration can lead to the formation of 'X'-type junction that the microstructure eventually resemble as diamond grain morphology as was observed.

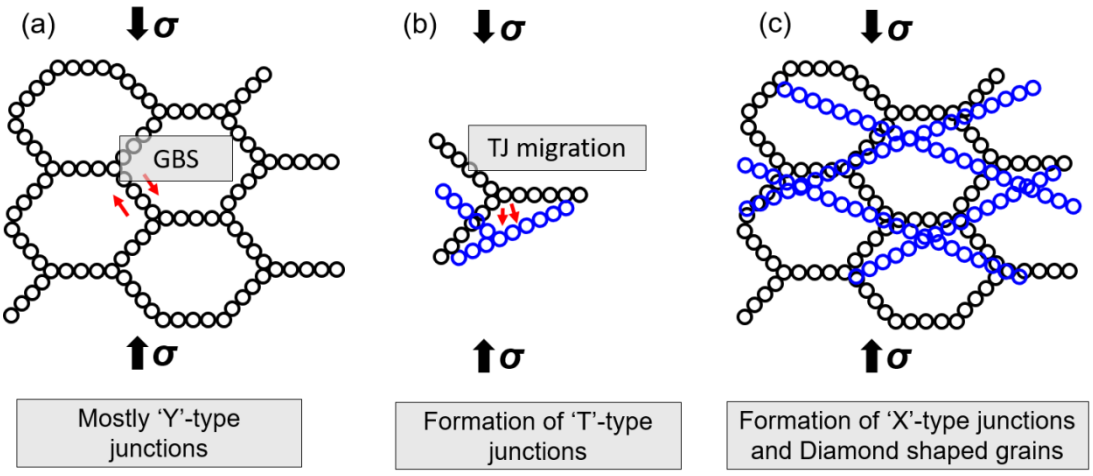

Figure 3.11 (a) A schematic illustration showing the characteristic DRX necklace structure with a possibility of grain boundary sliding (GBS) mechanism, where the microstructure is mostly composed of 'Y'-type junctions. (b) A schematic illustration showing straightening of triple junction (TJ) by TJ migration and resulting in the transition of 'Y'-type junctions to 'T'-type junction, (c) A schematic illustration showing several interconnected bands formed due to frequent TJ migration develop diamond shaped grains, and 'X'-type junctions.

On the other hand, as is well known, GBS induce sufficiently high lattice bending in the adjacent region of the grain boundary. It has been assumed that lattice bending is often accommodated by generation of excess dislocations. At high temperature, as dislocations can undergo climb, it might be expected that high degree of polygonization (development of LAGBs) would be induced just along the narrow region of grain boundary as is experimentally observed. Dorn [13] reported identical behavior in polycrystalline Al during the occurrence of GBS as the dominant deformation mechanism.

All of the above mentioned experimental evidences strongly suggested GBS might be the dominant deformation mechanism in the HfNbTaTiZr HEA during high-temperature

compression deformation. The present results showed that the heterogeneous microstructure composed of coarse unrecrystallized grains surrounded by DRX necklace structure can also undergo typical GBS mechanism.

3.4.3. Evolution of Texture

Unrecrystallized initial grains in **Figure 3.7** showed the <001> and/or <111> fiber texture, which is known as a typical compression texture in BCC metals and alloys. The texture indicates the occurrence of normal dislocation slips, like {110}<111>, {112}<111>, and {123}<111> in the unrecrystallized grains [8]. On the other hand, the pole intensity (I_{max}) of <001>/<111> orientation decreased with the increase of strain, as shown in **Figure 3.12**. The pole intensity indicates the relative strength of texture with regards to random orientation distribution, so that the pole intensity of '1' corresponds to completely random texture. Zhao et al. [20] showed the evolution of deformation texture during the occurrence of GBS in Pd-Au alloy. The pole intensity of the stable <110> was reported to have decreased with the increased contribution of GBS to the total deformation. Grains are expected to undergo random rotation during the occurrence of GBS. As a result, GBS often randomizes texture. In the present study, it was showed that the HfNbTaTiZr deform by GBS mechanism. Perhaps the influence of GBS mechanism could be taken into account for the decreased pole intensity. On the other hand, as is shown in **Figure 3.6**, freshly formed DRX grains had preferred orientation to the parent grain. The progress of deformation rapidly randomized DRX texture, shown in **Figure 3.7**. Ponge and Gottstein [2] reported similar observations for the high-temperature compression deformation of Ni_3Al an ordered intermetallic compound. Texture randomization of the DRX grains was correlated to the possibility of GBS along the DRX grains in the Ni_3Al due to observed high strain-rate sensitivity m ~0.4 to 0.5. In the present study, considering the direct evidence for GBS, the occurrence of random rotations of DRX grains due to GBS could have randomized the DRX texture.

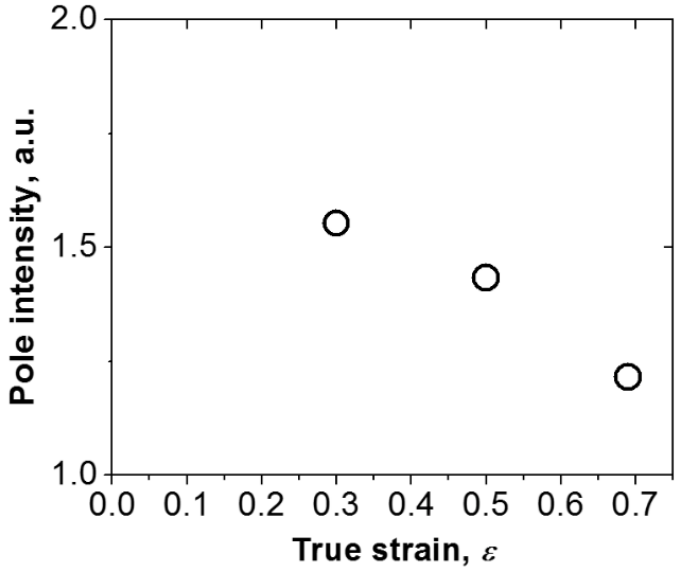

Figure 3.12 Effect of increased deformation strain on the pole intensity of deformed/unrecrystallized grains (*GOS > 2°*).

3.4.4. Correlation between Microstructural Aspects and the Flow Softening

The stress-strain behavior of HfNbTaTiZr during high temperature deformation showed a sharp drop in the flow stress around yielding, followed by a continuous decrease of the flow stress (**Figure 3.2**). The related mechanism for the high-temperature sharp drop of the flow stress was already discussed in **Chapter 2**. Here, the continuous decrease in the flow stress (gradual softening) after the stress drop is discussed, correlating with the microstructure evolution observed. Dynamic recrystallization (DRX) is one of the softening processes that simultaneously occur during deformation at elevated temperatures. In the present study, DRX grains formed along initial grain boundaries and resultant necklace structures were confirmed (**Figures 3.3**). The result indicates that DRX is one of the primary softening processes.

However, it is worth reminding that, for the present deformation condition (1000°C / 10^{-3} s^{-1}) the observed DRX fraction was relatively low (2% ≤ f_{DRX} ≤ 17%), shown in **Figure 3.5**. By that, it means, most of the material volume could be undergoing deformation probably by dislocation slip. In that sense, it is apparent that DRX may not be the primary reason for the continuous decrease of the flow stress. Incidentally, the present study showed DRX grains deform by grain boundary sliding (GBS) mechanism, shown in **Figure 3.8**. The occurrence of GBS, i.e., deformation confined to narrow regions along grain boundaries can minimize dislocation interactions, thus avoids work-hardening [13,21].

From the above considerations, it could be concluded that the possibility of DRX together with the GBS mechanism could account for the continuous flow softening during high-temperature deformation of the HfNbTaTiZr HEA.

3.5. Conclusions

Dynamic recrystallization and related deformation mechanisms in the equiatomic HfNbTaTiZr HEA were systematically studied by the use of hot-compression test at 1000°C for the strain rate 10^{-3} s^{-1}. Based on systematic microstructural observations, the following conclusions were drawn:

1. The stress-strain behavior of HfNbTaTiZr HEA, hot-deformed at 1000°C for the strain rate 10^{-3} s^{-1} showed a sharp drop followed by continuous flow-softening.

2. The microstructural observations confirmed evolution of the characteristic DRX necklace structure preceded by significant grain boundary bulging of the initial grain boundaries. Careful microstructural evaluation showed DRX grains had near ultra-fine grain size, d ~ 1.5 μm. DRX grains having grain size ~1.5 μm showed inhibited grain growth at high temperature. The first formed DRX grains had

orientation similar to the parent grain. However, the progress of deformation randomized the DRX grains orientations.

3. DRX grains deforming by grain boundary sliding (GBS) mechanism was confirmed. The phenomenon of DRX grains texture randomization and high temperature DRX grain size stability was attributed to the occurrence of GBS.

4. The progress of deformation during the occurrence of GBS has developed mesoscopic bands that interconnected several grains along the DRX necklace structure. As the deformation strain was increased until ε ~0.69, several interconnected bands showed diamond shaped grains. Moreover, microstructural characteristics revealed a transition of 'Y'-type junctions into 'T'-type or 'X'-type junctions. GBS accommodated by triple junction migration was assumed as one of the reasons for the development of mesoscopic bands and the transition of 'Y'-type junctions into 'T'-type or 'X'-type junctions.

5. Finally, the observed microstructural aspects like DRX and GBS were correlated with the continuous flow-softening observed in the stress-strain curve.

References

[1] B.J. E., H.P. Bernhard, M.N. Francis, The recrystallization process in some polycrystalline metals, Proc. R. Soc. London. Ser. A. Math. Phys. Sci. 267 (1962) 11–30. doi:10.1098/rspa.1962.0080.

[2] D. Ponge, G. Gottstein, Necklace formation during dynamic recrystallization: mechanisms and impact on flow behavior, Acta Mater. 46 (1998) 69–80. doi:https://doi.org/10.1016/S1359-6454(97)00233-4.

[3] M.J. Luton, C.M. Sellars, Dynamic recrystallization in nickel and nickel-iron alloys during high temperature deformation, Acta Metall. 17 (1969) 1033–1043. doi:https://doi.org/10.1016/0001-6160(69)90049-2.

[4] W. Roberts, H. Boden, B. Ahlblom, Dynamic recrystallization kinetics, Met. Sci. 13 (1979) 195–205. doi:10.1179/msc.1979.13.3-4.195.

[5] F.J. Humphreys, M. Hatherly, Chapter 13 - Hot Deformation and Dynamic Restoration, in: F.J. Humphreys, M.B.T.-R. and R.A.P. (Second E. Hatherly (Eds.), Elsevier, Oxford, 2004: p. 415–V. doi:https://doi.org/10.1016/B978-008044164-1/50017-7.

[6] R.R. Eleti, T. Bhattacharjee, L. Zhao, P.P. Bhattacharjee, N. Tsuji, Hot deformation behavior of CoCrFeMnNi FCC high entropy alloy, Mater. Chem. Phys. 210 (2018) 176–186. doi:https://doi.org/10.1016/j.matchemphys.2017.06.062.

[7] K.-Y. Tsai, M.-H. Tsai, J.-W. Yeh, Sluggish diffusion in Co–Cr–Fe–Mn–Ni high-entropy alloys, Acta Mater. 61 (2013) 4887–4897. doi:https://doi.org/10.1016/j.actamat.2013.04.058.

[8] C.N. REID, CHAPTER 6 - SLIP ON MORE THAN TWO SYSTEMS—MULTIPLE SLIP, in: C.N.B.T.-D.G. for M.S. REID (Ed.), Int. Ser. Mater. Sci. Technol., Pergamon, 1973: pp. 145–178. doi:https://doi.org/10.1016/B978-0-08-017237-8.50010-1.

[9] A.M. Wusatowska-Sarnek, H. Miura, T. Sakai, Nucleation and microtexture development under dynamic recrystallization of copper, Mater. Sci. Eng. A. 323 (2002) 177–186. doi:https://doi.org/10.1016/S0921-5093(01)01336-3.

[10] N.D. Stepanov, D.G. Shaysultanov, N.Y. Yurchenko, S. V Zherebtsov, A.N. Ladygin, G.A. Salishchev, M.A. Tikhonovsky, High temperature deformation behavior and dynamic recrystallization in CoCrFeNiMn high entropy alloy, Mater. Sci. Eng. A. 636 (2015) 188–195. doi:https://doi.org/10.1016/j.msea.2015.03.097.

[11] D.L. Bourell, H.J. McQueen, Thermomechanical processing of iron, titanium, and zirconium alloys in the bcc structure, J. Mater. Shap. Technol. 5 (1987) 53–73. doi:10.1007/BF02833686.

[12] O.A. Kaibyshev, A.I. Pshenichniuk, V. V Astanin, Superplasticity resulting from cooperative grain boundary sliding, Acta Mater. 46 (1998) 4911–4916. doi:https://doi.org/10.1016/S1359-6454(98)00197-9.

[13] J.E. Dorn, Some fundamental experiments on high temperature creep, J. Mech. Phys. Solids. 3 (1955) 85–116. doi:https://doi.org/10.1016/0022-5096(55)90054-5.

[14] R.C. Gifkins, Grain-boundary sliding and its accommodation during creep and superplasticity, Metall. Trans. A. 7 (1976) 1225–1232. doi:10.1007/BF02656607.

[15] K.A. Padmanabhan, G.E. Davies, Superplasticity, Springer, 1980.

[16] O.A. Kaibyshev, Superplasticity of Alloys, Intermetallides and Ceramics, Springer-Verlag, 1992.

[17] M.F. Ashby, R.A. Verrall, Diffusion-accommodated flow and superplasticity, Acta Metall. 21 (1973) 149–163. doi:https://doi.org/10.1016/0001-6160(73)90057-6.

[18] R. Raj, M.F. Ashby, On grain boundary sliding and diffusional creep, Metall. Trans. 2 (1971) 1113–1127. doi:10.1007/BF02664244.

[19] V. V Astanin, A. V Sisanbaev, A.I. Pshenichnyuk, O.A. Kaibyshev, Self-

organization of cooperative grain boundary sliding in aluminium tricrystals, Scr. Mater. 36 (1997) 117–122. doi:https://doi.org/10.1016/S1359-6462(96)00336-3.

[20] Y. Zhao, L.S. Toth, R. Massion, W. Skrotzki, Role of Grain Boundary Sliding in Texture Evolution for Nanoplasticity, Adv. Eng. Mater. 20 (2018) 1700212. doi:10.1002/adem.201700212.

[21] B. Fazan, O.D. Sherby, J.E. Dorn, Some observations on grain boundary shearing during creep, JOM. 6 (1954) 919–922. doi:10.1007/BF03398039.

Chapter 4

Recrystallization Behavior of the Hot-deformed HfNbTaTiZr Refractory High Entropy Alloy

4.1. Introduction

In **Chapter 3**, dynamic recrystallization (DRX) and related deformation mechanisms of the HfNbTaTiZr HEA during hot-deformation was systematically investigated at 1000°C and 10^{-3} s^{-1}. Microstructural observations confirmed the evolution of DRX grains preceded by the typical grain boundary bulging process; thus microstructures resembled the characteristic DRX necklace structure. DRX grains were found equiaxed and had ultrafine grain size, d ~1.5 μm. It is worth reminding; however, DRX grains were observed strictly along the grain boundary region; thus hot-deformation has resulted partially recrystallized microstructure composed of coarse deformed/unrecrystallized grains and surrounding DRX grains (necklace structure). The resulted microstructure is referred to heterogeneous microstructure.

Generally speaking, dynamic recovery (DRV) is one of the restoration processes that occur in the deformed/unrecrystallized grains during hot-deformation. DRV reduces the stored energy by means of dislocation climb/rearrangement, thus forms clear low angle grain boundaries (LAGBs) having misorientation, (θ), $2° \leq \theta < 15°$ networks and sub-grains in the deformed/unrecrystallized grains [1,2]. Well-known examples for the DRV dominant metals and alloys are β-Ti, β-Zr, and Mo and Al-alloys [3]. On the contrary, as was shown in **Chapters 2 and 3**, during hot-deformation the HfNbTaTiZr BCC-HEA showed the least evidence concerning the formation of LAGBs inside the coarse deformed/unrecrystallized grains.

As was shown in **Chapter 3**, DRX grains deform by grain boundary sliding (GBS) mechanism. In should be noted, furthermore, microstructural observations showed intense LAGBs in the adjacent regions of DRX grains. As discussed in **Chapter 3**, concerning GBS as the dominant deformation mechanism showed similar microstructural characteristics. If that were the case, perhaps it might be possible to assume that the heterogeneous microstructure of the HfNbTaTiZr might undergo GBS dominant deformation; thus the occurrence of GBS in the DRX necklace region must accommodate most of the plastic deformation than grains interiors.

The nature of GBS dominant deformation mechanisms emphasize that the deformed material might lack the necessary driving force (i.e., dislocation density) for the formation of nuclei during subsequent static recrystallization (also referred to post-DRX annealing) [4]. However, a systematic study on the effect of high temperature deformation mechanisms on the static recrystallization behavior is lacking. In this chapter, recrystallization behavior of hot-deformed HfNbTaTiZr HEA is investigated concerning the effect of deformation mechanisms on the later recrystallization behavior.

4.2. Experimental Procedure

Following the results from **Chapter 3**, the HfNbTaTiZr was primarily deformed at 1000°C for the strain rate 10^{-3} s^{-1}, until 50% initial height reduction (equivalent strain, ε = 0.69). **Figure 4.1** shows the experimental flow diagram for the thermo-mechanical processing followed in the present study. Annealing treatment was carried out by maintaining the deformed sample at the deformation temperature for different time intervals such as 300 s, 600 s, 900 s, 1800 s, and 3600 s. Every deformation and a subsequent annealing process were carried out on a fresh as-cast sample. The specimens were water quenched immediately after the annealing and provided for microstructural observations.

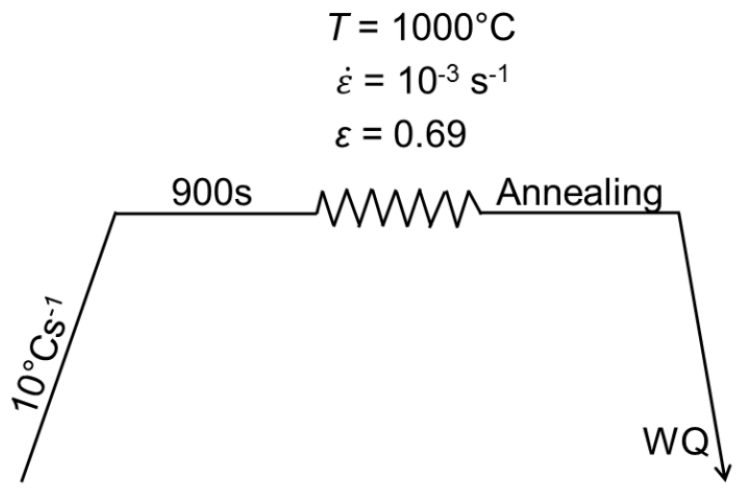

Figure 4.1 Schematic diagram showing the experimental procedure and processing conditions in the compression and subsequent annealing tests of HfNbTaTiZr HEA.

4.3. Results

4.3.1. Hot-deformed Microstructure and Texture

Figure 4.2 shows the microstructure and texture of the HfNbTaTiZr alloy hot-deformed at 1000°C for the strain rate 10^{-3} s^{-1} until 50% of the initial height (equivalent strain, ε = 0.69). Hot-deformation of HfNbTaTiZr alloy showed heterogeneous microstructure having coarse deformed grains surrounded by the characteristic DRX necklace structure. The necklace structure was composed of fine DRX grains (for details see **Chapter 3**). The deformed grains interiors mostly showed red or blue colors, which indicates that the deformed grains preferentially have <001> or <111> orientations parallel to the C.A. Texture measurement of the deformed grains confirmed <001> fiber texture (**Figure 4.2 (b)**), whereas the DRX grains showed no preferred orientation (**Figure 4.2 (c)**). [DRX grains were extracted using grain orientation spread (GOS) approach, which was discussed in **Chapter 2**. Grains satisfying GOS ≤ 2° criteria are considered as DRX grains.]

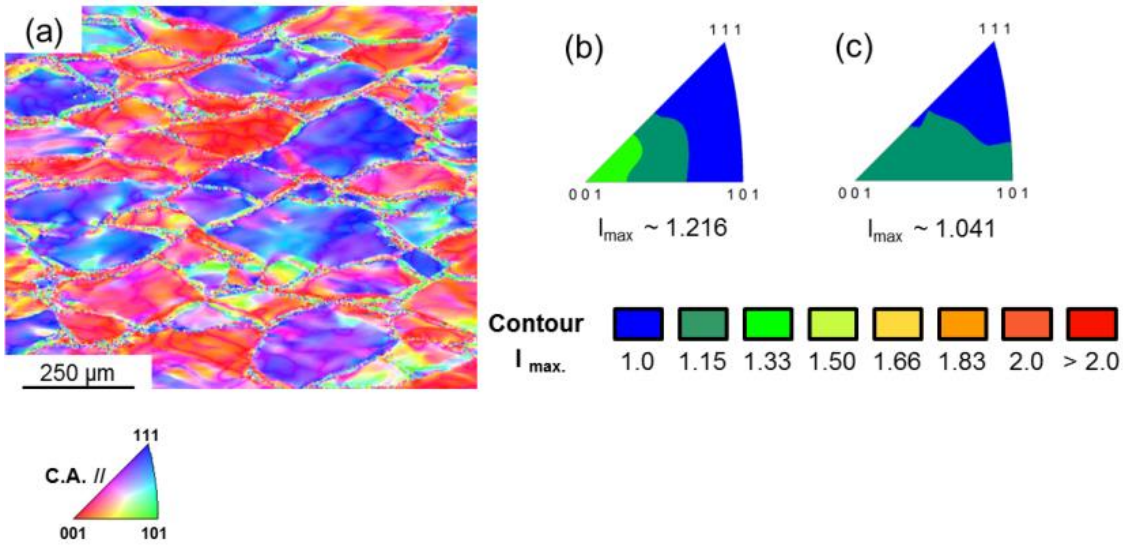

Figure 4.2 (a) EBSD inverse pole figure (IPF) map showing the microstructure of hot-deformed HfNbTaTiZr HEA at 1000°C for the strain rate 10^{-3} s^{-1} until 50% of initial height, (b) EBSD inverse pole figure (IPF) plot showing crystallographic orientations parallel to the compression axis (C.A.) of the unrecrystallized regions (*GOS* > *2*°), (c) in the recrystallized regions (*GOS* ≤ *2*°).

4.3.2. Annealing Behavior of the Hot-deformed Microstructure

Figure 4.3 shows the hot-deformed and subsequently annealed microstructures of HfNbTaTiZr HEA for various time intervals. Microstructures shown in **Figure 4.3** represent grain boundary maps superimposed on image quality (IQ) maps obtained from the EBSD measurement, where red and blue lines indicate low angle grain boundaries (LAGBs) having misorientations (θ), $2° \leq \theta < 15°$, and high angle grain boundaries (HAGBs) with $\theta \geq 15°$, respectively. Microstructural observations indicated that the hot-deformed microstructure was highly stable until 600 s during annealing. However, prolonged annealing time intervals led to rapid grain growth. The relatively more

homogeneous microstructure was observed at 3600 s. It should be mentioned; furthermore, it was apparent that the deformed grains were consumed mostly by the grain growth of pre-existing DRX grains. *(From here on, the grain coarsened DRX grains during annealing will be referred to recrystallized grains).* **Figure 4.4** shows the inverse pole figure (IPF) maps of the recrystallized grains corresponding to **Figure 4.3**. Colors in the IPF maps correspond to crystallographic orientations parallel to the compression axis (C.A.). Recrystallized grains showed no preferred orientation. **Figure 4.5** shows the annealing behavior of the hot-compressed HfNbTaTiZr HEA showing the effect of annealing time on the recrystallized grain size.

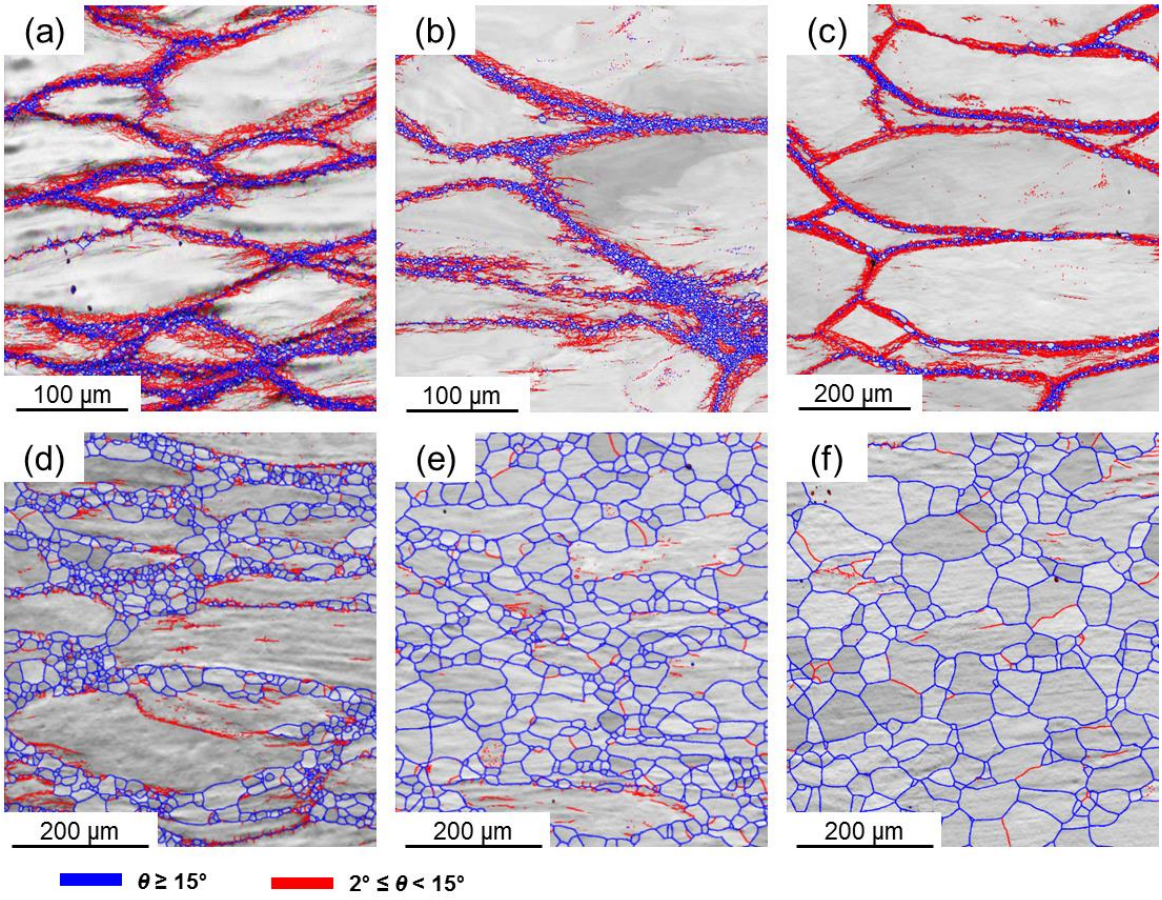

Figure 4.3 EBSD grain boundary maps superimposed on image quality maps showing the annealing behavior of the hot-compressed and subsequently annealed HfNbTaTiZr HEA. (a) as-deformed at 1000°C for the strain rate 10^{-3} s^{-1}, (b) subsequently annealed at 1000°C for 300 s, (c) 600 s, (d) 900 s, (e) 1800 s, and (f) 3600 s. Low angle grain boundaries with misorientations (θ), $2° \leq \theta < 15°$ and high angle grain boundaries with $\theta \geq 15°$ are shown in red and blue lines, respectively. Compression axis during hot-compression was parallel to the vertical axis of microstructures.

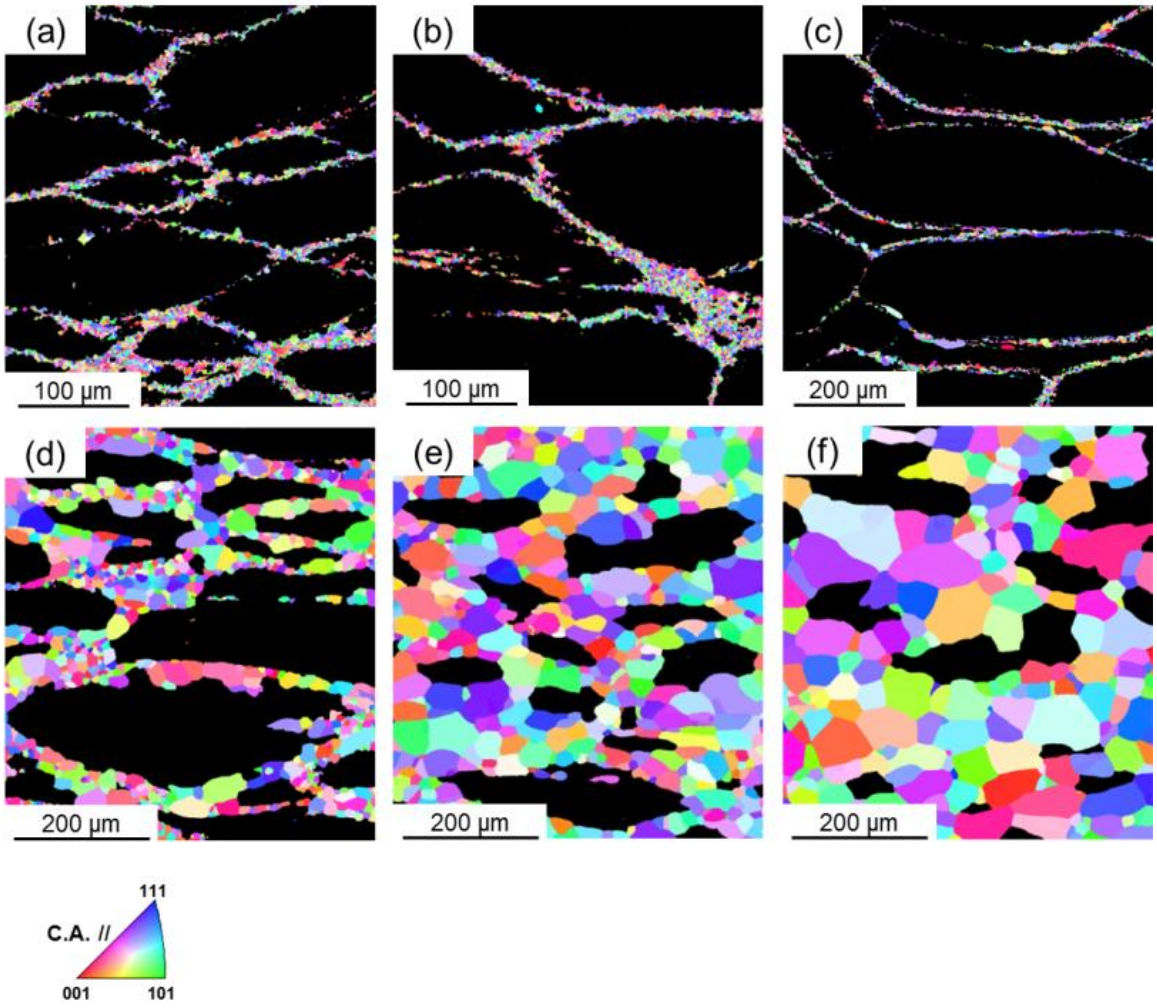

Figure 4.4 EBSD inverse pole figure (IPF) maps of the hot-compressed and subsequently annealed HfNbTaTiZr HEA showing recrystallized regions (*GOS* ≤ *2°*). (a) as-deformed at 1000°C for the strain rate 10^{-3} s^{-1}, (b) subsequently annealed at 1000°C for 300 s, (c) 600 s, (d) 900 s, (e) 1800 s, and (f) 3600 s. Colors in the IPF maps correspond to crystallographic orientations parallel to the compression axis (C.A.). Compression axis during hot-compression was parallel to the vertical axis of microstructures.

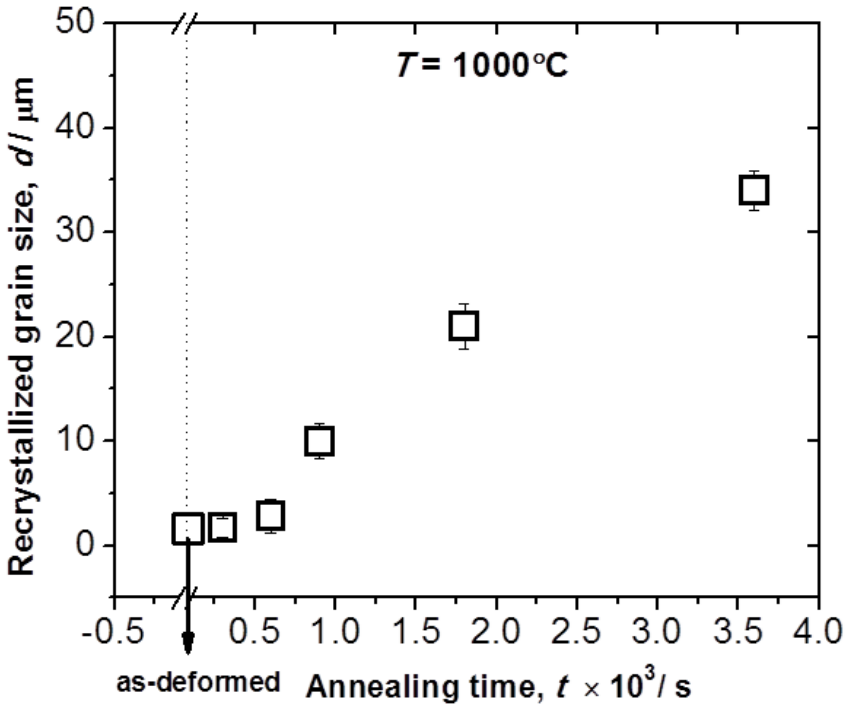

Figure 4.5 Annealing behavior of the hot-compressed HfNbTaTiZr HEA showing the effect of annealing time on the recrystallized grain size.

Usually, during post-deformation annealing, the strain-hardened deformed grains are expected to undergo recrystallization by means of nucleation and grain growth, whereas DRX grains undergo grain coarsening under prolonged annealing time [2]. However, the present experimental results (**Figures 4.3**) indicated grain growth of pre-existing DRX grains as the primary recrystallization process during the post-DRX annealing of the hot-deformed HfNbTaTiZr HEA. Moreover, the development of LAGB networks or sub-grains that are typically observed during annealing of metallic materials was least observed in the present study [2].

4.4. Discussions

4.4.1. Static Recrystallization and Related Restoration Processes

Annealing the hot-deformed HfNbTaTiZr alloy showed recrystallization by grain growth as the primary restoration process (**Figure 4.3**). It was apparent that the classical nucleation process, i.e., the formation of new strain-free grains was least observed. **Figure 4.6** shows the annealing behavior of the hot-deformed HfNbTaTiZr HEA showing the number of recrystallized grains per unit area as a function of the annealing time. The observed number of recrystallized grains per unit area decreased as the annealing time was increased. Decreased recrystallized grains during annealing suggested nucleation of new grains might not have happened.

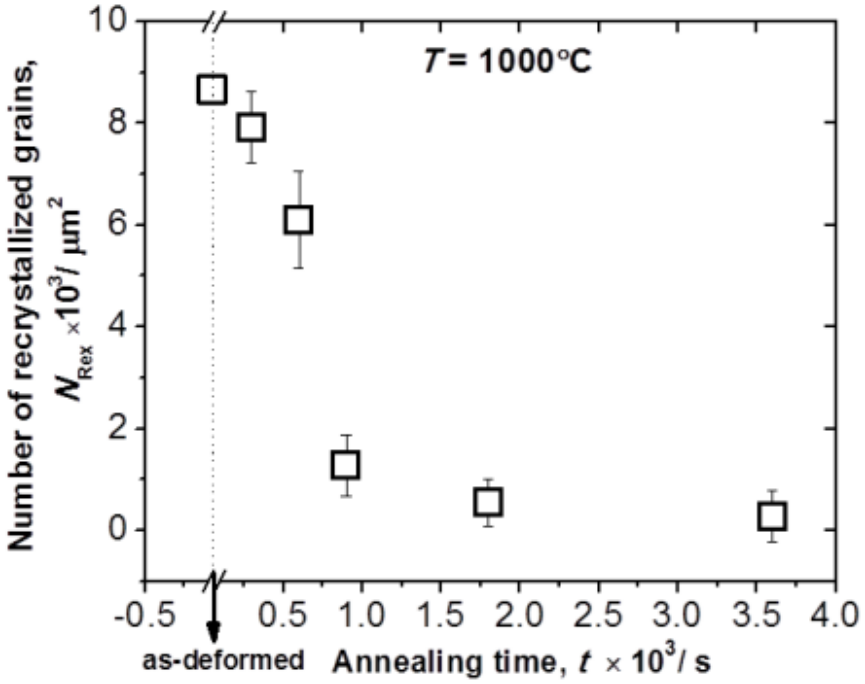

Figure 4.6 Annealing behavior of the hot-deformed HfNbTaTiZr HEA showing the number of recrystallized grains per unit area as a function of the annealing time.

Generally speaking, the driving force for recrystallization is provided mostly by the dislocation density present in the deformed material. According to Cahn, in any homogeneously deformed grain, recrystallization by nucleation of new strain-free grains cannot occur [5]. Correspondingly, Honeycombe [6] and Gilman [7] showed Cadmium and Zinc respectively would not recrystallize after deformed in tension associated with the homogeneous deformation. Such behavior is considered since no part of grain interior differs in orientation from any other by an angle sufficient to make a large-angle boundary.

In that sense, the present annealing behavior of the hot-deformed HfNbTaTiZr HEA possibly shows some insights into the prior hot-deformed microstructure. The EBSD inverse pole figure (IPF) map corresponding to the deformed microstructure showed rather uniform orientation in the grains interiors, shown in **Figure 4.2**. Moreover, the deformed grains were confirmed preferentially oriented to <001> orientation parallel to the C.A. As is known <001> orientation is one of the stable deformation textures of BCC metals and alloys deformed in compression, which indicates that the deformed grains were plastically deformed by conventional dislocation slip, like {110}<111>, {112}<111>, and {123}<111> [8]. Usually, the stable <001> orientation is often expressed to have low stored energy. It has been well known that the orientations having low stored energy do not tend to recrystallize by means of classical nucleation, instead undergo recovery [9].

Furthermore, generally speaking, annealing the deformed material often leads to dislocations annihilation or rearrangement. Dislocations rearrangement at least by dislocation climb would lead to the development of LAGB networks. Development of LAGBs and well-defined subgrain structures during hot-deformation and subsequent annealing were reported in several metals and alloys [9]. Here, it was surprising to note that annealing the hot-deformed HfNbTaTiZr alloy showed least evidence for the formation of LAGB networks in the deformed grains interiors. Instead, as shown in **Figure 4.7**, the distribution of LAGBs in the annealed microstructures decreased with the increased annealing time.

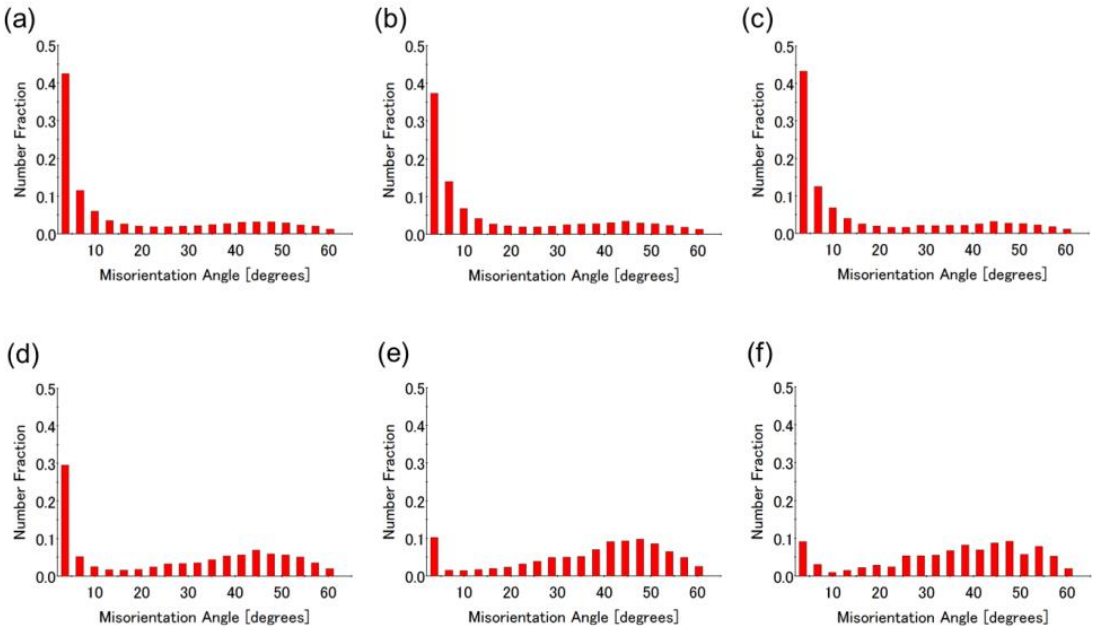

Figure 4.7 Misorientation angle distributions corresponding to the microstructures shown in Figure 4.3. (a) as-deformed at 1000°C for the strain rate 10^{-3} s^{-1}, (b) subsequently annealed at 1000°C for 300 s, (c) 600 s, (d) 900 s, (e) 1800 s, and (f) 3600 s.

Here, it is worth reminding that in the present study the HfNbTaTiZr alloy was hot-compressed until 50% of the initial height (the equivalent true strain, ε ~0.69) before subjecting specimens to the annealing treatment. Although 50% deformation is relatively large, the absence of conventional annealing features is rather strange. In that case, annealing behavior of the HfNbTaTiZr must be strongly affected by the as-deformed high-temperature mechanisms. As shown in **Chapter 3**, the necklace DRX structure can deform by grain boundary sliding (GBS) mechanism. It was also shown that the occurrence of GBS along the necklace structure developed mesoscopic bands along the DRX necklace structure which might accommodate significant amount of plastic deformation. If that were the case, it could be assumed that grains interiors might not have sufficient dislocation density to allow the occurrence of nucleation of grains or the formation of LAGB networks.

As a result, recrystallization occurs exclusively by the migration of existing high-angle boundaries, i.e., by the growth of pre-existing DRX grains.

It was clear that the grain growth of pre-existing DRX grains consumed the coarse deformed/unrecrystallized grains. In other words, the high angle boundary migration appeared the primary recrystallization process during the static recrystallization of the hot-deformed HfNbTaTiZr HEA. An identical behavior is often referred to as strain-induced boundary migration (SIBM). Generally speaking, in the SIBM, the deformed volume is restored due to the grain boundary migration at the expense of the neighboring deformed grain. One of the characteristic behaviors of SIBM is that it does not cause changes in the recrystallization texture [3,9]. To experimentally evaluate this, recrystallization texture of the hot-deformed and subsequently annealed HfNbTaTiZr alloy was analyzed and shown in **Figure 4.8**. In the hot-deformed state, recrystallized DRX grains showed weak and random texture. As discussed in **Chapter 3**, DRX grains deform by grain boundary sliding (GBS) mechanism. The occurrence of GBS was attributed to the random texture of DRX grains. It should be noted, however, the random texture of the hot-deformed condition prevailed during the subsequent annealing process. In other words, grain growth during recrystallization showed no preferred orientation. Considering the similarities of the present observations with the classical SIBM mechanism, recrystallization by grain growth due to grain boundary migration is realized as probably the only restoration process during annealing the hot-deformed HfNbTaTiZr HEA.

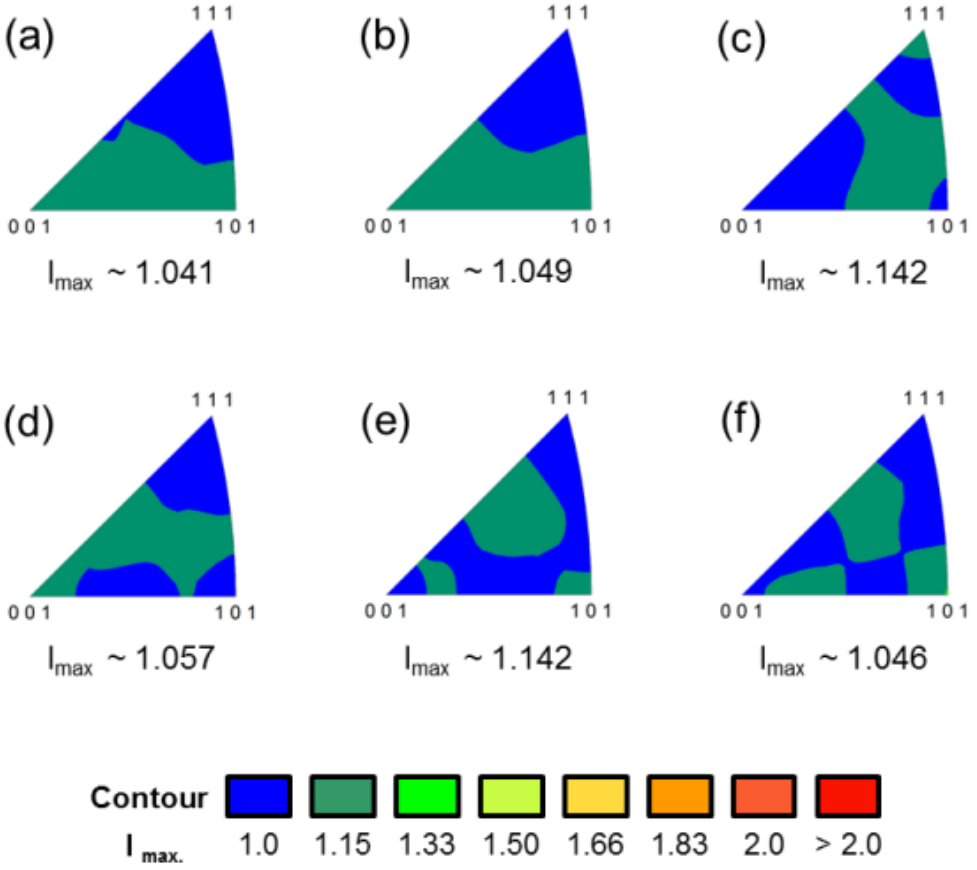

Figure 4.8 EBSD inverse pole figures (IPF) showing crystallographic orientations parallel to the compression axis (C.A.) in the recrystallized regions (*GOS* ≤ *2*°) in the specimens deformed and subsequently annealed. (a) Deformed at 1000°C for the strain rate 10^{-3} s^{-1} until 50%, (b-f) Subsequently annealed at 1000°C for 300 s, 600 s, 900 s, 1800 s, and 3600 s respectively.

4.5. Conclusions

Recrystallization behavior of the hot-deformed HfNbTaTiZr HEA was systematically investigated at the deformed temperature 1000°C for different annealing time intervals. Based on the microstructural observations, the following conclusions were drawn:

1. Annealing the hot-compression specimens showed high microstructural stability until 600 s. However, annealing above 900 s showed rapid grain growth of the pre-existing DRX grains and the recrystallized grain size continuously increased with the annealing time.

2. During the annealing process, the classical recrystallization mechanism by means of nucleation of new strain-free grains was least observed. Furthermore, the progress of microstructural changes during annealing lacked the development of well-defined sub-grain structures in the deformed grains interiors.

3. The lack of typical annealing characteristics was assumed due to the lack of necessary dislocation density in the hot-deformed grains, which was accounted for the occurrence of extensive grain boundary sliding (GBS) along the DRX grains during hot-deformation.

4. Grain boundary migration was realized as the primary and probably the only effective means of restoration process for the hot-deformed HfNbTaTiZr alloy during recrystallization. Accordingly, the prevailed random DRX grains texture during recrystallization supported the experimental findings.

References

[1] T. Sakai, M. Ohashi, K. Chiba, J.J. Jonas, Recovery and recrystallization of polycrystalline nickel after hot working, Acta Metall. 36 (1988) 1781–1790. doi:https://doi.org/10.1016/0001-6160(88)90246-5.

[2] T. Sakai, A. Belyakov, R. Kaibyshev, H. Miura, J.J. Jonas, Dynamic and post-dynamic recrystallization under hot, cold and severe plastic deformation conditions, Prog. Mater. Sci. 60 (2014) 130–207. doi:https://doi.org/10.1016/j.pmatsci.2013.09.002.

[3] R.D. Doherty, D.A. Hughes, F.J. Humphreys, J.J. Jonas, D.J. Jensen, M.E. Kassner, W.E. King, T.R. McNelley, H.J. McQueen, A.D. Rollett, Current issues in recrystallization: a review, Mater. Sci. Eng. A. 238 (1997) 219–274. doi:https://doi.org/10.1016/S0921-5093(97)00424-3.

[4] O.A. Kaibyshev, R.Z. Valiev, V. V Astanin, On the nature of superplastic deformation, Phys. Status Solidi. 35 (1976) 403–413. doi:10.1002/pssa.2210350144.

[5] R.W. Cahn, A New Theory of Recrystallization Nuclei, Proc. Phys. Soc. Sect. A. 63 (1950) 323. http://stacks.iop.org/0370-1298/63/i=4/a=302.

[6] R.W.K. Honeycombe, INHOMOGENEITIES IN THE PLASTIC DEFORMATION OF METAL CRYSTALS. II. X-RAY AND OPTICAL MICROGRAPHY OF ALUMINIUM, J. Inst. Met. 80 (1951).

[7] J.J. Gilman, Structure and polygonization of bent zinc monocrystals, Acta Metall. 3 (1955) 277–288. doi:https://doi.org/10.1016/0001-6160(55)90065-1.

[8] C.N. Reid, W.S. Owen, Deformation Geometry for Materials Scientists: International Series on Materials Science and Technology, first ed., Pergamon, Braunschweig, 1973.

[9] F.J. Humphreys, M. Hatherley, Recrystallization and Related Annealing Phenomena, second ed., Elsevier, Oxford, 2004.

Chapter 5

Lack of Normal Hardening in HfNbTaTiZr High Entropy Alloy

5.1. Introduction

The deformation mechanisms and microstructure evolution in HfNbTaTiZr HEA during thermo-mechanical processing at elevated temperatures were systematically studied in **Chapters 2, 3, and 4**. Unfortunately, homogeneous microstructures in HfNbTaTiZr were unable to obtain due to the nature of deformation mechanisms at elevated temperatures which were already discussed in the previous chapters.

It should be noted however, thermo-mechanical processing using cold rolling and subsequent annealing is one of the most commonly employed processes to fabricate homogeneous microstructures. Annealing the cold rolled sheets at high temperatures for different time intervals facilitates microstructure control having various grain sizes. Grain refinement is one of the well-known strengthening mechanisms of metals and alloys; thus, mechanical properties of metals and alloys often depend on the grain size. Improved mechanical properties of different metals and alloys were reported by using grain refinement approach [1]. According to the classical Hall-Petch relationship, decreasing the grain size increases the yield strength. The inverse relationship between yield strength and grain size is expressed as [2],

$$\sigma_y = \sigma_0 + k_{HP} d^{-1/2} \tag{5.1}$$

where σ_y is the yield strength (MPa), σ_0 is the friction stress which represents the intrinsic lattice resistance to the dislocation motion (MPa), k_{HP} is Hall-Petch coefficient which

measures the effective strengthening contribution of the grain boundary (MPa.μm$^{0.5}$), d is the average grain size (μm).

In recent years, grain refinement approach has been extensively used to study the mechanical properties of high entropy alloys (HEAs). Several face-centered cubic (FCC) high entropy and medium entropy alloys were reported having an excellent combination of strength and ductility. Otto et al. [3] reported the grain size dependence of yield strength of the CoCrFeMnNi alloy having k_{HP} ~494 MPa.μm$^{0.5}$. Sohn et al. [4] reported the VCoNi medium entropy alloy (MEA) having k_{HP} ~864 MPa.μm$^{0.5}$ remarkably large. The measured k_{HP} values indicate a strong dependence of yield strength on the grain size; implies yield strength of FCC-HEAs and MEAs can be effectively improved by employing grain refinement approach. On the other hand, FCC-HEAs and MEAs were reported to exhibit high friction stress, σ_0 associated with the lattice distortion effect of HEAs [5–7].

Wang et al. [8] reported the effect of lattice distortion on the yield strength of BCC-HEAs. Their investigation showed that the exceptional solid solution strengthening of BCC-HEAs is due to severe lattice distortion effect induced by the local atomic size and modulus differences. Adding to that, Song et al. [9] reported that the lattice distortion of BCC-HEAs is significantly high compared to the FCC-HEAs. Considering the intrinsic solid solution strengthening of BCC-HEAs, addition of grain refinement strengthening might significantly enhance the mechanical properties of BCC-HEAs. However, the effect of grain refinement on mechanical properties of BCC-HEAs was least studied [10]. Therefore, the objective of the present chapter is to fabricate the HfNbTaTiZr BCC-HEA having various grain sizes using conventional cold rolling and subsequent annealing and understand the effect of grain size on mechanical properties.

5.2. Experimental Procedures

5.2.1. Cold Rolling and Annealing

The as-cast ingot having dimensions 30 mm (length) x 15 mm (width) x 11.25 mm (height) was cold rolled until 92% initial height reduction. The rolled sheet was annealed in a vacuum atmosphere at 1200°C for different time intervals (4 min, 5 min, 6 min, 8 min, and 10 min). **Figure 5.1** schematically illustrates the thermo-mechanical processing pattern followed in the present study. Annealed specimens were immediately water quenched and provided for microstructural observations.

Tensile specimens having gauge dimensions 2 mm (length) x 1 mm (width) x 0.6 mm (thickness) were cut from the annealed sheets. The rolling direction of the cold rolled sheet was aligned parallel to the longitudinal axes of the tensile specimens. Digital image correlation (DIC) technique was used to measure the precise deformation strain. Tensile tests were performed at ambient temperature for the strain-rate 8.3×10^{-4} s^{-1}.

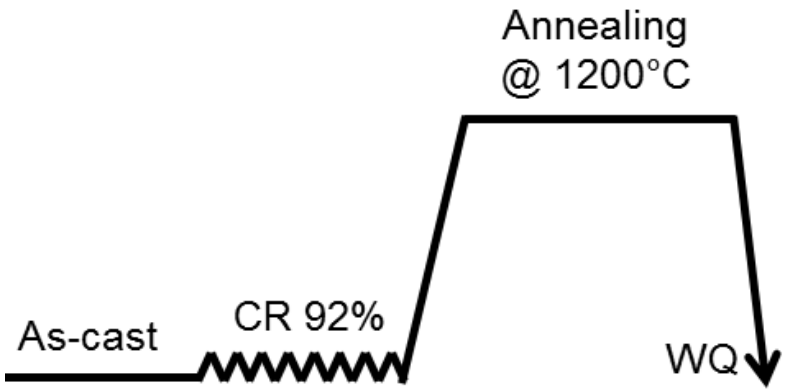

Figure 5.1 Schematic diagram showing the experimental procedure and processing conditions in the cold rolling (CR) and subsequent annealing treatment of the HfNbTaTiZr RHEA.

5.2.2. Microstructural Analyses

For microstructural observations, annealed specimens were mechanically polished until achieving scratch-free surfaces and then electropolished to get mirror-like surfaces. Electropolishing was carried out in a chemical solution containing 10 vol.% $HClO_4$ and 90 vol.% CH_3OH. The chemical solution was maintained at -20°C by adding liquid nitrogen. The final polishing was done at a constant voltage of 20V for 30sec. Electron back-scattering diffraction (EBSD) system and Back-scatter electron (BSE) imaging facility operated in a field emission-scanning electron microscope (FE-SEM, JSM 7100F) at an accelerated voltage of 20 kV was used to obtain microstructural information.

For the transmission electron microscopy (TEM) observation, specimens were mechanically polished until 70 µm thin foils were achieved. Further sample preparation was carried out using conventional twin-jet electropolishing approach, in a chemical solution containing 950 ml CH_3OH, 45 ml H_2SO_4, and 5 ml HF. The chemical solution was maintained at -35°C by adding liquid nitrogen. Twin-jet electropolishing was carried out at 22.5V potential. TEM observations were performed in a JEOL JEM 2010 electron microscope at an accelerating voltage of 200 kV.

5.3. Results

5.3.1. Microstructures

Figure 5.2 shows fully recrystallized microstructures of the HfNbTaTiZr obtained by cold rolling and subsequent annealing. **Figure 5.2 a-c** shows the SEM-BSE images indicating fully recrystallized microstructures having no remnants of the deformed volume. Microstructures shown in **a-c** corresponds to the annealed conditions 1200°C for 4 min, 1200°C for 6 min, and 1200°C for 10 min having average grain sizes 6 µm, 25 µm, and 50 µm respectively. Microstructural observations indicated equiaxed grains having uniformly distributed grain sizes. The average grain size was measured using the line intercept method. **Figure 5.2 d-f** shows EBSD inverse pole figure (IPF) maps suggested the

recrystallized microstructures had no preferred orientation. The colors in the IPF map show crystallographic orientations parallel to the rolling direction (RD) according to the key stereographic triangle shown in **Figure 5.2**. **Figure 5.2 g-i** shows EBSD image quality (IQ) maps confirmed the recrystallized microstructures were mostly composed of high angle grain boundaries (HAGBs) having misorientation (θ), $\theta \geq 15°$. HAGBs are shown in blue lines, whereas low angle grain boundaries (LAGBs) having misorientation (θ), $2° \leq \theta \leq 15°$ are shown in red lines.

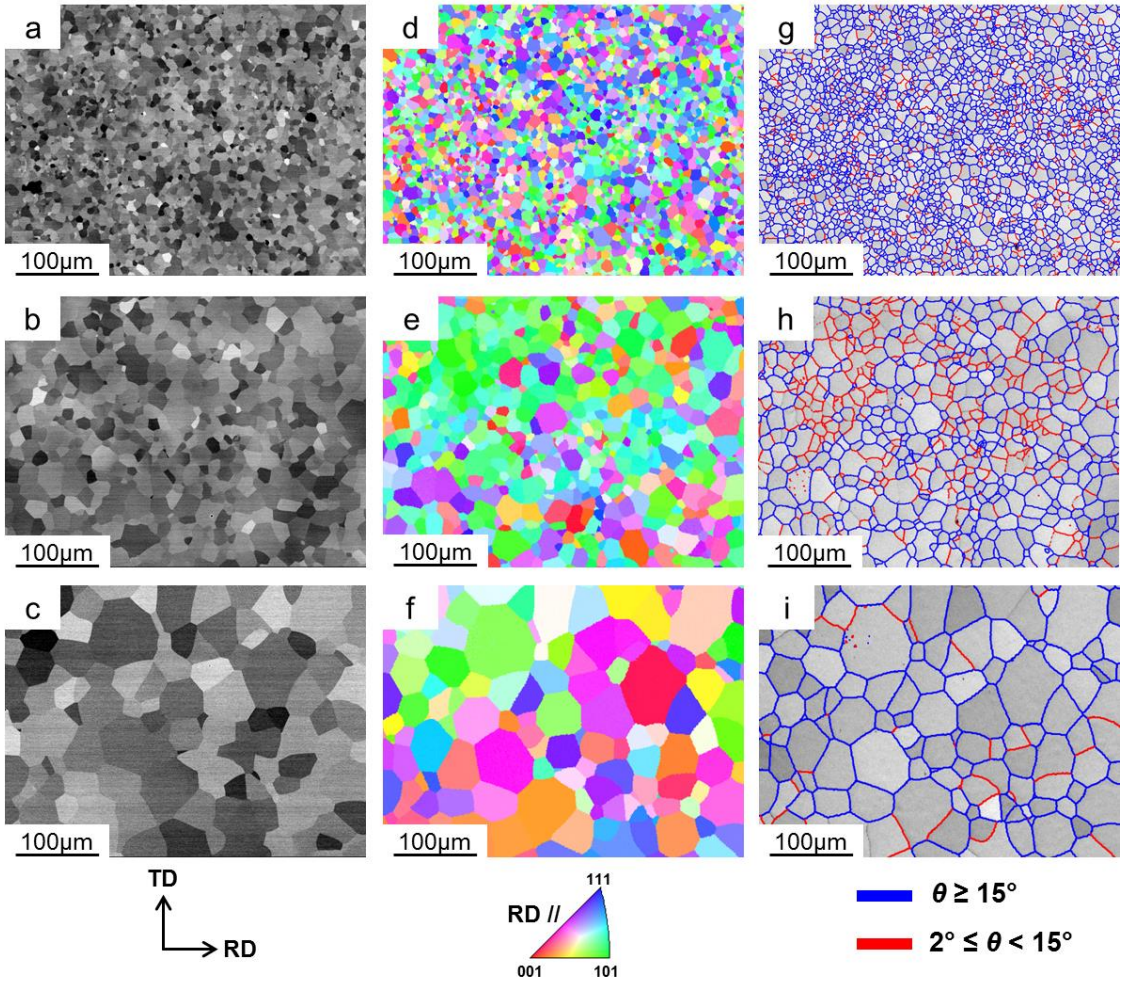

Figure 5.2 Microstructures of thermo-mechanically processed HfNbTaTiZr refractory high entropy alloy showing fully recrystallized and uniformly distributed equiaxed grain sizes: (a-c) SEM-BSE images of (a) 6 μm, (b) 25 μm, and (c) 50 μm, (d-f) EBSD inverse pole figure (IPF) maps showing distribution of grains orientations parallel to the rolling direction, (g-i) EBSD grain boundary and image quality maps confirmed microstructures composed of mostly high angle boundaries. Low angle grain boundaries with misorientations (θ), $2° \leq \theta < 15°$ and high angle grain boundaries with $\theta \geq 15°$ are shown in red and blue lines, respectively.

5.3.2. Stress-Strain Curves

Figure 5.3 shows stress-strain curves of the HfNbTaTiZr tensile deformed at ambient temperature for various grain sizes. **Figure 5.3 a** shows engineering stress-strain curves, whereas **Figure 5.3 b** shows true stress-strain curves. Although HfNbTaTiZr alloy indicated high strength (> 1000 MPa) and ductility (~ 18%), stress-strain curves of all grain sizes showed lack of strain-hardening. It should be noted that stress-strain curves showed discontinuous yielding (sudden transition from elastic stage to plastic deformation stage) rather than a continuous yielding. It is worth mentioning moreover, despite the microstructural similarities prior to the initiation of plastic deformation during tensile tests at ambient temperature and high-temperature compression tests, it was evident that stress-strain curves did not show sharp drop during tensile deformation at ambient temperature.

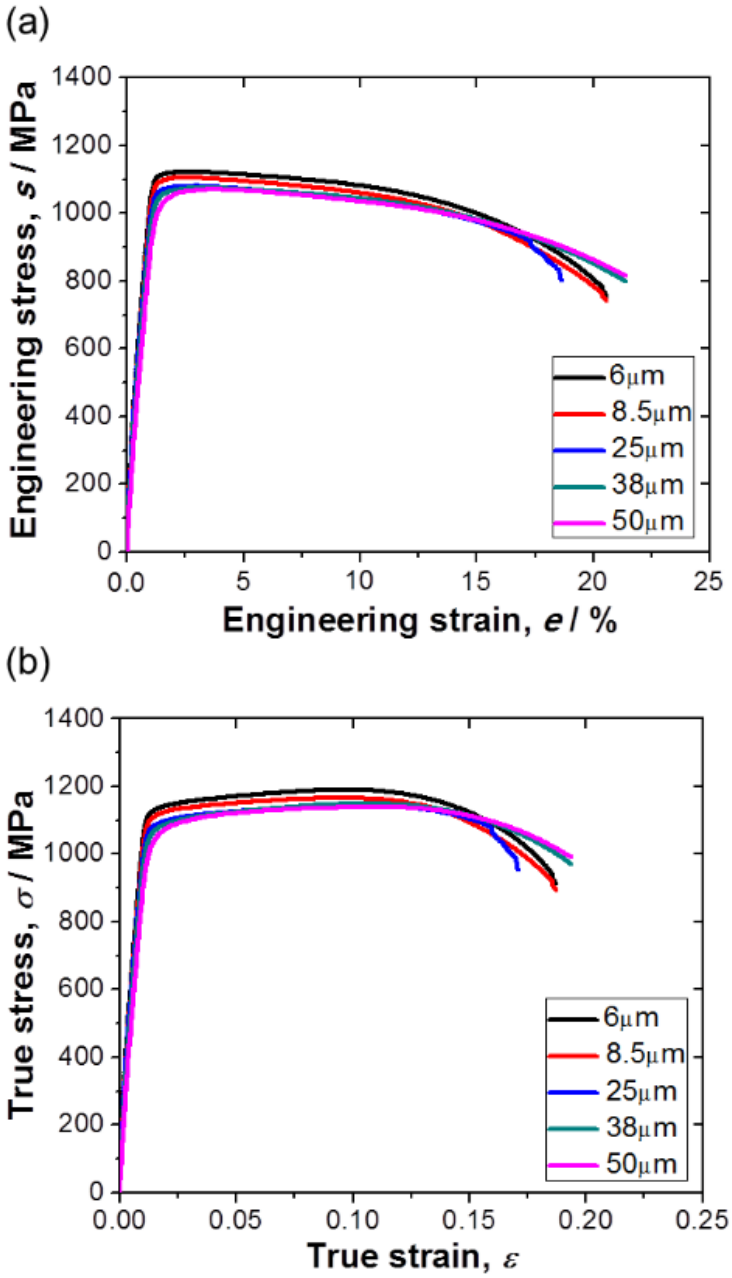

Figure 5.3 Stress-strain curves of the equiatomic HfNbTaTiZr HEA tensile deformed at ambient temperature for various grain sizes. (a) Engineering stress-strain curves, (b) True stress-strain curves.

As was discussed in the introduction section, the dependence of yield strength on the grain size was expressed using Hall-Petch relationship (**Equation 5.1**). **Figure 5.4** shows Hall-Petch relationship of the HfNbTaTiZr alloy for the yield strength ($\sigma_{0.2\%}$) and flow strength at different strain intervals. Here, 0.2% proof stress was used to measure the yield strength. It was interesting to note that the HfNbTaTiZr refractory HEA showed lack of increased yield strength with the decrease of grain size. In this sense, the HfNbTaTiZr alloy is ineffective to the grain refinement strengthening mechanism. Present observations measured the grain boundary strengthening coefficient, k_{HP} ~322 MPa.μm$^{0.5}$ and the friction stress, σ_0 ~998 MPa. It is noteworthy, furthermore, Hall-Petch relationship plotted at different strain intervals showed a decrease of the k_{HP} with the increase of deformation strain, shown in **Figure 5.4**. The measured k_{HP} was observed to be lower, whereas the σ_0 was exceptionally high compared to pure metals and alloys having BCC crystal structure. **Table 5.1** shows the summary of results showing grain boundary strengthening coefficients and friction stress of different metals and alloys having BCC crystal structure. It has been assumed that HEAs show high friction stress which might be primarily due to lattice distortion. The present observation supports high friction stress might be a characteristic property of HEAs. The lack of grain refinement strengthening and low k_{HP} will be discussed in the later part of this chapter by considering the possible deformation mechanisms of HfNbTaTiZr HEA.

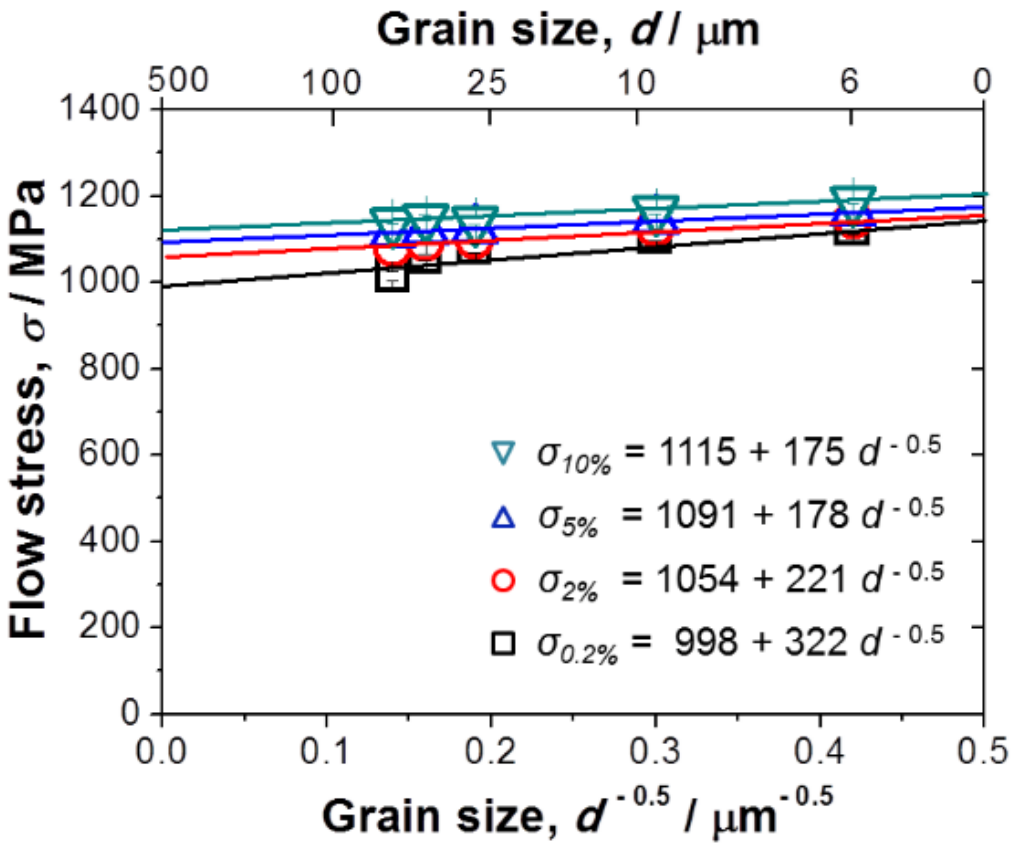

Figure 5.4 Hall-Petch relationship of the HfNbTaTiZr alloy for the yield strength ($\sigma_{0.2\%}$) and flow strength at different strain intervals.

Table 5.1 Summary of results showing grain boundary strengthening coefficient, k_{HP} and friction stress, σ_0 of different BCC metals and alloys.

Metals/Alloys (BCC)	**k_{HP} (MPa.μm$^{0.5}$)**	**Ref.**	**Friction stress, σ_0 (MPa)**	**Young modulus, E (MPa)**	**σ_0/E (×10^{-6})**	**Ref.**
HfNbTaTiZr	322	Present study	998	92	10487	Present study
MoNbTaVW	1462	[11]	1078	Not Available		[11]
$Al_{0.1}$CrNbVMo	811	[12]	1680			[12]
Nb	1051	[13]	120	105	1142	[14]
Ta	1669		80	190	421	
Mo	1536		270	329	820	
V	789		150	128	1171	
Cr	1380 - 2561		320	279	1146	

As shown in **Figure 5.3,** stress-strain behavior of the HfNbTaTiZr lacked strain-hardening; therefore, the strain-hardening exponent of HfNbTaTiZr alloy was evaluated. In general, the plastic flow behavior of metallic materials in the uniform deformation region is expressed by the following relationship,

$$\sigma = K\varepsilon^n \tag{5.2}$$

where, σ is true stress, ε is true strain, n is strain-hardening exponent, K is strength coefficient. **Figure 5.5** shows true stress-strain curve for the 6 μm grain size specimen

within the uniform elongation region. The plot is shown in the log-log scale. The slope of the plot yielded strain-hardening exponent, n ~0.02. Usually, the strain-hardening exponent of metallic materials has values between 0.1 and 0.5 [5]. It is rather surprising that the strain-hardening exponent of HfNbTaTiZr alloy is nearly one order of magnitude lower than other metals and alloys. In this sense, the HfNbTaTiZr alloy can undergo plastic deformation under mostly constant flow stress.

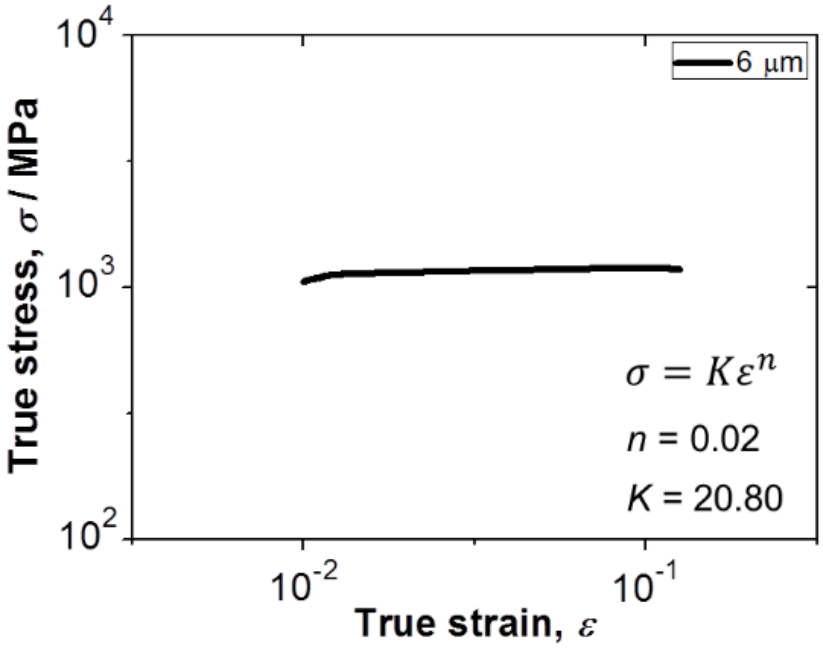

Figure 5.5 Log-log plot of true stress-strain curve for the 6 μm grain size specimen in the uniform plastic deformation region.

5.4. Discussions

5.4.1. Dislocation Density Measurement

5.4.1.1. In-situ X-ray Diffraction Measurements

Conventionally, the dislocation density is measured from TEM observations on samples that are primarily sectioned and mechanically polished thin foils. This approach is referred to ex-situ technique. Ex-situ techniques not only limit the observable sample geometry but also induce mechanical stresses that might alter the dislocation structure. On the other hand, experimental technique such as three-dimensional X-ray diffraction (3D-XRD) has been often used to overcome the limits imposed by ex-situ techniques. 3D-XRD allows characterization of materials in real-time during deformation without damaging the sample, thus referred to in-situ. In the present study, a 3D-XRD experimental technique was employed to evaluate dislocation density in the HfNbTaTiZr HEA. The high-energy synchrotron X-ray radiation source at the Super-Photon ring (SPring-8), Japan facility through the beam line 46 (BL-46XU) was used to perform the test. A picture of the experimental facility and the schematic illustration of the working principle are shown in **Figure 5.6**. The beam energy and the corresponding wavelength were 30 keV and 0.0413 nm respectively. The beam size on the tensile sample was 300 μm along the tensile direction and 1000 μm along the width direction. The tensile test was carried out on the 6 μm grain size specimen at ambient temperature for the strain-rate 8.3×10^{-4} s^{-1}. Tensile specimens having gauge dimensions 10 mm (length) x 3 mm (width) x 0.21 mm (thickness) were cut from the annealed sheets. The rolling direction of the cold rolled sheet was aligned parallel to the longitudinal axes of the tensile specimens. It is noteworthy; furthermore, the tensile test during in-situ XRD measurement was performed without using strain gauge. So, the nomenclature of strain in this session is to be considered as nominal strain. One X-ray diffraction profile was recorded for every 1 s during deformation.

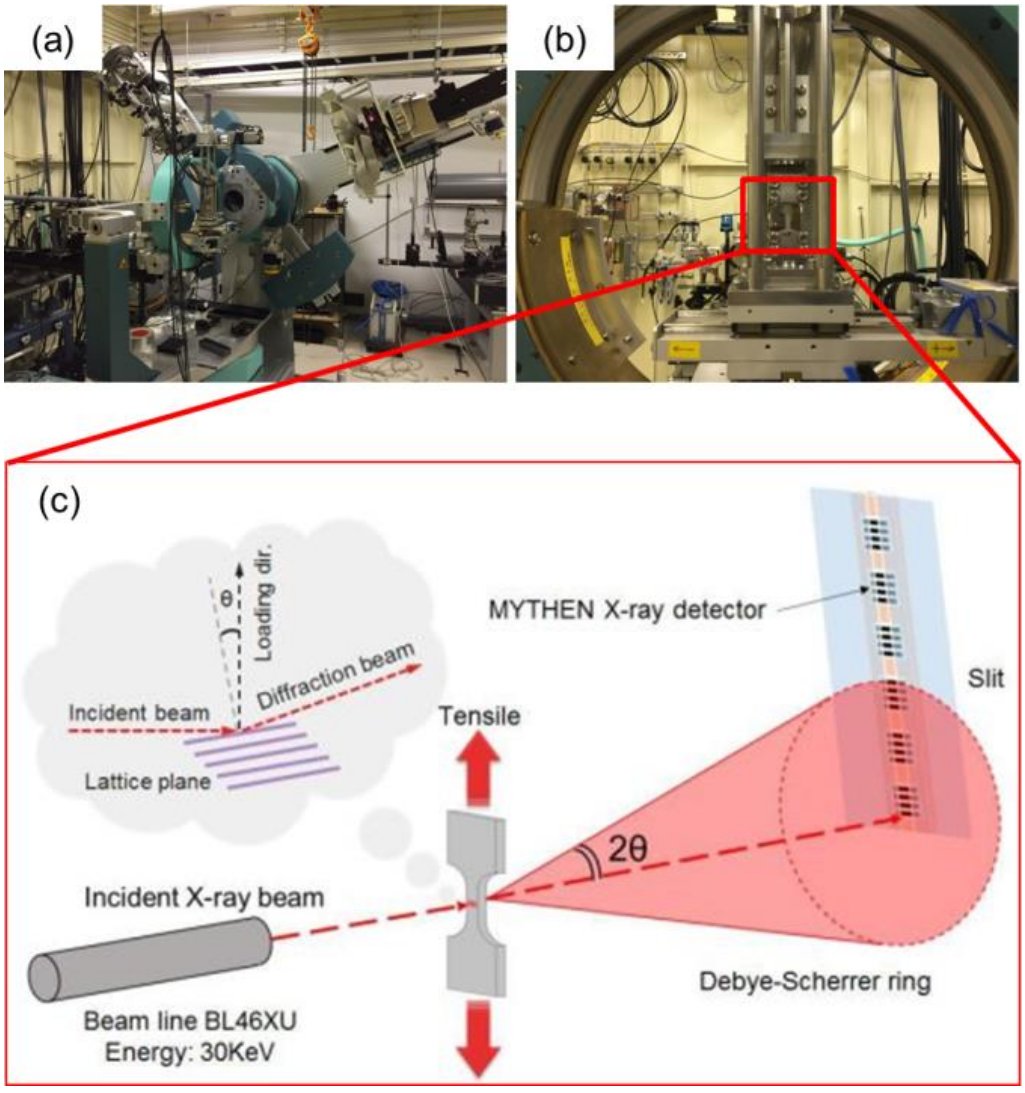

Figure 5.6 The experimental facility at Spring-8 for in-situ tensile tests using high-energy synchrotron X-ray radiation. (a) A picture of the experimental facility at the Spring-8, (b) Beam zone showing the fixed tensile sample, (c) Schematic illustration of the experimental set-up at the Spring-8, BL46XU.

Figure 5.7 shows the stress-strain curve and the corresponding in-situ XRD profiles at different strain intervals obtained during deformation. **Figure 5.7 a** shows the nominal stress-strain curve, and **Figure 5.7 b** shows the XRD profile for the fully recrystallized specimen before starting the tensile test e = 0%, and XRD profiles after the onset of plastic flow, shown as $e \geq 5\%$. XRD profiles showed the HfNbTaTiZr alloy retained the initial BCC phase during tensile deformation.

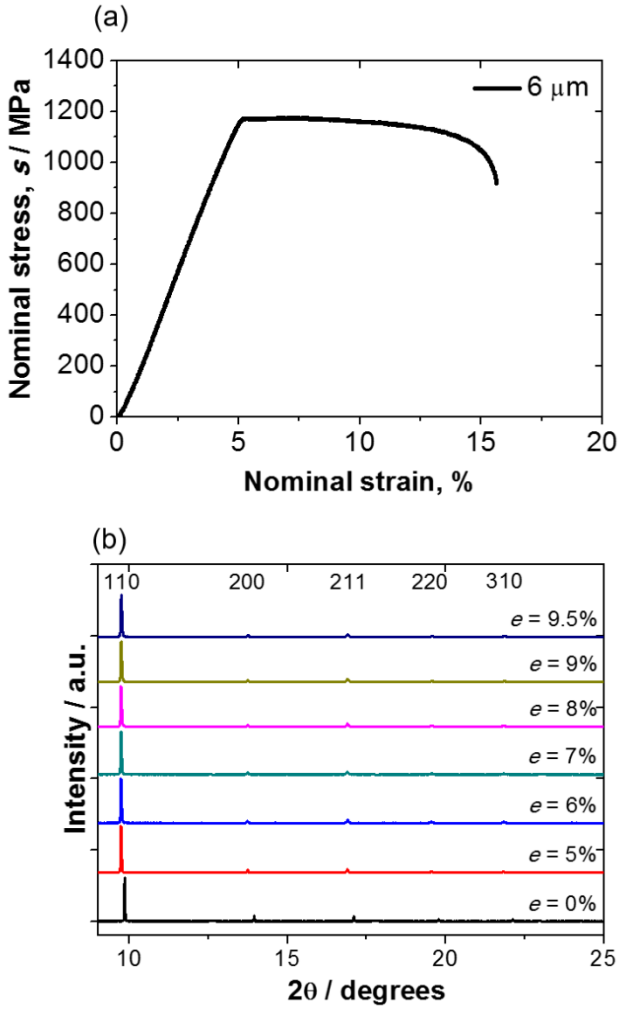

Figure 5.7 (a) The nominal stress-strain curve of HfNbTaTiZr alloy obtained during in-situ tensile test, (b) In-situ XRD profiles corresponding to different tensile strain intervals.

Figure 5.8 shows the overlapped XRD profiles of (110) peak. The sharp shift of the XRD peak from e = 0% to 5% towards lower 2θ is primarily due to elastic deformation. It should be noted however, the peak shift between before beginning the test (i.e., e = 0%) and after the onset of plastic deformation (i.e., e = 5%) was large. It was apparent that the peak width of XRD profiles increased after the onset of deformation but remained mostly unchanged during the progress of deformation. Increased peak width (Δ2θ) is often associated with the non-uniform strain distribution which might be primarily due to the crystallographic slip of dislocations.

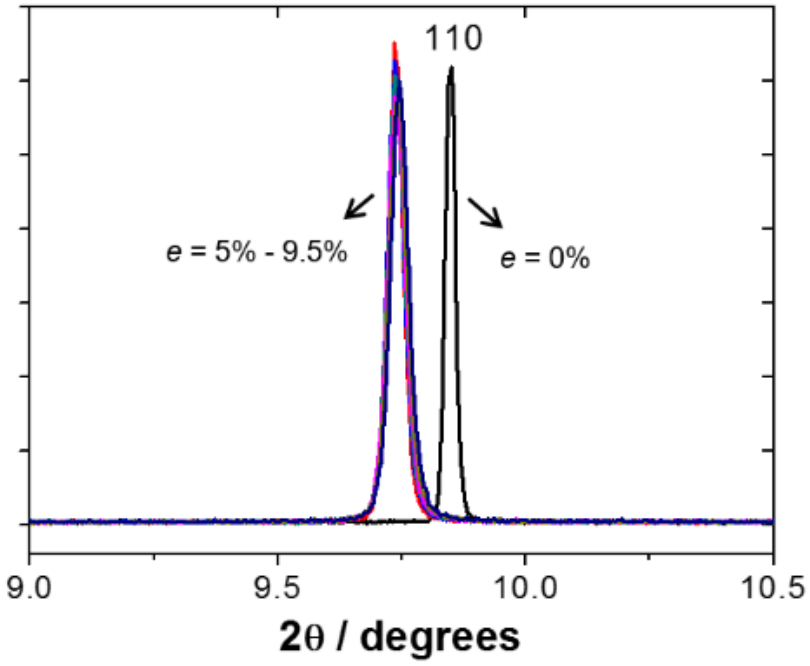

Figure 5.8 Overlapped in-situ XRD profiles of (110) diffraction peaks at different strain intervals.

According to the Williamson-Hall (WH) analysis method, the increased peak width can be used to estimate the apparent microstrain (ε) during deformation. The relationship between $\Delta 2\theta$ and ε is expressed as [15],

$$\frac{\Delta 2\theta.\cos\theta}{\lambda} = \frac{0.9}{D} + \frac{2\varepsilon.\sin\theta}{\lambda} \tag{5.3}$$

where, $\Delta 2\theta$ is full width at half maximum (FWHM) of the diffraction peak (°), θ is Bragg's diffraction angle (°), λ is the wavelength of the beam (nm), D is crystallite size (nm), ε is microstrain. The ε can be estimated from the slope of WH plot. **Figure 5.9** shows WH plot from the XRD profiles obtained during deformation.

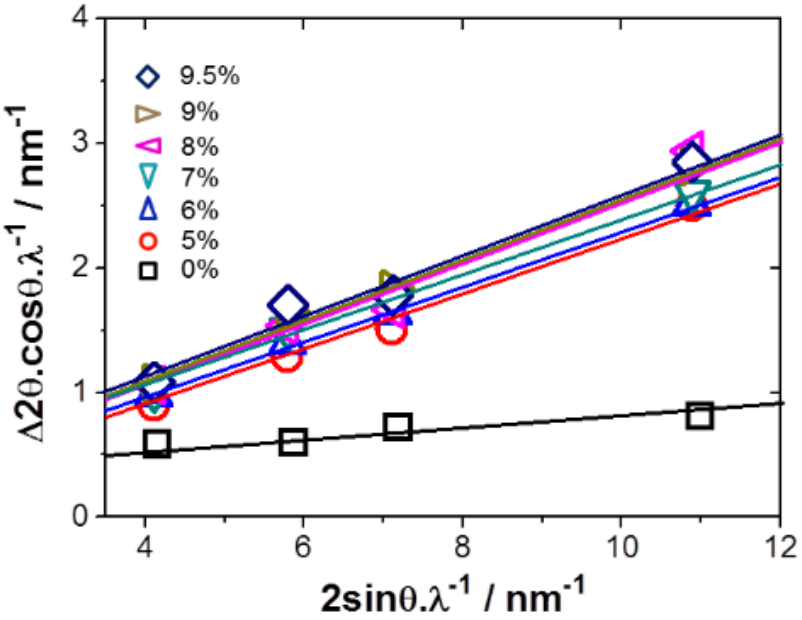

Figure 5.9 Williamson-Hall plot of HfNbTaTiZr HEA for different strain intervals derived from the in-situ XRD profiles.

Using the obtained microstrain (ε), according to Williamson-Smallman, dislocation density, ρ can be calculated by using the following relationship [16],

$$\rho = 14.4\frac{\varepsilon^2}{b^2} \tag{5.4}$$

where, ρ is dislocation density (m^{-2}), ε is microstrain obtained from the slope of WH plot, b is burgers vector (nm). For the present HfNbTaTiZr alloy, b = 0.295 nm [17].

Figure 5.10 shows the estimated dislocation density during in-situ tensile deformation. For the matter of convenience and visual appreciation, the change of dislocation density during deformation is represented with the stress-strain curve. It was clear that the dislocation density rapidly increased after the onset of plastic deformation; however, the dislocation density was observed nearly constant during the progress of plastic deformation. It should be noted, furthermore, the fully recrystallized HfNbTaTiZr HEA, i.e., e = 0% showed dislocation density ~2.0×10^{17} m^{-2}. After the onset of plastic deformation, the dislocation density increased by two orders of magnitude ~1.2×10^{19} m^{-2}.

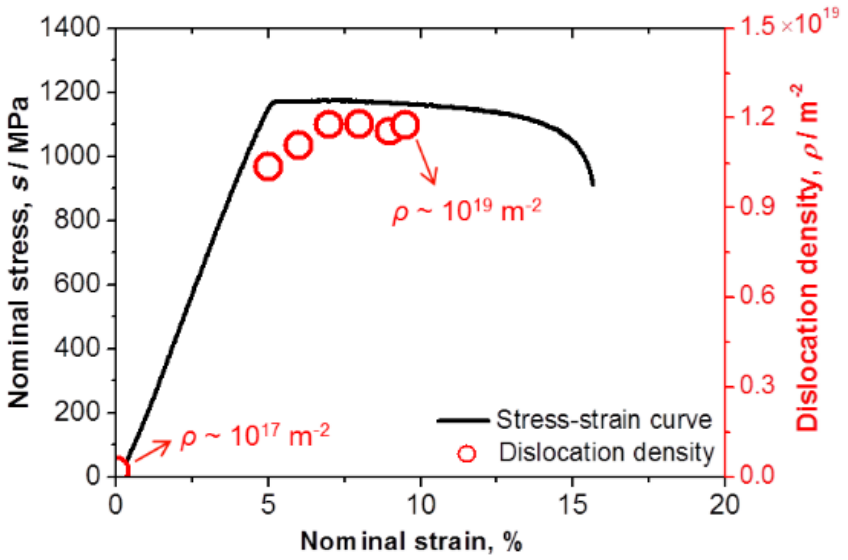

Figure 5.10 Estimated dislocation density during tensile deformation of HfNbTaTiZr HEA evaluated from the in-situ XRD profiles.

In general, fully recrystallized metals and alloys are often suggested to have dislocation density 10^6 ~ 10^8 m^{-2}, whereas severe plastic deformed materials as ~ 10^{16} m^{-2}. In this sense, the dislocation density of 10^{17} m^{-2} in the fully recrystallized HfNbTaTiZr HEA is rather unusual and unrealistic. It is noteworthy that the dislocation density was evaluated from the XRD profiles by considering peak broadening (FWHM) as an important outcome. It has been suggested that HEAs are prone to severe lattice distortion effect due to the constituent elements having different atomic sizes and modulus mismatch. Song et al. [9] studied *ab initio* based theoretical calculations predicted the lattice distortion in BCC-HEAs is significantly high compared to FCC-HEAs. This could be understood by the fact that every lattice site in FCC has 12 nearest neighbors, whereas BCC has 8 nearest neighbors. FCC- HEAs have high chances of forming like-pair atomic bonds in the nearest neighbors and thus have smaller lattice distortion compared to BCC-HEAs. **Table 5.2** shows the physical properties of the constituent elements in the HfNbTaTiZr alloy.

Table 5.2 Physical properties of the constituent refractory elements in the present HfNbTaTiZr HEA [8].

Element	Hf	Nb	Ta	Ti	Zr
Atomic radius, r (Å)	1.541	1.429	1.430	1.418	1.551
Shear modulus, μ (GPa)	30	38	69	44	33

In the present alloy, the maximum atomic size difference was observed between Ti and Zr as 9.37%. This intrinsic lattice distortion might have increased the peak width of the XRD profiles which might affect the evaluated dislocation density. As a result, the peak broadening due to severe lattice distortion might be one of the reasons for the estimated substantial dislocation density.

It should be noted, however, dislocation density increased by two orders of magnitude but remained mostly constant after yielding. As is well known, flow stress is proportional to dislocation density, thus the constant dislocation density reflected in the lack of strain-hardening. Therefore, it can be concluded that the lack of strain-hardening and low strain-hardening exponent (n ~0.02) of the HfNbTaTiZr HEA could be due to constant dislocation density during deformation.

5.4.2. Hall-Petch Relationship, Friction Stress

The result from Hall-Petch relationship of the HfNbTaTiZr HEA showed large friction stress, σ_0 ~998 MPa. As was shown in **Table 5.1**, Young modulus of the present alloy and pure Nb are very similar, so the normalized friction stress by the Young modulus is shown between them as friction stress in HfNbTaTiZr (σ_0/E ~10487×10^{-6}) is almost one order of magnitude higher than the pure Nb (σ_0/E ~1142×10^{-6}). As was discussed in the former section 5.4.1, HEAs are prone to severe lattice distortion. As a result, atomic

positions of individual elements in any given unit cell of HEAs are displaced from the average lattice constant. **Figure 5.11** shows a schematic illustration of the possibility of lattice distortion in BCC-HEA. The dislocation core of HEAs might experience fluctuation of the Peierls-Nabarro energy barrier, so does the Peierls-Nabarro stress barrier (equivalent to friction stress) due to the variation of the local chemical environment [5]. **Figure 5.12** shows a schematic illustration showing the fluctuation of Peierls-Nabarro energy (Peierls potential energy). The increased fluctuations due to the lattice distortion might increase the friction stress in HEAs. Zhao and Nieh [18] has systematically studied the correlation between lattice distortion and friction stress in Ni-based equiatomic alloys. They found that the friction stress was linearly proportional to the lattice distortion. Further, Yoshida et al. [2] have reported high friction stress, σ_0 ~218 MPa in the CoCrNi an FCC medium entropy alloy compared to pure metals and conventional alloys.

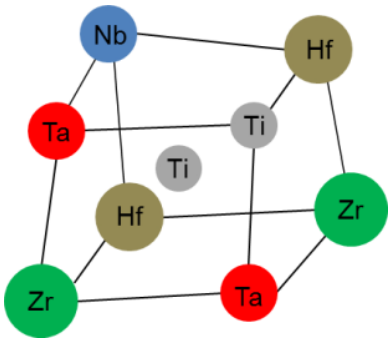

Figure 5.11 Schematic illustration showing the possibility of lattice distortion in HEAs due to atomic size mismatch.

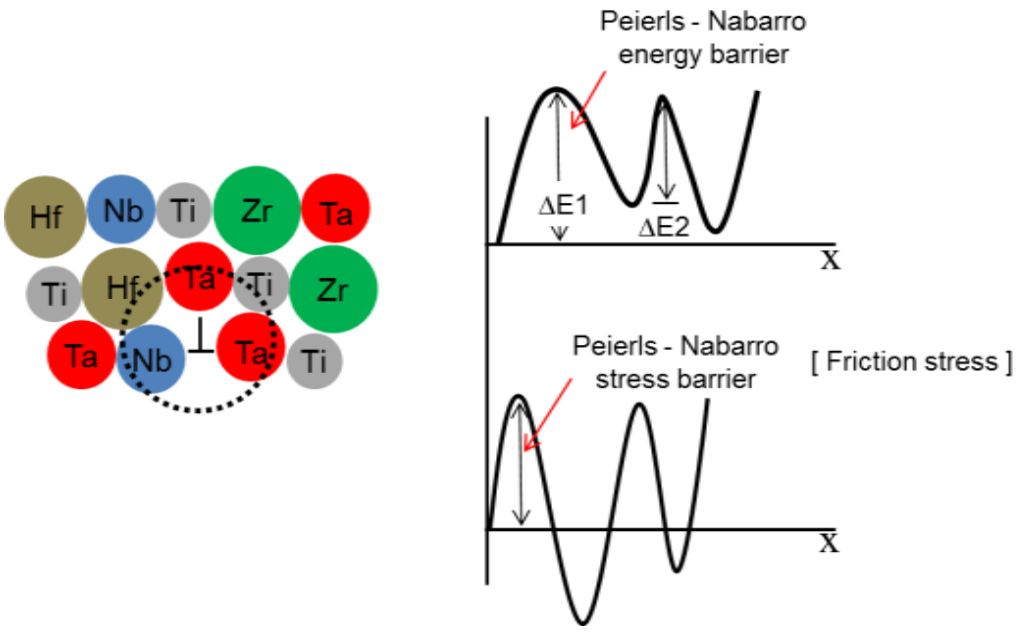

Figure 5.12 Schematic illustrations showing distorted lattice of HEA with dislocation, and the fluctuated Peierls potential energy resulted due to local lattice distortion. Black dot circle represents dislocation core.

Song et al. [9] conducted *ab initio* theoretical studies to determine the effect of atomic size mismatch on the local lattice distortion. Their study revealed that the BCC-HEAs particularly refractory HEAs showed local lattice distortion several times higher than the FCC-HEAs. Therefore, the friction stress deriving from the local lattice distortions could be very high in the BCC-HEAs. It should be noted furthermore, BCC metals and alloys naturally exhibit high friction stress compared to FCC metals and alloys, because screw dislocations in BCC crystals are suggested as non-planar. Therefore, considering the non-planar nature of screw dislocations combined with the unusual dislocation core structure and the fluctuated Peierls potential in BCC-HEAs might result exceptional friction stress as was experimentally observed. Based on this evidence it could be concluded that friction stress might be the characteristic property of HEAs.

5.4.3. Lack of Grain Boundary Strengthening Mechanism

The lack of increased yield strength with grain refinement showed the ineffectiveness of grain boundary strengthening mechanism in the present HfNbTaTiZr HEA (**Figure 5.3**). Generally speaking, such behavior is considered to be caused by the presence of grain boundary related mechanisms. A well-known example of the lack of grain boundary strengthening is the tensile behavior of pure-Mg [20]. The lack of grain boundary strengthening of Mg has been attributed to grain boundary sliding (GBS) mechanism.

For checking the possibility, tensile test was carried out on the pre-polished tensile specimen having an average grain size of ~6 µm. Marker grids having dimentions 100 µm (length) × 100 µm (height) × 0.3 µm (depth) were inscribed on the gauge part of the specimen by using focused ion beam (FIB) (Model: FEI Quanta 3D 200i). Further, digital image correlation (DIC) technique was used on the other side of the tensile specimen to measure the accurate deformation strain. The tensile test was carried out at ambient temperature for the strain-rate 8.3×10^{-4} s^{-1} deformed until, e ~10.4%. **Figure 5.13 a-b** shows the SEM-BSE images of microstructures with the grid patterns before and after deformation respectively. The high-magnification SEM-BSE images of the deformed specimen from different locations are shown in **Figure 5.14**. Microstructural observation showed shear offsets at the marker line and grain boundary intersections. These observations demonstrated direct evidence for the occurrence of GBS. It is, therefore to be noted that the lack of grain boundary strengthening mechanism in the HfNbTaTiZr HEA could be correlated to the occurrence of GBS mechanism. However, it should be noted that true stress-strain curves shown in **Figure 5.3 b** did not show flow softening but indicated a flat or steady-state flow behavior which means GBS might not be the dominant deformation mechanism at ambient temperature.

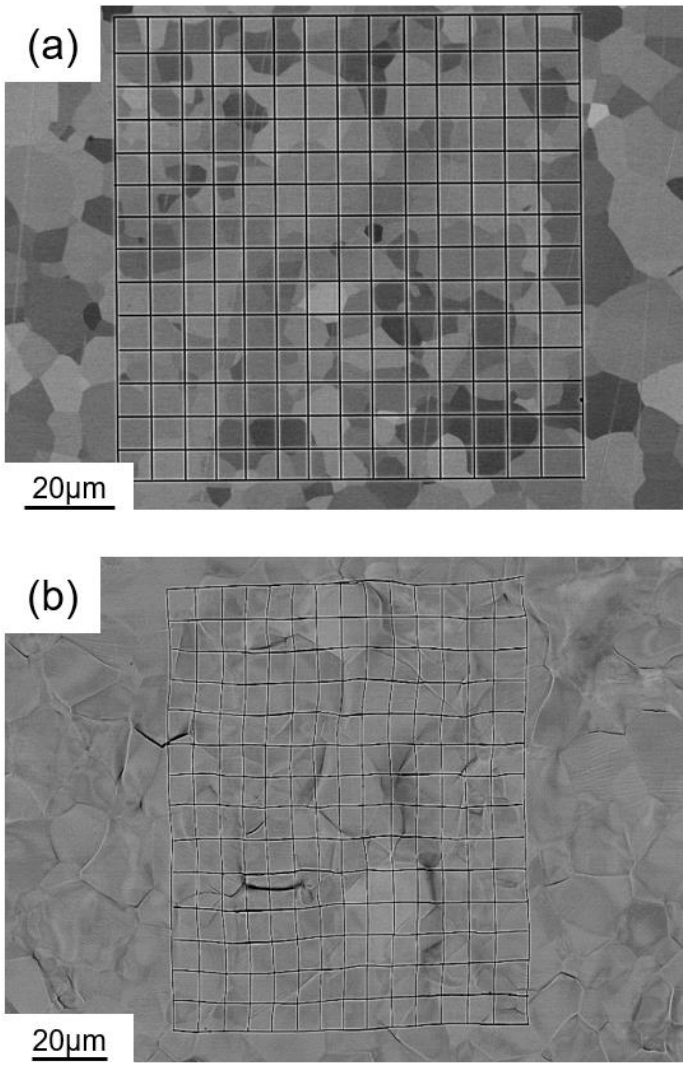

Figure 5.13 SEM-BSE images showing the microstructures on the tensile gauge part with the inscribed FIB marker grid. (a) The FIB marker grid before deformation, e = 0%, (b) FIB marker grid after tensile strain, e ~10.4%. The tensile axis is parallel to the vertical axis of microstructures.

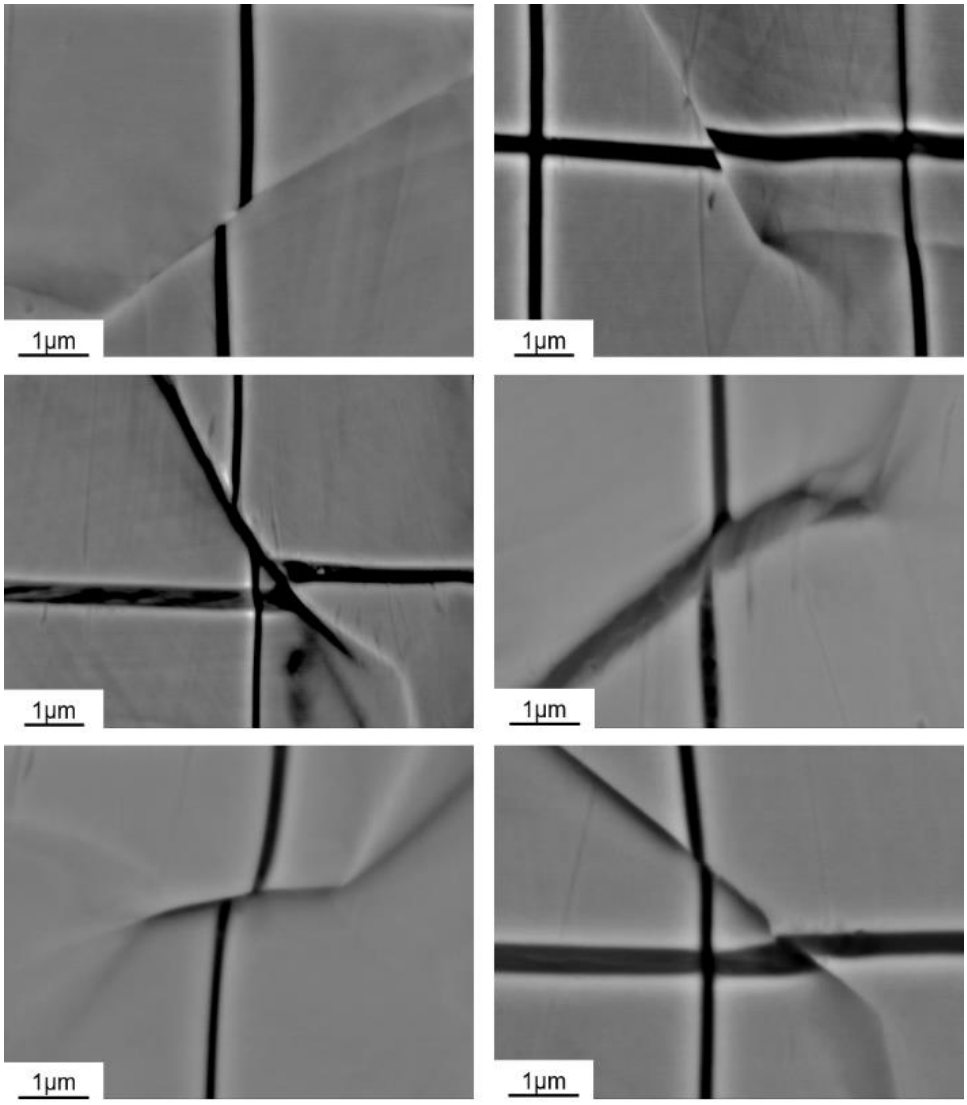

Figure 5.14 High-magnification SEM-BSE images of the deformed specimen (*e* ~10.4%) showing shear offsets at the marker line and grain boundary intersection. The observed shear offsets demonstrated direct evidence for the occurrence of grain boundary sliding (GBS) mechanism. The tensile axis is parallel to the vertical axis of microstructures.

5.4.4. Strain-rate Sensitivity and Activation Volume

Metallic materials that are susceptible to GBS mechanism exhibit high strain-rate sensitivity (*m*) of flow stress. The strain-rate jump test was used to evaluate the strain-rate sensitivity of HfNbTaTiZr alloy. Strain-rate jump test was carried out at three different strain-rates each with an order of magnitude difference such as 8.3×10^{-3} s^{-1}, 8.3×10^{-4} s^{-1}, and 8.3×10^{-5} s^{-1}. The tensile test was carried out on 6 μm grain size specimen. **Figure 5.16** shows the stress-strain curve of HfNbTaTiZr alloy showing rate dependent plastic flow behavior during strain-rate jump test. It was apparent that the change of flow stress was proportional to the change of strain-rate (i.e., the flow stress increased with the increased strain-rate, and vice versa). The dependence of change of flow stress concerning the change of strain-rate is expressed as,

$$m = \frac{\log(\sigma_2 / \sigma_1)}{\log(\dot{\varepsilon}_2 / \dot{\varepsilon}_1)} \tag{5.5}$$

where, *m* is strain-rate sensitivity, σ is flow stress (MPa), $\dot{\varepsilon}$ is strain-rate (s^{-1}). The estimated *m* value for the HfNbTaTiZr alloy at an ambient temperature ranged 0.017 ~ 0.019. As was reported, nanocrystalline (*d* ~100 nm) Cu also showed similar *m* value, *m* ~0.02 [21]. As was shown in **Chapters 2 and 3**, having proved the possibility of GBS in the HfNbTaTiZr alloy, the high-temperature *m* value was, *m* ~0.35. The *m* value at ambient temperature is obviously at least an order of magnitude lower compared to the *m* value at high-temperature, and yet, the experimental results showed the possibility of GBS at ambient temperature.

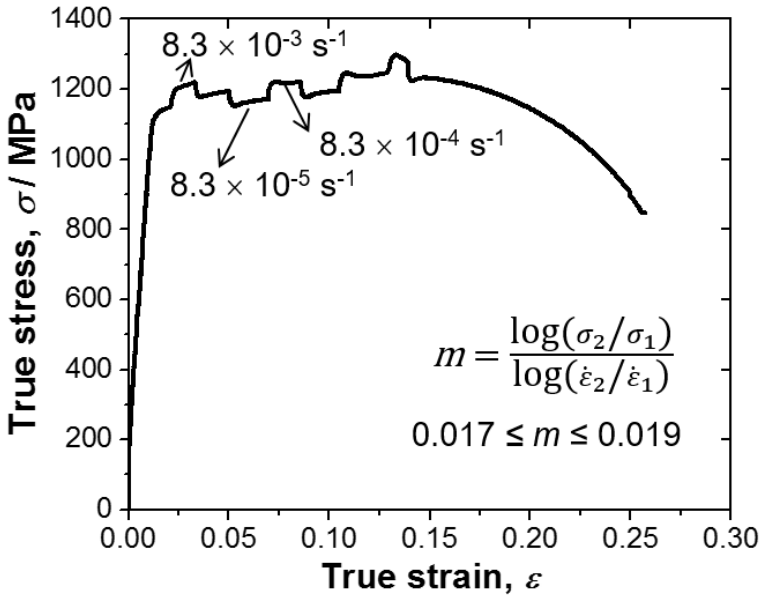

Figure 5.16 Stress-strain curve of HfNbTaTiZr HEA showing rate dependent plastic flow behavior during strain-rate jump test.

It should be pointed out that it is quite important to establish a correlation between surface measurements and processes occurring in the material volume. For instance, activation volume (V^*) can be estimated from the strain-rate dependence of the flow stress. Activation volume represents a proportional relationship for the area swept by the mobile dislocations. Metals and alloys that exhibit dislocation dominant intragranular slip tend to show high activation volume. This could provide fundamental aspects of plastic deformation like the thermally activated rate-controlling mechanism [22]. V^* is calculated by using the following equation,

$$V^* = \sqrt{3} k_B T \frac{\ln(\dot{\varepsilon}_2 / \dot{\varepsilon}_1)}{\Delta\sigma} \tag{5.6}$$

where, k_B is Boltzmann's constant, T is Temperature (K), $\dot{\varepsilon}$ is strain rate (s^{-1}), and σ is flow stress (MPa). **Figure 5.17** shows the normalized activation volume (V^*/b^3) for the HfNbTaTiZr HEA was ~6 b^3. It should be noted, furthermore, the evaluated V^* was mostly constant during the progress of plastic deformation.

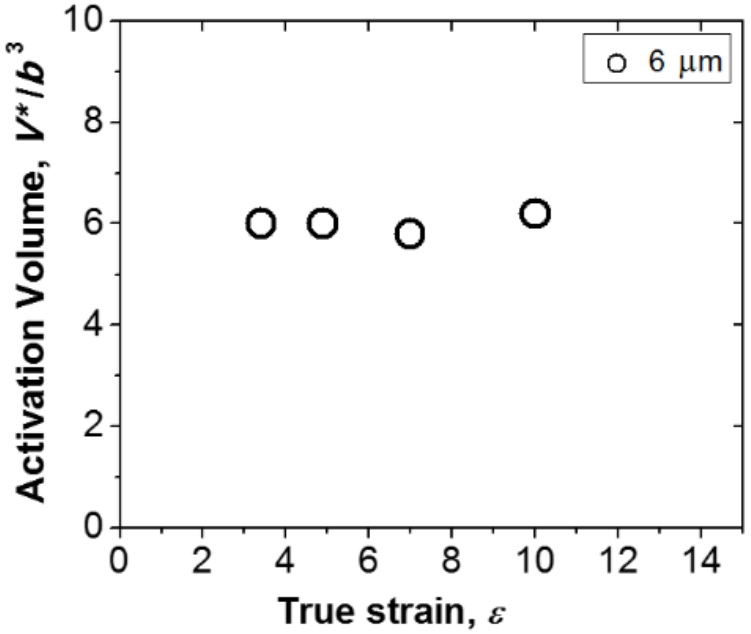

Figure 5.17 The evaluated apparent activation volume (V^*) as a function of deformation strain from the strain-rate jump test. V^* is normalized by the Burgers vector, b.

Wu et al. [7] showed a systematic study of CoCrFeMnNi and its derived FCC high entropy and medium entropy alloys and calculated the V^*. The calculated V^* of CoCrFeMnNi FCC-HEA having ~100 µm grain size ranged > 50 b^3 at 293 K. On the other hand, Couzinie et al. [17] calculated the V^* of the HfNbTaTiZr BCC-HEA having ~80 µm grain size. The calculated V^* ranged between 33 and 48 b^3. As is well-known, the V^* > 10

b^3 indicate thermally activated dislocation glide as the rate-controlling mechanism [22]. It has been suggested that the dislocation line in HEAs are locally bowed due to atomic size and modulus mismatch between unlike atomic pairs. This situation of dislocations in the HEA is considered similar to the interaction of forest of solute atoms and the gliding dislocation. According to the classic Labusch model, the pinning effect of concentrated solute alloys on the gliding dislocations is rather weak, and the same has been considered to apply for the concentrated alloys like HEAs. As a result of this, activation of dislocation glide indeed leads to high V^* [7]. Both the existing standard examples of HEAs, i.e., CoCrFeMnNi FCC-HEA and HfNbTaTiZr BCC-HEA, have shown thermally activated dislocation glide as the primary deformation mechanism.

It is noteworthy, however, the present observations on fine-grained HfNbTaTiZr alloy indicated low $V^* \sim 6\ b^3$. The activation volume as low as $\sim 5\ b^3$ was reported in ultrafine-grained Mg [20] and $\sim 8\ b^3$ in nanocrystalline Cu [21]. The low V^* in those pure metals was accounted for the occurrrence of grain boundary mediated deformation mechanism. The typical V^* values and the corresponding rate-controlling mechanisms are shown in the following **Table 5.3**. The evaluated V^* in the present study indicated dislocation-mediated grain boundary sliding/shearing might be the rate-controlling mechanism.

Table 5.3 Rate-controlling mechanisms and the corresponding typical activation volumes observed in metals and alloys [23].

Rate-controlling Mechanism	**Typical V^*/b^3**
Dislocation mediated grain boundary sliding/shearing	$1 – 10\ b^3$
Overcoming the Peierls-Nabarro stress	$10 – 10^2\ b^3$
Cutting through forest dislocations	$10^2 – 10^4\ b^3$

Conrad [23] proposed a model for Cu having ultra-fine grained microstructures. In the model, Conrad assumed the possibility of grain boundary sliding could be realized due to the shear of dislocations situated at the head of dislocation pile-up. It was suggested that the stress concentration at the head of dislocation pile-up could be sufficiently high to promote shear at the grain boundary. The transition of the dislocation situated at the head of the dislocation pile-up controls the rate of deformation. Thus, dislocation-mediated grain boundary sliding accounts as the rate-controlling mechanism.

One of the possible ways of realizing Conrad's approach in the HfNbTaTiZr BCC-HEA is to confirm dislocation pile-up. It is noteworthy however, BCC metals and alloys undergo plastic deformation by extensive cross-slip such that dislocation pile-up is least observed. In the present study, interrupted tensile tests were performed to verify the possibility of dislocation pile-up in the BCC-HEA. The interrupted tensile test was carried out on the ~6 μm grain size specimen deformed until, e ~2.2% and immediately unloaded. **Figure 5.18** shows the TEM image of the HfNbTaTiZr HEA deformed until, e ~2.2%. TEM image confirmed dislocation pile-up at the grain boundary. The observed dislocations satisfied the invisibility criteria $g.b = 0$ for the diffraction vector, $g = 110$. Based on this analysis, observation indicated the typical <111> slip direction, suggesting {110}<111> or {112}<111> as potentially active slip systems during the initial stages of plastic deformation. Moreover, dislocation pile-up confirmed dislocations were localized in narrow bands. Similar observations were extensively reported in low stacking fault energy (low-SFE) FCC metals and alloys that primarily deform by planar slip. Unlike low-SFE FCC metals and alloys, BCC metals and alloys undergo plastic deformation by extensive cross-slip such that dislocation pile-up is least observed [24]. Although the origin of planar slip in the HfNbTaTiZr is not yet understood, the observation confirmed the possibility of dislocation pile-up at the grain boundary.

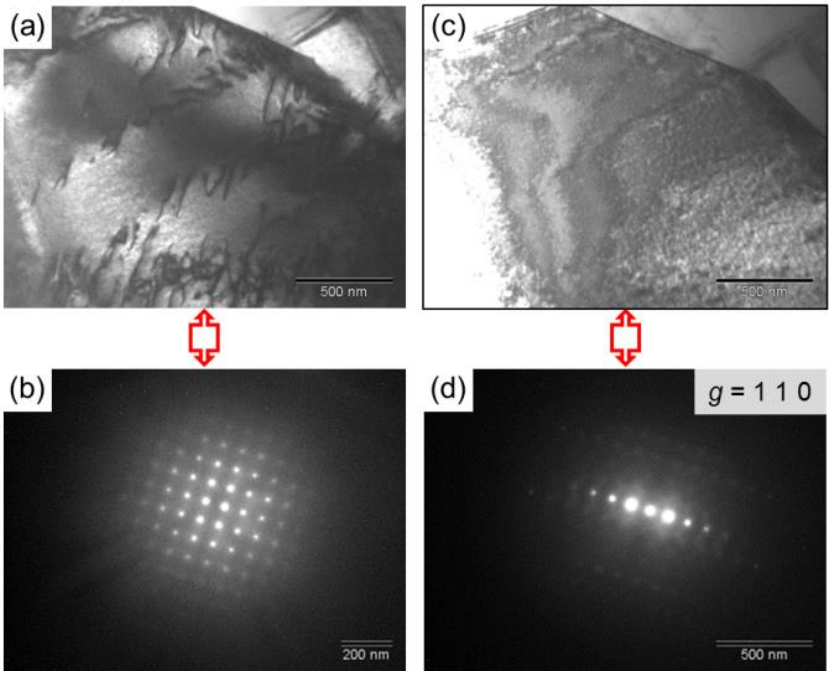

Figure 5.18 TEM images and the corresponding diffraction patterns of the HfNbTaTiZr HEA deformed until, e ~ 2.2%. (a) TEM image showing clear dislocation pile-up at the grain boundary, (b) Transmitted diffraction pattern corresponding to the TEM image shown in (a), (c) TEM image showing all dislocations satisfied invisibility criteria $g.b = 0$ for the diffraction vector g = 110 shown in (d).

The present experimental results appear to coincide with Conrad model, which represents the plastic deformation of HfNbTaTiZr HEA is controlled by the dislocation-mediated grain boundary sliding. However, this correlation does not have to be readily considered since Conrad model does not take grain boundary structure into account. As is well known, the onset of GBS in metallic materials can also result due to the special nature of grain boundaries. With that consideration, the present alloy which is primarily composed of refractory elements requires further systematic and rigorous experimental studies that

can show the nature of grain boundaries present in the equiatomic HfNbTaTiZr refractory high entropy alloy.

5.5. Conclusions

In the present chapter, the effect of grain refinement on mechanical properties of the HfNbTaTiZr BCC-HEA was systematically investigated. Based on tensile stress-strain behaviors and microstructural observations, the following conclusions were drawn:

1. Microstructures of HfNbTaTiZr HEA composed of equiaxed grains having grain sizes ~6 μm to 50 μm were successfully fabricated using conventional cold rolling and annealing.

2. Stress-strain curves for all grain sizes showed a lack of significant strain-hardening. It should be noted; furthermore, stress-strain curves showed a lack of significant increase in yield strength with the grain refinement. This observation suggested the HfNbTaTiZr HEA was ineffective to the grain boundary strengthening mechanism.

3. The Hall-Petch relationship of HfNbTaTiZr HEA revealed high friction stress (σ_0) ~998 MPa and low grain boundary strengthening coefficient (k_{HP}) ~322 MPa.$\mu m^{0.5}$.

4. High friction stress was attributed to the fluctuation of Peierls potential energy for the dislocation motion due to local lattice distortion at the atomic level in HEAs.

5. Tensile test using in-situ XRD analysis suggested dislocation density increased immediately after yielding but remained mostly unchanged during the progress of plastic deformation. Considering the proportionality between flow stress and dislocation density, lack of increment in dislocation density was attributed as one of the reasons for the lack of strain-hardening of HfNbTaTiZr.

6. A systematic tensile deformation on the fine-grained (~6 μm) pre-polished specimen having inscribed marker lines showed shear offsets at the marker line and

the grain boundary intersections. Based on this experimental observation, it was confirmed that the HfNbTaTiZr HEA could deform by grain boundary sliding (GBS) mechanism at ambient temperature. Consequently, the occurrence of GBS was attributed to the lack of grain boundary strengthening mechanism.

7. Strain rate jump tests suggested relatively high strain rate sensitivity, m ~0.019 of flow stress of the HfNbTaTiZr HEA. The estimated activation volume (V^*) from the strain rate jump tests indicated V^* ~6 b^3. Low V^* (< 10 b^3) suggested dislocation-mediated grain boundary sliding (GBS) might be the rate-controlling mechanism during the plastic deformation of HfNbTaTiZr HEA. The low V^* value coincided with the possibility of GBS mechanism as was experimentally observed.

References

[1] N. Tsuji, Y. Ito, Y. Saito, Y. Minamino, Strength and ductility of ultrafine grained aluminum and iron produced by ARB and annealing, Scr. Mater. 47 (2002) 893–899. doi:https://doi.org/10.1016/S1359-6462(02)00282-8.

[2] G.E. Dieter, Mechanical Metallurgy, third ed., Mc-Graw Hill, London, 1988.

[3] F. Otto, A. Dlouhý, C. Somsen, H. Bei, G. Eggeler, E.P. George, The influences of temperature and microstructure on the tensile properties of a CoCrFeMnNi high-entropy alloy, Acta Mater. 61 (2013) 5743–5755. doi:https://doi.org/10.1016/j.actamat.2013.06.018.

[4] S.S. Sohn, A. Kwiatkowski da Silva, Y. Ikeda, F. Körmann, W. Lu, W.S. Choi, B. Gault, D. Ponge, J. Neugebauer, D. Raabe, Ultrastrong Medium-Entropy Single-Phase Alloys Designed via Severe Lattice Distortion, Adv. Mater. 0 (2018) 1807142. doi:10.1002/adma.201807142.

[5] R.S. Mishra, N. Kumar, M. Komarasamy, Lattice strain framework for plastic deformation in complex concentrated alloys including high entropy alloys, Mater. Sci. Technol. 31 (2015) 1259–1263. doi:10.1179/1743284715Y.0000000050.

[6] S. Yoshida, T. Bhattacharjee, Y. Bai, N. Tsuji, Friction stress and Hall-Petch relationship in CoCrNi equi-atomic medium entropy alloy processed by severe plastic deformation and subsequent annealing, Scr. Mater. 134 (2017) 33–36. doi:https://doi.org/10.1016/j.scriptamat.2017.02.042.

[7] Z. Wu, Y. Gao, H. Bei, Thermal activation mechanisms and Labusch-type strengthening analysis for a family of high-entropy and equiatomic solid-solution alloys, Acta Mater. 120 (2016) 108–119. doi:https://doi.org/10.1016/j.actamat.2016.08.047.

[8] Z. Wang, Q. Fang, J. Li, B. Liu, Y. Liu, Effect of lattice distortion on solid solution strengthening of BCC high-entropy alloys, J. Mater. Sci. Technol. 34 (2018) 349–

354. doi:https://doi.org/10.1016/j.jmst.2017.07.013.

[9] H. Song, F. Tian, Q.-M. Hu, L. Vitos, Y. Wang, J. Shen, N. Chen, Local lattice distortion in high-entropy alloys, Phys. Rev. Mater. 1 (2017) 23404. doi:10.1103/PhysRevMaterials.1.023404.

[10] C.-C. Juan, M.-H. Tsai, C.-W. Tsai, W.-L. Hsu, C.-M. Lin, S.-K. Chen, S.-J. Lin, J.-W. Yeh, Simultaneously increasing the strength and ductility of a refractory high-entropy alloy via grain refining, Mater. Lett. 184 (2016) 200–203. doi:https://doi.org/10.1016/j.matlet.2016.08.060.

[11] B. Kang, J. Lee, H.J. Ryu, S.H. Hong, Ultra-high strength WNbMoTaV high-entropy alloys with fine grain structure fabricated by powder metallurgical process, Mater. Sci. Eng. A. 712 (2018) 616–624. doi:https://doi.org/10.1016/j.msea.2017.12.021.

[12] B. Kang, J. Lee, H.J. Ryu, S.H. Hong, Microstructure, mechanical property and Hall-Petch relationship of a light-weight refractory Al0.1CrNbVMo high entropy alloy fabricated by powder metallurgical process, J. Alloys Compd. 767 (2018) 1012–1021. doi:https://doi.org/10.1016/j.jallcom.2018.07.145.

[13] D. Wu, J. Zhang, J.C. Huang, H. Bei, T.G. Nieh, Grain-boundary strengthening in nanocrystalline chromium and the Hall–Petch coefficient of body-centered cubic metals, Scr. Mater. 68 (2013) 118–121. doi:https://doi.org/10.1016/j.scriptamat.2012.09.025.

[14] Z.C. Cordero, B.E. Knight, C.A. Schuh, Six decades of the Hall–Petch effect – a survey of grain-size strengthening studies on pure metals, Int. Mater. Rev. 61 (2016) 495–512. doi:10.1080/09506608.2016.1191808.

[15] G.K. Williamson, W.H. Hall, X-ray line broadening from filed aluminium and wolfram, Acta Metall. 1 (1953) 22–31. doi:https://doi.org/10.1016/0001-6160(53)90006-6.

[16] G.K. Williamson, R.E. Smallman, III. Dislocation densities in some annealed and

cold-worked metals from measurements on the X-ray debye-scherrer spectrum, Philos. Mag. A J. Theor. Exp. Appl. Phys. 1 (1956) 34–46. doi:10.1080/14786435608238074.

[17] J.-P. Couzinié, L. Lilensten, Y. Champion, G. Dirras, L. Perrière, I. Guillot, On the room temperature deformation mechanisms of a TiZrHfNbTa refractory high-entropy alloy, Mater. Sci. Eng. A. 645 (2015) 255–263. doi:https://doi.org/10.1016/j.msea.2015.08.024.

[18] Y.Y. Zhao, T.G. Nieh, Correlation between lattice distortion and friction stress in Ni-based equiatomic alloys, Intermetallics. 86 (2017) 45–50. doi:https://doi.org/10.1016/j.intermet.2017.03.011.

[19] Z. Wu, H. Bei, F. Otto, G.M. Pharr, E.P. George, Recovery, recrystallization, grain growth and phase stability of a family of FCC-structured multi-component equiatomic solid solution alloys, Intermetallics. 46 (2014) 131–140. doi:https://doi.org/10.1016/j.intermet.2013.10.024.

[20] H. Somekawa, T. Mukai, Hall–Petch Breakdown in Fine-Grained Pure Magnesium at Low Strain Rates, Metall. Mater. Trans. A. 46 (2015) 894–902. doi:10.1007/s11661-014-2641-2.

[21] J. Chen, L. Lu, K. Lu, Hardness and strain rate sensitivity of nanocrystalline Cu, Scr. Mater. 54 (2006) 1913–1918. doi:https://doi.org/10.1016/j.scriptamat.2006.02.022.

[22] D. Caillard, J.L. Martin, Thermally activated mechanisms in crystal plasticity, first ed., Pergamon, 2003.

[23] H. Conrad, Grain size dependence of the plastic deformation kinetics in Cu, Mater. Sci. Eng. A. 341 (2003) 216–228. doi:https://doi.org/10.1016/S0921-5093(02)00238-1.

[24] D. Hull, D.J. Bacon, Introduction to Dislocations, fifth ed., Butterworth-Heinemann, 2011.

Chapter 6

Summary and Conclusions

In the present thesis, "*Deformation Mechanisms and Microstructure Evolution in HfNbTaTiZr High Entropy Alloy during Thermo-mechanical Processing at Elevated Temperatures*" were studied. The present study revealed several important and unique behaviors of the HfNbTaTiZr during thermo-mechanical processing (TMP) at high temperatures and tensile behavior at ambient temperature. Each of the behavior was systematically analyzed and experimentally verified. The main results obtained from every chapter are briefly summarized and concluded below:

In **Chapter 1**, this thesis has reported the relevant introduction and background to high entropy alloys, thermo-mechanical processing and objective of the present study.

In **Chapter 2**, this thesis has reported deformation behavior and microstructure evolution in high temperature processing of HfNbTaTiZr refractory high entropy alloy. Hot-deformation by uniaxial compression was carried out at different temperatures (1000°C, 1100°C, and 1200°C) for various strain rates (10^{-4} s^{-1}, 10^{-3} s^{-1}, and 10^{-2} s^{-1}) until 50% of initial height reduction (equivalent strain, $\varepsilon = 0.69$). The deformed specimens were quenched by water immediately after the compression to freeze microstructures and provided for microstructural observations.

Stress-strain curves for most of the hot-compressed conditions showed sharp drop of the flow stress around yielding followed by continuous flow softening. When the compression at 1000°C was stopped just after the sharp stress-drop and immediately

restarted, the stress-drop disappeared. On the other hand, when the specimens were held at 1000°C for 120 s ~ 600 s after quitting the hot-compression, the sharp stress-drop occurred in subsequent re-loading and the degree of the stress drop increased with increasing the holding time. Based on these results, the sharp drop of the flow stress in HfNbTaTiZr was attributed to dislocation unlocking from any substitutional solute atom(s). In correlation to the continuous flow softening observed after the sharp stress-drop, characteristic necklace microstructures composed of coarse unrecrystallized grains surrounded by fine dynamically recrystallized grains were observed. The occurrence of dynamic recrystallization (DRX) was considered as one of the reasons for the flow softening.

Apparent activation energy (Q) for high-temperature deformation of HfNbTaTiZr was evaluated as 124 ~ 113 $kJmol^{-1}$ from the stress-strain data obtained from the hot-compression. The evaluated Q was lower than the activation energies for self-diffusion of the pure elements included in the alloy, but somehow close to the activation energies for self-diffusion in high-temperature β phase (BCC) of Ti and Zr.

Depending on the deformation conditions, DRX grain sizes ranged from 0.7 μm to 34 μm. The fine DRX grain sizes suggested a possibility of sluggish diffusion in the HfNbTaTiZr HEA. The DRX fraction and DRX grain size were well organized as a function of the flow stress rather than Z (calculated by the use of the activation energy of 113 $kJmol^{-1}$. The DRX fraction and the DRX grain size increased with decreasing the flow stress. In the necklace DRX microstructures, coarse unrecrystallized grains had <001> and <111> fiber textures parallel to the compression axis, which suggested plastic deformation by dislocation slip similar to conventional BCC metals and alloys. On the other hand, the DRX grains did not have texture but rather randomly oriented.

The flow stress analysis indicated high strain-rate sensitivity (m) of 0.35 in the hot-compression, which suggested a possibility of grain boundary sliding (GBS) even in the heterogeneous necklace microstructures composed of coarse unrecrystallized regions and fine DRX grains. The fine DRX grains were considered preferable for the occurrence of GBS, and the nearly random texture observed for the DRX grains coincided with GBS.

In **Chapter 3**, this thesis has reported dynamic recrystallization and related deformation mechanisms in equiatomic HfNbTaTiZr refractory high entropy alloy. The microstructural evolution was studied by deforming the specimens at 1000°C for the strain rate 10^{-3} s^{-1} until different strain intervals (ε = 0.06 ~ 0.69). The deformed specimens were quenched by water immediately after the compression to freeze microstructures and provided for microstructural observations.

The stress-strain curve of HfNbTaTiZr HEA hot-deformed at 1000°C for the strain rate 10^{-3} s^{-1} showed a sharp drop followed by continuous flow-softening.

The microstructural observations confirmed evolution of the characteristic DRX necklace structure preceded by significant grain boundary bulging of the initial grain boundaries. A careful microstructural evaluation showed DRX grains having near ultra-fine grain size, d ~ 1.5 μm. DRX grains having grain size ~1.5 μm showed inhibited grain growth at high temperature. DRX was strictly confined to grain boundary regions, thus resulted microstructures had coarse unrecrystallized grain and surrounding DRX necklace structure. Moreover, the first formed DRX grains had orientation similar to the parent grain. The progress of deformation increased DRX fraction but randomized the DRX grains orientations.

Considering the high strain rate sensitivity, m ~ 0.35, for the first time, the present study showed direct evidence for DRX grains deforming by grain boundary sliding (GBS) mechanism. The occurrence of GBS was attributed to the high temperature DRX grain size stability and the phenomenon of DRX grains texture randomization.

The progress of deformation during the occurrence of GBS has shown several interesting microstructural characteristics in the DRX necklace region. The deformation developed mesoscopic bands having ‘T’-type junctions along the DRX necklace structure which was most likely due to the GBS mechanism accommodated by triple junction migration. As the deformation strain increased until ε ~0.69, several interconnected bands

formed diamond-shaped grains having ‘X’-type junctions. Moreover, intense low angle grain boundaries were observed in the adjacent regions of DRX necklace structure.

Finally, the observed microstructural aspects like DRX and GBS were correlated to the continuous flow-softening observed in the stress-strain curve.

The present study is so far the first systematic study that has shown the direct evidence for DRX grains deform by GBS mechanism.

In **Chapter 4**, this thesis has reported recrystallization behavior of the hot-deformed HfNbTaTiZr refractory high entropy alloy. Initially, hot-deformation was carried out at 1000°C for the strain rate 10^{-3} s^{-1} until 50% of initial height reduction (equivalent strain, ε = 0.69). Followed by the deformation, the deformed specimens were subsequently annealed by holding at the deformation temperature (1000°C) for different time intervals (300 s ~ 3600 s). This study is analogous to the static recrystallization process. The deformed and annealed specimens were quenched by water immediately after the test to freeze microstructures and provided for microstructural observations.

Detailed analysis concerning the deformed microstructure and the GBS mechanism was discussed in chapter 3. Annealing the hot-deformed specimens showed high microstructural stability until 600 s. However, annealing above 900 s showed rapid grain growth of the pre-existing DRX grains. The recrystallized grain size continuously increased with the annealing time.

During the annealing process, the classical recrystallization mechanism, i.e., restoration of the deformed volume by the nucleation of new strain-free grains was least observed. Furthermore, the microstructural changes during annealing indicated least evidence for well-defined sub-grain structures in the deformed/unrecrystallized grains interiors. The lack of typical recrystallization characteristics during annealing was

considered due to the lack of necessary dislocation density in the hot-deformed grains, which was accounted for the occurrence of grain boundary sliding (GBS) mechanism along the DRX grains during hot-deformation.

Grain boundary migration by the growth of pre-existing DRX grains appeared to be the primary and probably the only effective means of recrystallization for the hot-deformed HfNbTaTiZr alloy during annealing process. Accordingly, the prevailed random DRX grains texture during recrystallization supported the experimental observations.

In **Chapter 5**, this thesis has reported the lack of normal hardening in HfNbTaTiZr body-centered cubic high entropy alloy. Here, the effect of grain size on the mechanical properties of HfNbTaTiZr HEA was studied with particular emphasis given to the deformation mechanisms. Homogeneous microstructures having different grain sizes ranging from ~6 μm to ~50 μm were successfully fabricated using conventional cold rolling and annealing treatment. Mechanical properties of the obtained microstructures were investigated using tensile deformation at ambient temperature.

Stress-strain curves of tensile deformed HfNbTaTiZr HEA showed lack of strain-hardening. On the other hand, grain refinement showed no significant increment of yield strength that implied; the HfNbTaTiZr HEA showed lack of grain boundary strengthening mechanism. The Hall-Petch relationship indicated high friction stress, σ_0 ~998 MPa. High friction stress was attributed to the fluctuation of Peierls potential energy for the dislocation motion due to local lattice distortion at the atomic level in HEAs.

Tensile test using in-situ XRD analysis suggested dislocation density increased immediately after yielding but remained mostly constant during the progress of plastic deformation. Considering the proportionality between flow stress and dislocation density, lack of increment in dislocation density was attributed as one of the reasons for the lack of strain-hardening of HfNbTaTiZr.

The lack of grain boundary strengthening mechanism was carefully investigated by inscribing marker lines on the pre-polished tensile specimen having ~6 μm grain size. Microstructural observations of the same specimen after tensile deformation (e ~10.4%) indicated shear offsets at the marker line and grain boundary intersections. Based on this experimental observation, it was confirmed that the HfNbTaTiZr HEA could deform by grain boundary sliding (GBS) mechanism at ambient temperature. Consequently, the occurrence of GBS was attributed to the lack of grain boundary strengthening mechanism.

Strain rate jump tests suggested relatively high strain rate sensitivity, m ~0.019 of flow stress of HfNbTaTiZr HEA. Adding to that, the activation volume (V^*) estimated from the strain-rate jump test revealed, V^* ~6 b^3. Low V^* ($V^* < 10\ b^3$) suggested dislocation-mediated grain boundary sliding might be the rate-controlling mechanism during plastic deformation of the HfNbTaTiZr HEA. The low V^* value coincided with the possibility of GBS mechanism as was experimentally observed.

The present study is so far the first systematic study that has shown correlation between the lack of strain-hardening and grain boundary strengthening, and the operative deformation mechanisms of the HfNbTaTiZr HEA during tensile deformation at ambient temperature.

In **Chapter 6**, this thesis has reported experimental findings from every chapter were briefly summarized and concluded.

Acknowledgments

I would like to express my sincere gratitude to my thesis advisor Prof. Nobuhiro Tsuji, for giving an opportunity to pursue my higher studies with him. I sincerely acknowledge his invaluable suggestions and productive discussions during the course of my study. I also acknowledge his patience in proofreading my thesis and manuscripts. It would not be exaggerated that this thesis could not have finished in the given time without his continuous support and encouragement.

I would like to extend my sincere gratitude to Prof. Atul H. Chokshi, Indian Institute of Science, India, for his invaluable suggestions and most effective discussions during his stay at Kyoto University.

I would like to thank my seniors Tilak Bhattacharjee, Mohit Joshi and my friends Sushma Kumari, Prashant Goyal, and Gunjan Sapra for their unconditional help during my stay in Japan. I would also like to thank Asso. Prof. Akinobu Shibata and Assi. Prof. Yu Bai of Tsuji laboratory for their help. Thanks are due to all the lab members for creating a healthy research atmosphere. I would like to thank Ms. Akiko Koike, secretary of Tsuji lab for her continuous help during my day to day activities and for processing all the official documents regarding my Ph.D.

I would like to express my sincere appreciation to Prof. Haruyuki Inui and Prof. Hideyuki Yasuda of Kyoto University for their acceptance to evaluate my thesis.

Most importantly, acknowledgments are due to the Japan International Cooperation Agency (JICA) - FRIENDSHIP scholarship, for financial support during the course of my study at Kyoto University, Japan. I will always be owing gratitude to the JICA for invaluable support.